Interference Cancellation For Faster-Than-Nyquist Wireless Communications

by **Mingfei Tong**

Thesis submitted in fulfilment of the requirements for the degree of
Doctor of Philosophy
under the supervision of
Prof. Xiaojing Huang
and
Prof. Andrew Zhang

School of Electrical and Data Engineering
Faculty of Engineering and IT
University of Technology Sydney
July 15, 2025

Certificate of Original Authorship

I, Mingfei Tong, declare that this thesis is submitted in fulfilment of the requirements for the award of Doctor of Philosophy, in the School of Electrical and Data Engineering at the University of Technology Sydney.

This thesis is wholly my own work unless otherwise referenced or acknowledged. In addition, I certify that all information sources and literature used are indicated in the thesis.

This document has not been submitted for qualifications at any other academic institution.

This research is supported by the Australian Government Research Training Program.

Signature: Production Note:
Signature removed prior to publication.

Date: July 15, 2025

Abstract

The transition to sixth-generation (6G) networks promises transformative advancements in speed (up to 1 Tbps), spectral efficiency (over 100 bits/Hz), latency, and connectivity. Faster-than-Nyquist (FTN) signalling emerges as a key enabler, boosting spectral efficiency by intentionally violating the Nyquist criterion, albeit introducing inter-symbol interference (ISI). This thesis develops a low-complexity, high-performance FTN system with practical feasibility, addressing critical challenges in ISI cancellation, channel adaptability, and hardware impairments.

A novel frame-by-frame decision-directed successive interference cancellation (DDSIC) scheme is proposed, integrating frequency-domain minimum-mean-square-error (FD-MMSE) equalisation. Compared to existing methods, DDSIC achieves superior bit error rate (BER) performance with reduced computational complexity, particularly under high-order modulation.

To enhance real-world applicability, the system is tested under multipath fast-fading channels, where rapid channel state information (CSI) variations and Doppler shifts degrade performance. Traditional DDSIC, reliant on static CSI, is augmented with an adaptive transmission precoding (ATPC) method to counteract time-varying distortions. Simulations confirm ATPC's robustness in dynamic environments.

Beyond channel challenges, hardware imperfections like I/Q imbalance (IQI) in radio frequency (RF) front-ends are addressed. IQI causes image band interference, particularly in direct-conversion architectures. This work introduces an expanded signal model analyzing both primary and image band components, enabling joint suppression of IQI and ISI. The proposed DDSIC framework mitigates IQI to near-zero levels while maintaining high performance in multipath fading.

Overall, the core contributions of this thesis lie in three areas: (i) the development of a low-complexity DDSIC algorithm for effective ISI cancellation; (ii) the enhancement of system adaptability to fast-fading channels through ATPC; and (iii) the integration of IQI mitigation within the FTN framework. Extensive simulations validate the system's performance across diverse wireless environments, bridging the gap between theoretical FTN capacity gains and practical 6G deployment readiness.

Acknowledgements

First and foremost, my heartfelt appreciation goes to my supervisor, Prof. Xiaojing Huang. It is his careful, patient, warm and insightful guidance that enabled me to learn how to embark and how to make progress on the road of scientific research, and also inspired me to work hard in higher and deeper academic fields in the future. His encouragement during difficult times and his clear direction when I felt lost have been the most profound influences in my growth as a researcher. I am also deeply grateful to my co-supervisor, Prof. J. Andrew Zhang, whose guidance and dedication are indispensable in my progress. His contributions were not only valuable but truly vital in my accomplishments.

I would like to extend my sincere thanks to my friends and colleagues who stood by me during my doctoral studies: Dr. Hongyang Zhang, Junjie Huang, Shangyi Sun, Yongle Zhang, Feng Tao, Zhaoqi Cui, Keda Xu, Fanchao Zeng, Xingyu Cheng, Dr. Hao Zhang, and Dr. Anh Tuyen Le. Their companionship and support made this journey much richer and more colorful. The memories we have created together will forever be some of the most precious moments of my life.

I would also like to express my deepest gratitude to my parents. Your unconditional love and selfless support are the foundation of everything I have achieved. Without your sacrifices, encouragement, and belief in me, none of this would have been possible.

Finally, I want to say to myself – thank you for sailing through the sea of learning for the past twenty years, and for still holding on to your original dream. I hope that, in the future, the dust of challenges will not dim the brightness of your eyes at this moment. May you always remember to be grateful for life and for the chance to keep burning brightly.

Mingfei Tong

July 15, 2025

Sydney, Australia

Publications

Publications Related to This Thesis

Journal Papers

J-1. **M. Tong**, X. Huang and J. A. Zhang, "Faster-Than-Nyquist Transmission With Frame-by-Frame Decision-Directed Successive Interference Cancellation," *IEEE Transactions on Communications*, vol. 71, no. 8, pp. 4851-4861, Aug. 2023, doi: 10.1109/TCOMM.2023.3279404.

J-2. **M. Tong**, X. Huang, J. A. Zhang and L. Hanzo, "Adaptive FTN Signaling Over Rapidly-Fading Channels," to appear in *IEEE Transactions on Communications*, doi: 10.1109/TCOMM.2025.3545655.

J-3. **M. Tong**, X. Huang and J. A. Zhang, "Joint Interference Cancellation for FTN Systems with I/Q Imbalance," to appear in *IEEE Transactions on Wireless Communications*, doi: 10.1109/TWC.2024.3523493.

Conference Papers

C-1. **M. Tong**, X. Huang and J. A. Zhang, "Frame-based Decision Directed Successive Interference Cancellation for FTN Signaling," in Proceedings of *2022 IEEE Globecom Workshops (GC Wkshps)*, Rio de Janeiro, Brazil, 4-8 Dec. 2022, pp. 1670-1674, doi: 10.1109/GCWkshps56602.2022.10008577.

C-2. **M. Tong**, X. Huang, J. A. Zhang and Y. J. Guo, "Joint Interference Cancellation for FTN Signaling in I/Q Imbalanced Environment," in Proceedings of *2024 23rd Interna-*

tional Symposium on Communications and Information Technologies (ISCIT), Bangkok, Thailand, 23-25 Sept. 2024, pp. 223-228, doi: 10.1109/ISCIT63075.2024.10793684. (Received Best Paper Award.)

Contents

List of Figures

List of Tables

Abbreviations

3GPP - 3rd generation partnership project

5G - fifth generation

6G - sixth generation

ADC - analog-to-digital converter

AI - artificial intelleigence

AR - augmented realit

ATPC - adaptive transmission precoding

AWGN - additive white Gaussian noise

BCJR - Bahl-Cocke-Jelinek-Raviv

BER - bit error rate

BPSK - binary phase shift keying

CFO - carrier frequency offset

CIR - channel impulse response

CMOS - complementary metal-oxide semiconductor

CoMP - coordinated multi-point transmission

CP - cyclic prefix

CS - channel shortening

CSI - channel state information

DAC - digital-to-analog converter

DDSIC - decision-directed successive interference cancellation

DFE - decision feedback equaliser

DFT - discrete Fourier transform

DSP - digital signal processing

DVB-S2 - digital video broadcasting satellite second generation

eMBB - enhanced mobile broadband

ETSI - European telecommunications standards institute

EVD - eigenvalue decomposition

FD - frequency domain

FTN - faster-than-Nyquist

FFT - fast Fourier transform

FIR - finite impulse response

FPGA - field programmable gate array

I-branch - in-phase branch

ICI - inter-carrier interference

IDFT - inverse discrete Fourier transform

IF - intermediate frequency

IFFT - inverse fast Fourier transform

IDFT - inverse discrete Fourier transform

IQI - I/Q imbalance

ISI- inter-symbol interference

ITU - international telecommunications union

IOTA - isotropic orthogonal transform algorithm

LDPC - low-density parity-check

LO - local oscillator

LOS - line-of-sight

LTE - long term evolution

MAP - maximum a posteriori probability

MF - matched filter

MIMO - multiple-input multiple-output

MMSE - minimum mean square error

mMTC - massive machine-type communications

mmWave - millimeter-wave

MSE - mean-square-error

NLOS - non-line-of-sight

OFDM - orthogonal frequency division multiplexing

OTFS - orthogonal time frequency space

PDF - probability density function

PEP - pairwise error probability

PSD - power spectral density

QAM - quadrature amplitude modulation

Q-branch - quadrature-phase branch

QC - quasi-cyclic

QPSK - quadrature phase shift keying

QRD - QR decomposition

RF - radio frequency

RRC - root-raised-cosine

SC-FDE - single carrier frequency domain equalisation

SISO - soft-input-soft-output

SNR - signal-to-noise ratio

SSSSE - successive symbol-by-symbol sequence estimator

SSSgbKSE - go-back K sequence estimator

SVD - singular value decomposition

Tbps - Terabyte per second

TD - time domain

TDD - time division duplex

TDL - tapped delay line

TFO - time and frequency offset

THP - Tomlinson-Harashima precoding

UMa - urban macrocell

uRLLC - ultra-reliable and low latency communication

VA - Viterbi algorithm

VR - virtual reality

ZF - zero forcing

Notations

Bold letters denote matrices and vectors.

$(\cdot)^{\mathbf{T}}$ denotes the transpose operation.

$(\cdot)^{*}$ denotes the conjugate operation.

$(\cdot)^{\mathbf{H}}$ denotes the conjugate transpose operation.

$\mathbf{X}_{MN}$ indicates an MN by MN matrix.

$\mathbf{I}_{N}$ denotes an N by N identity matrix.

$\mathbf{F}_{N}$ and $\mathbf{F}_{N}^{\mathbf{H}}$ denote the N-point normalised DFT matrix and IDFT matrix respectively.

$*$ denote the linear convolution operation.

$\mathbf{I}_{MN}$ and $\mathbf{O}_{MN}$ denote MN by MN matrices with all 1 and 0 elements respectively.

$\mathrm{diag}\{\mathbf{X}\}$ denotes extracting the diagonal elements from matrix $\mathbf{X}$ and $\mathrm{diag}\{\mathbf{x}\}$ denotes forming a diagonal matrix with vector $\mathbf{x}$.

$\otimes$ denotes Kronecker product respectively.

$\mathbf{X}(i,:)$ indicates the i-th row of $\mathbf{X}$ and $\mathbf{X}(:,j)$ indicates the j-th column of $\mathbf{X}$.

$\mathrm{Tr}\{\cdot\}$ indicates the trace of a matrix.

$\mathbb{E}[\cdot]$ indicates the ensemble expectation.

$\mathrm{Re}\{\cdot\}$ and $\mathrm{Im}\{\cdot\}$ indicate the real and imaginary parts of a complex-valued quantity, respectively.

List of Symbols

Table 1: Signals, Channel Representations and System Parameters

Symbols	**Definitions**
$s(t)$	Time domain continuous transmitted signal
$x(t)$	Time domain continuous FTN signal (after RRC filtering)
$r(t)$	Time domain continuous received signal
$w(t)$	Time domain continuous noise
$S(f)$	Frequency domain continuous transmitted signal
$X(f)$	Frequency domain continuous FTN signal (after RRC filtering)
$R(f)$	Frequency domain continuous received signal
$W(f)$	Frequency domain continuous noise
s_i	Time domain discrete transmitted signal
r_i	Time domain discrete received signal
h_i, τ_i, and ν_i	The path gain, delay and Doppler shift of the i-th path in a sparse P-path channel model
P	Number of multipaths in a sparse P-path channel model.
τ	Delay
ν	Doppler frequency shift

Symbols	**Definitions**
t	Time variables
f	Frequency variables
g_t	Transmitter-side IQI amplitude mismatch parameter
g_r	Receiver-side IQI amplitude mismatch parameter
θ_t	Transmitter-side IQI phase mismatch parameter
θ_r	Receiver-side IQI phase mismatch parameter
$u(t)$	Time domain RRC pulse
$h(\tau, \nu)$	Continuous delay-Doppler channel representation
$g(t)$	Time domain equivalent channel response
$G[k]$	Discrete frequency domain equivalent channel response element
$E[k]$	Discrete frequency domain equalisation matrix element
$H_\nu(f, \nu)$	Continuous frequency-Doppler channel representation
$H(f, t)$	Continuous time-frequency channel representation
M	Number of subcarriers in OFDM/OTFS symbol
N	Number of symbols per frame
α	Time acceleration factor
β	Roll-off factor of RRC filter
B	Bandwidth of transmitted signal
f_c	Carrier frequency
T	Duration of Nyquist symbol
L	Length of ISI channel impulse response of SSSSE and SSSgbKSE algorithms
L_{ISI}	Length of ISI channel impulse response of truncated VA
M_S	Number of survivors of M-BCJR algorithm

Symbols	**Definitions**
K_{max}	Maximum number of resolvable Doppler frequency shifts
v_{max}	Maximum speed
f_{max}	Maximum Doppler frequency
d_{max}	Maximum delay
L_{max}	Number of multipaths
Δf	Frequency resolution
F_s	Sampling rate
σ_s^2	Time domain signal power (the same as σ_x^2)
σ_w^2	Time domain noise power
γ_{in}	Input SNR before equalisation
γ_{out}	Output SNR after equalisation

Table 2: Matrices and Vectors

Symbols	**Definitions**
$\mathbf{r}$	Time domain received sequence
$\mathbf{s}$	Time domain transmitted sequence
$\mathbf{x}$	Time domain FTN signal sequence
$\mathbf{w}$	Time domain noise sequence
$\mathbf{H}$	Time domain channel matrix
$\mathbf{R}$	Frequency domain received sequence
$\mathbf{S}$	Frequency domain transmitted sequence
$\mathbf{W}$	Frequency domain noise sequence
$\mathbf{G}$	Time domain equivalent channel matrix
$\mathbf{H}_\nu$	Frequency-Doppler channel matrix
$\mathbf{h}$	Discrete version of $h(\tau, \nu)$
$\hat{\mathbf{s}}$	Estimate of $\mathbf{s}$
$\hat{\mathbf{S}}$	Estimate of $\mathbf{S}$
$\mathbf{E}$	Frequency domain MMSE matrix
$\mathbf{E}_\nu$	Doppler domain MMSE matrix
$\mathbf{X}$	FTN Data symbol matrix (after RRC filtering)
$\mathbf{x}$	FTN Data symbol vector (after RRC filtering)
$\mathbf{y}$	Received signal after MMSE equalisation
$\mathbf{P}$	Time domain transfer matrix

Symbols	**Definitions**
$\hat{\mathbf{s}}^i$	Hard-decided symbols in the i-th iteration of DDSIC
$\hat{\mathbf{y}}^i$	MMSE equalised symbols in the i-th iteration of DDSIC
$\mathbf{\Psi}$	Time domain interpolation matrix
$\mathbf{Q}$	Unitary matrix composed of eigenvectors of $\mathbf{H}_\nu^{\mathbf{H}}\mathbf{H}_\nu$
$\mathbf{V}$	Modulation matrix in general

Chapter 1

Introduction

Section 1.1 discusses the evolution of mobile networks, highlighting key technologies of next-generation wireless communication systems and the demands of future communications. Section 1.2 introduces the principle of faster-than-Nyquist signalling. Section 1.3 outlines the motivation for this research, including existing challenges and practical implementation issues. The proposed approaches and main contributions are summarized in Section 1.4, while the thesis organization is presented in Section 1.5.

1.1 Background

The fifth-generation (5G) deployments have been commercially launched by 2020, following a two-phase rollout strategy. Phase 1, completed in 2018 under the 3rd Generation Partnership Project (3GPP) Release 15, prioritized enhanced mobile broadband (eMBB) and ultra-reliable low-latency communication (URLLC) [1]. Phase 2, completed in 2019 through Release 16, expanded 5G capabilities to support additional services, including massive machine-type communications (mMTC) and higher frequency bands [2], [3]. 5G operates across a range of frequency bands, including sub-6 GHz microwave bands and millimeter-wave (mmWave) frequencies above 24 GHz [4], [5]. This dual-band approach balances wide coverage at lower frequencies with high capacity at higher frequencies, which is crucial for network densification and meeting the growing demand for high-speed data transmission[6].

Advanced technologies such as massive multiple-input multiple-output (MIMO), beamforming, and mmWave connectivity have demonstrated significant potential in improving spectral efficiency and network capacity [7], [8]. However, challenges remain, particularly in managing multi-cell interference, supporting high user densities, and overcoming signal propagation limitations associated with mmWave frequencies [9]. To address these issues, network operators are increasingly leveraging artificial intelligence (AI)-driven optimization techniques [10], [11], dynamic spectrum sharing [12], and coordinated multi-point transmission (CoMP) [13] to enhance performance. Moreover, as the deployment of standalone 5G networks progresses, edge computing [14] and network slicing [15] are expected to play crucial roles in enabling highly customized and low-latency services tailored to specific use cases, such as autonomous vehicles, industrial automation immersive augmented reality (AR), and virtual reality (VR) applications [16], [17].

3GPP Release 18, often regarded as the foundation for "5G-advanced", promises further enhancements in 5G performance, including more flexible spectrum utilization, improved energy efficiency, and increased support for diverse devices [18]. As mobile networks continue to evolve, key concerns for ongoing 5G deployments include meeting ambitious targets for peak data rates, ultra-reliable low-latency communication, and spectral efficiency [19]. Given the exponential growth of connected devices and data traffic, 5G systems must be designed to accommodate this surge without a proportional increase in energy consumption, which is a critical factor for mobile network operators striving for sustainable operations. Additionally, 5G rollouts face challenges related to infrastructure investment, spectrum allocation, and ensuring coexistence with existing technologies such as legacy long term evolution (LTE) networks [20]. Effective interference management, seamless inter-network handovers, and robust security mechanisms are essential for maintaining a high-quality user experience [21].

Looking ahead, the transition from 5G to the sixth-generation (6G) networks is already under discussion, with initial research focusing on technologies that will enable unprecedented levels of connectivity. 6G is expected to push beyond 5G capabilities by incorporating terahertz (THz) communications [22], AI-native network management [23], and quantum communication for enhanced security [24]. These advancements aim to achieve peak data rates exceeding 1 Tbps, ultra-low latency in the order of microseconds, and extreme energy efficiency to support the demands of future applications such as holographic communication, interconnected smart cities, and brain-computer interfaces [25], [26]. As industry and academia collaborate on 6G research, addressing challenges in hardware limitations, energy consumption, and regulatory frameworks will be crucial to realizing the full potential of next-generation wireless communication [27].

1.2 Principle of Faster-Than-Nyquist Signalling

According to the Nyquist criterion, to avoid inter-symbol interference (ISI), a baseband system must operate at a transmission rate no greater than twice the bandwidth of the ideal band-limited channel [28]. For many years, most systems obey this orthogonality condition. However, in the 1970s, J. E. Mazo challenged this limitation by introducing the concept of faster-than-Nyquist (FTN) signalling, a scheme that allows symbol rates to exceed the Nyquist rate. While this non-orthogonal transmission intentionally introduces ISI, Mazo demonstrated that FTN enables the transmission of approximately 25% faster than Nyquist transmission without impacting the bit error rate (BER) at the receiver [29]. Therefore, the key idea behind FTN is that the introduced ISI can be managed through advanced detection and equalisation techniques, allowing the system to exploit this "extra" capacity. As a result, FTN can achieve higher spectral efficiency and transmit more information over a given bandwidth compared to traditional Nyquist signalling. Despite the increased complexity in receiver design required to handle the ISI, FTN can significantly improve the performance of communication systems, making it attractive for use in bandwidth-constrained scenarios.

Figure 1.1 illustrates the transmitted waveforms consisting of 5 sinc pulses for both Nyquist signalling and FTN signalling. For Nyquist signalling, pulses are transmitted at intervals of T, while for FTN signalling, they are transmitted at intervals of αT, where α denotes the time acceleration factor for FTN signalling, $0 < \alpha < 1$. It can be observed from the figure that with time acceleration, ISI inevitably occurs at sampling points. Compared to those ISI induced by multipath transmission, the FTN-induced ISI is predictable and can be cancelled with effective methods.

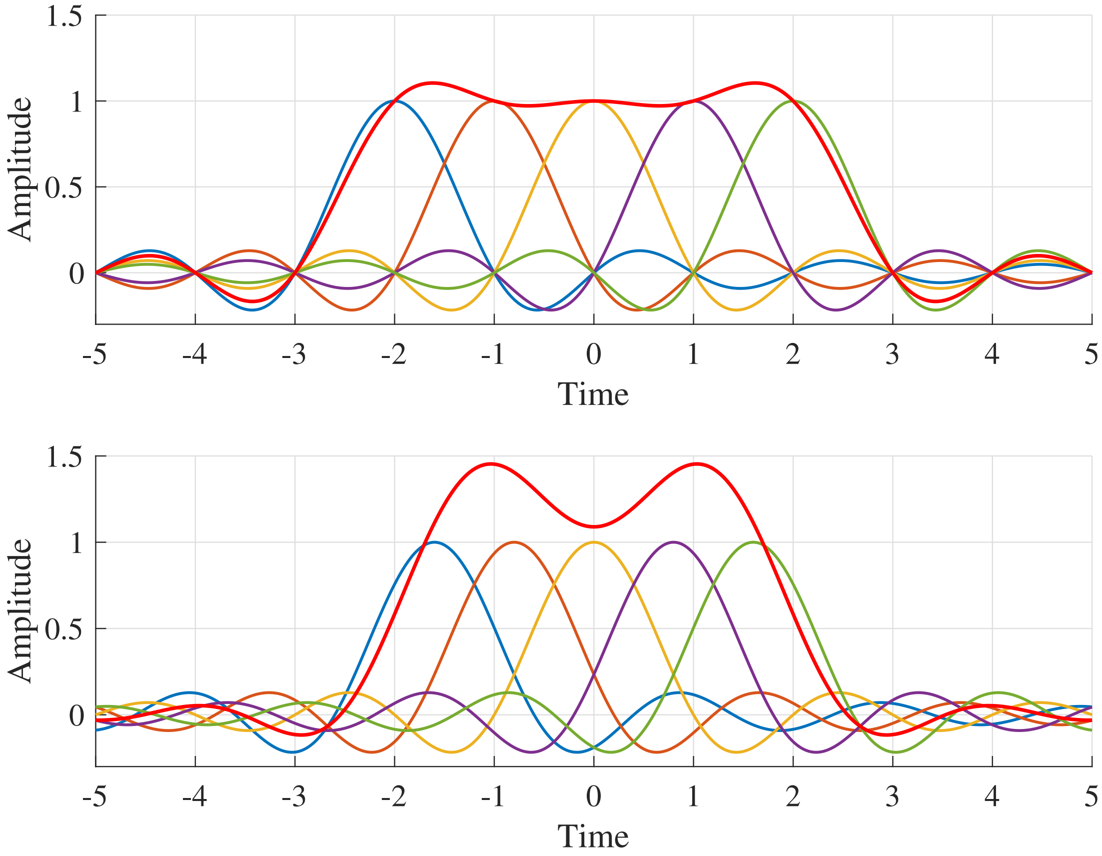

Figure 1.1: Transmitted waveforms with Nyquist signalling (upper) and FTN signalling adopting $\alpha = 0.8$ (lower), where the sampling points correspond to the central peak positions of each sinc pulse.

Mazo's idea of fast pulses remained dormant for 30 years until researchers began questioning potential losses in quadrature pulses and the relationship between channel capacity and signal spectrum. Studies such as [29], [30] suggest that both the main lobe and stopband of the power spectral density (PSD) contribute to information transmission, challenging conventional bandwidth-energy-error performance theories.

In addition, the Shannon limit defines the maximum transmission rate achievable under white noise conditions. While always approached, this theoretical boundary has never been surpassed. In the context of 5G and 6G research, the notion that FTN can surpass the Shannon limit remains a topic of debate, making FTN both appealing and controversial.

1.3 Motivations

The advancement of FTN signalling should aim at developing low-complexity anti-ISI techniques. Moreover, FTN research should be grounded in considerations of practical implementation. Several challenges need to be addressed to realise the full potential of FTN signalling in real-world applications, which are the motivations of this thesis.

1.3.1 Problems in Existing Methods

Since FTN signalling intentionally introduces ISI into data transmission, a key research focus has been on developing efficient ISI mitigation techniques within a low-cost architecture. In previous studies [31], [32], most design efforts have concentrated on the receiver side. Specifically, FTN-induced ISI can be mitigated through a combination of equalisation, decoding, and subsequent cancellation algorithms.

Finite zero-forcing (ZF) equalisation is the simplest form of equalisation. Its primary objective is to truncate the infinite ZF equaliser and convert it into a finite impulse response (FIR) filter. However, a notable limitation of finite ZF equaliser is its inability to fully remove residual ISI, leading to noise amplification. This makes finite ZF equaliser viable only in scenarios with a high signal-to-noise ratio (SNR). At lower SNR regions, noise amplification results in poor performance, thus limiting its effectiveness. Salz et al. first introduced the concept of the decision feedback equaliser (DFE) in [33], which enhanced a conventional linear equaliser by incorporating a feedback module. The feedback coefficients were designed to mirror the overall impulse response, ensuring a minimised mean-square error (MSE) between the linear equaliser's impulse response and the transmitting filter response. This adjustment resulted in a DFE with a lower MSE than a traditional linear equaliser, making it a more effective choice for ISI mitigation. In MMSE equalisation, the optimal inverse matrix is derived by minimising the correlation between the received signal and the error. This approach offers a distinct advantage over the ZF equalisation, as MMSE equalisation provides better reliability, especially in low SNR conditions. Furthermore, frequency domain equalisation (FDE) is often preferred over time-domain equalisation due to its reduced computational complexity. MMSE equalisation can be efficiently adapted for FD. In 2013, Sugiura et al. pioneered the use of MMSE-aided FDE by introducing cyclic prefixes (CP) after each modulated symbol [34]. This structure transformed the tap-coefficient matrix into a circulant form, enabling eigenvalue decomposition. Through eigenvalues and a diagonal matrix, the fast Fourier transform (FFT) coefficients were derived, allowing the equalisation process to be shifted to FD. This method proved especially beneficial for long-tap scenarios, significantly reducing computational complexity. However, it performed less effectively at high transmission rates.

Beyond equalisation, decoding algorithms also play a critical role in mitigating ISI in FTN systems. Decoding schemes such as the Viterbi algorithm (VA) [35] and the Bahl-Cocke-Jelinek-Raviv (BCJR) algorithm [36] have formed the basis for maximum likelihood and maximum *a posteriori* (MAP) detection, respectively. In the context of FTN applications, these algorithms are often modified to balance performance and complexity. The truncated version of Viterbi equalisation, as employed in [31], reduces complexity by symmetrically truncating the infinite waveform and disregarding segments with negligible frequency response. In practice, however, the truncated length often remains substantial, leading to high computational complexity in the VA.

Colavolpe et al. introduced the sum-product algorithm for MAP symbol detection [37]. This approach allows for a linear increase in complexity relative to the number of interfering symbols. However, the model is based on an FD multiplexing system, where frequency overlap can lead to severe inter-carrier interference (ICI). Anderson et al. enhanced the M-BCJR algorithm by utilising Forney's observation model [38]. In their work, they streamlined the algorithm by removing states with redundant and low-probability values [39]. However, Forney's model primarily assumes white noise, which complicates the derivation of a whitening filter. To address this limitation, Li et al. proposed a simplified M-BCJR algorithm based on the Ungerboeck observation model. However, this approach is effective only within a specific range of ISI, and the parameters for path selection vary depending on channel conditions.

In 2012 and 2013, Rusek et al. introduced a channel shortening (CS) algorithm in two studies [40], [41]. The primary objective of CS is to calculate the front-end filter and target response in the frequency domain, maximising the power within the shortened channel. However, due to its FDE operation, CS performs less effectively than time domain (TD) equalisation algorithms in high-rate transmission scenarios.

In addition, the pre-techniques, which aim at processing cancellation on the transmitter side, are also demonstrated to be effective in FTN systems. In [42], a linear pre-equaliser was introduced to reduce ISI, complemented by a spectral precoder to prevent spectral broadening. Ishihara et al. applied an eigenvalue-decomposition-based precoder to achieve optimal power allocation and enhanced BER performance in frequency-selective channels [43]–[45]. In a related study, Li et al. proposed a precoding-based channel estimation and data detection method aimed at improving system performance [46]. Wang et al. presented an adaptive FTN scheme that dynamically adjusts the mapping order, code rate, and sampling rate [47]. These transmit-side approaches open new avenues for reducing the complexity of ISI cancellation and enhancing system capacity. However, achieving full-diversity transmission without channel coding remains an unexplored area in these studies. Further research is necessary to explore innovative transmit-side techniques for uncoded FTN transmissions, aiming to counteract fast fading without solely relying on the addition of redundant information in the transmitted signal.

1.3.2 Practical Implementation Challenges

FTN signalling is currently undergoing a critical transition from theoretical research to practical implementation. Real-world deployment requires robust performance in fast-fading environments, including both multipath non-line-of-sight (NLOS) and line-of-sight (LOS) channels. Additionally, hardware impairments, particularly in radio frequency (RF) signal transmission, present significant challenges that cannot be overlooked.

To facilitate successful real-world adoption, it is essential to address several key implementation challenges that affect both algorithmic robustness and hardware reliability. The following outlines two primary obstacles of FTN systems:

- *Challenge 1:* **Effectiveness in Fast-Fading Channels**

  In fast-fading multipath channels, the adverse effects of Doppler shift result in frequency uncertainty and continuously time-varying channel state information (CSI) [48]. These factors significantly increase the challenges associated with both equalisation and interference cancellation. Consequently, mitigating the Doppler effect is a crucial prerequisite for achieving high-integrity FTN data recovery.

  In the study of multipath fading channels, the diversity order is regarded as a crucial metric for assessing the system's ability to accurately recover transmitted signals. It represents the "degree of freedom" and plays a pivotal role in quantifying the average pairwise error probability (PEP) [49]. Ideally, a system should achieve full diversity order to ensure high-integrity recovery of transmitted signals. However, conventional FTN schemes are short of attaining full diversity due to the inherent non-orthogonal signalling, which compromises the reliability of data recovery. Consequently, it is essential to develop techniques that either enhance the diversity order or mitigate the adverse effects of multipath transmission.

- *Challenge 2:* **Hardware Impairments**

  While numerous FTN systems and ISI cancellation methods, such as [33], [37], [38], are effective in simulations, there is still relatively limited research on hardware implementation. This gap is largely due to the complexities introduced by hardware impairments. In addition to conventional ISI, hardware-induced distortions—such as in-phase and quadrature-phase imbalance (IQI), phase noise, and amplifier nonlinearities—exacerbate interference challenges, necessitating more robust and computationally efficient interference cancellation techniques.

Dasalukunte et al. first explored the potential for hardware implementation of FTN signalling. They proposed a multicarrier FTN system designed for 65 nm complementary metal-oxide semiconductor (CMOS) and field programmable gate array (FPGA) platforms [50], [51]. This architecture utilised an isotropic orthogonal transform algorithm (IOTA) basis and a look-up table to approximate orthogonal transmission. Jana et al. extended this work by incorporating RF transmission modules, including up-conversion and down-conversion, into FTN systems [52]. This system relies heavily on dual-polarised coding, which ensures robustness under high-order modulation.

However, these studies do not address practical impairments such as transmitter and receiver IQI, carrier frequency offset (CFO), phase noise, and nonlinearity-induced interference [53]. To address these issues, the architecture of existing FTN systems requires further refinement, and interference cancellation techniques must be adapted to handle a broader range of interference sources effectively.

1.4 Approaches and Contributions

While extensive research has been conducted on FTN systems in terms of ISI cancellation and performance analysis, as discussed in Section 1.3, several practical challenges remain unresolved. These include computational complexity in high-density signalling, robustness under fast-fading environments, and vulnerability to hardware impairments. To address these limitations, this thesis proposes a frame-based decision-directed successive interference cancellation (DDSIC) algorithm that can effectively eliminate ISI in both additive white Gaussian noise (AWGN) and slow-fading channels. The frame-based structure is adopted to balance processing efficiency and system flexibility. Unlike symbol-by-symbol detection schemes, frame-based processing allows simultaneous operations using FFT/DFT, which significantly reduce computational burden while supporting pipelined or parallel hardware implementation. Additionally, the proposed architecture is extended to fast-fading environments leveraging an adaptive transmit precoding (ATPC) technique to enhance diversity performance across OFDM, single-carrier frequency-domain equalisation (SC-FDE), and orthogonal time-frequency space (OTFS) modulation schemes when integrated with faster-than-Nyquist (FTN) signalling. Remarkably, the ATPC-aided system achieves performance in fast-fading channels comparable to that in slow-fading scenarios with perfect CSI, ensuring the sustained efficacy of the DDSIC algorithm.

Moreover, the proposed FTN framework is considered implementable in practical systems due to its low computational complexity, high efficiency, and strong robustness against both fast-fading and hardware impairments such as IQI. These characteristics make the design well-suited for hardware-constrained platforms like RF front-ends or baseband processors. The algorithm's performance has been rigorously validated through simulation under realistic channel and hardware conditions, further supporting its practical feasibility and application potential in future broadband wireless systems. The key contributions of this thesis are summarized as follows.

- *Contribution 1:* **A Novel Low-Complexity Frame-Based DDSIC Algorithm**

  To address the high computational complexity of symbol-by-symbol detection methods in FTN systems, an FTN system with a novel DDSIC algorithm is established and investigated in Chapter 3.

  At the transmitter side, the input data is generated and mapped by M-array quadrature amplitude modulation (M-QAM), divided into frames and then sent frame-by-frame. Data symbols are transmitted at a rate faster than Nyquist transmission, resulting in intentional ISI. A root-raised-cosine (RRC) filter is applied for pulse shaping, which cuts the FTN bandwidth to Nyquist bandwidth.

  At the receiver side, the DDSIC algorithm is applied to eliminate ISI and process symbol detection. The first stage of DDSIC is the FD-MMSE equalisation and the second stage is successive interference cancellation. Instead of using traditional matched filtering, MMSE helps prevent noise enhancement and reduces ISI. The key advantage of using MMSE in FD is that it transforms convolution operations into multiplications using discrete Fourier transform (DFT) and/or inverse discrete Fourier transform (IDFT), thereby reducing computational complexity. In subsequent iterations, the detected symbols are iteratively regenerated, and ISI is successively removed. The difference between the received signal and the regenerated signal after interference cancellation represents the residual ISI, which is used in the next iteration. The complexity is also reduced since the proposed system is linear, and thus the regeneration process of DDSIC is simplified into a multiplication of the signal vector and transfer matrix. Furthermore, the signals are transmitted and processed frame-by-frame, which saves complexity than symbol-by-symbol methods such as the successive symbol-by-symbol sequence estimator (SSSSE) and the go-back K sequence estimator (SSSgbKSE) in [54].

Additionally, this chapter provides a theoretical analysis of the BER for each DDSIC iteration. Based on the power of each decomposed component, the theoretical BER expressions for each iteration and a BER lower bound where ISI is assumed to be completely removed are derived. These theoretical analyses are used to validate the efficacy of the DDSIC algorithm and establish its performance compared to other methods. Simulation results demonstrate that MMSE equalisation significantly outperforms conventional matched filtering, particularly in mitigating inter-symbol interference (ISI). A systematic investigation of the time acceleration factor reveals the minimum threshold at which the proposed DDSIC algorithm effectively suppresses ISI without incurring significant BER degradation. Furthermore, DDSIC is benchmarked against state-of-the-art detection methods, including SSSSE, SSSgbKSE, truncated Viterbi, and M-BCJR algorithms. The proposed DDSIC algorithm achieves a superior complexity-performance trade-off, consistently outperforming symbol-by-symbol approaches in both AWGN and multipath fading channels. When combined with low-density parity-check (LDPC) coding, DDSIC exhibits further performance enhancements, delivering substantial BER improvements across all evaluated channel conditions.

This contribution has been published in [C-1] and [J-1].

- *Contribution 2:* **Implementation Extension to Fast-Fading Channels**

To ensure robust FTN transmission under more realistic channels, Chapter 4 tackles the impact of the Doppler effect and time-varying CSI on conventional data detection under fast-fading multipath channels and proposes an adaptive FTN transmission system to address this problem.

This system leverages the ATPC method to mitigate Doppler-induced impairments, enhancing the resilience of FTN systems. Different modulation schemes are also discussed, including the integration of OFDM, SC-FDE, and OTFS with FTN signalling, and their compatibility with fast-fading multipath channels. The ATPC method utilises the eigenvalue decomposition of FD channel matrix to construct an adaptive precoding matrix, which effectively mitigates Doppler shift and transforms the fast-fading channel into a slow-fading equivalent, facilitating ISI cancellation. The MMSE equaliser is employed to reduce the impact of fast-fading multipath channels, while DDSIC is used to iteratively mitigate ISI. This chapter also provides closed-form BER expressions for two extreme channel conditions: infinite multipath without Doppler shifts, representing a high-frequency diversity scenario, and infinite Doppler frequencies with full multipath diversity, representing a high-time diversity scenario. These extreme cases provide useful benchmarks for evaluating the performance of FTN systems under varying degrees of channel impairments.

In simulation results, the system shows robust performance with increasing Doppler shifts, demonstrating the effectiveness of ATPC. Although it is concluded that OFDM-FTN fails in achieving frequency diversity and SC-FDE-FTN fails in achieving time diversity, with the aid of ATPC, the two schemes are converted into a short-frame adaptive scheme that can achieve both time and frequency diversities. Also, OTFS is converted into a long-frame adaptive scheme, which improves its BER performance under the same scenarios [55]. The proposed system is compared to conventional techniques such as truncated Viterbi and turbo-BCJR. The ATPC-aided DDSIC shows superior performance, especially in high SNR regions, highlighting its robustness.

This contribution has been published in [J-2].

- *Contribution 3:* **Consideration of I/Q Imbalance in Broadband Wireless Systems**

  To improve the hardware applicability of FTN systems, Chapter 5 presents the challenges of I/Q imbalance in FTN systems, which introduces significant distortions due to amplitude and phase mismatches in the I and Q branches.

Although prior research has focused on mitigating ISI in FTN systems, the impact of IQI, which is a key impairment caused by analog front-end imperfections, particularly in direct-conversion architectures, has largely been overlooked. To address this research gap, an FTN system that considers the effects of IQI caused by direct-conversion architecture is established. The transmitted signal undergoes up-conversion and down-conversion, which are modeled using lowpass filters (LPFs) for each branch, taking into account amplitude and phase mismatches. The signal model is extended to an extended-dimension space, representing both original and image signals and providing a framework to effectively model and analyse the impact of IQI. This model serves as the foundation for the joint ISI and IQI cancellation algorithm. It allows the equaliser to simultaneously address interference from both ISI and IQI. The robustness of the proposed scheme is evaluated under various IQI scenarios, including mild, medium, and severe IQI.

Simulation results indicate that the DDSIC algorithm effectively mitigates IQI, with minimal performance degradation in realistic scenarios. Moreover, the improved DDSIC algorithm is compared with existing algorithms such as the truncated Viterbi algorithm in [56] and the M-BCJR algorithm in [57]. The results demonstrate that the DDSIC achieves superior BER performance after only a few iterations, with lower computational complexity. The proposed scheme is also tested with LDPC coding, which significantly improves the BER performance under various channel conditions, further demonstrating its practical applicability.

This contribution has been published in [C-2] and [J-3].

1.5 Thesis Organisation

This thesis is organised as follows.

Chapter 2 conducts a literature review. Additionally, it presents the principle of FTN signalling, fast-fading transmission and IQI problem.

Chapter 3 presents the structure of the proposed FTN system and the integration of ISI cancellation modules. The equivalent channel is modeled as a circular convolution matrix, facilitating low-complexity estimation through FD-MMSE equalisation. Building on these foundations, a novel frame-based DDSIC algorithm is introduced for practical implementation. To demonstrate the advantages of the proposed algorithm, a complexity analysis is conducted, comparing it with conventional symbol-by-symbol methods. Additionally, theoretical BER expressions and a BER lower bound are derived for performance evaluation. Finally, simulation results are provided to validate the theoretical analyses, showcasing the proposed method's ability to achieve lower complexity and superior performance compared to state-of-the-art techniques.

Chapter 4 presents an adaptive FTN signalling scheme over fast-fading channels. To investigate the potential of FTN systems under fast-fading transmission conditions, both the time and frequency diversity are analysed in terms of three modulation schemes: OFDM, SC-FDE, and OTFS. Each of these modulation schemes is evaluated in combination with FTN signalling. To ensure the effectiveness of the algorithm in fast-fading channels, an adaptive precoding scheme is proposed aimed at mitigating the Doppler effect and transforming time-varying CSI into statistical representations. Finally, the BER performance is compared across various configurations, including precoded and non-precoded schemes, as well as long-frame and short-frame transmission schemes.

Chapter 5 introduces an IQI-aware FTN system aided by a joint interference cancellation algorithm. To address the analog front-end IQI problem, an extended-dimension signal model is proposed, and the ISI cancellation algorithm is improved to perform joint interference cancellation, enabling simultaneous removal of both ISI and IQI. Additionally, theoretical BER expressions for each iteration and a BER lower bound are derived for performance evaluation. Simulation results are presented to verify the accuracy of these theoretical results and to benchmark the performance of the proposed scheme against other existing methods.

Finally, conclusions are drawn, some open issues are discussed and some research directions for future work are presented in Chapter 6.

Chapter 2

Literature Review

FTN signalling is a key technology in 5G communication, offering enhanced spectral efficiency and transmission speed. This review comprehensively surveys FTN studies and is structured into five sections. First, it outlines the development of FTN signalling. Second, it reviews existing FTN system technologies. Third, it examines state-of-the-art FTN advancements in fast-fading channels. Fourth, it discusses challenges and solutions for I/Q imbalance in FTN systems. Finally, it presents the basic FTN system framework and signal models.

2.1 Development of FTN Signalling

Mazo's proposal on FTN signalling [29] initially garnered limited attention primarily due to constrained hardware capabilities and the absence of pressing demand for high-speed data transmission during that era. During the subsequent decades (from the late 1970s to the early 2000s), only a handful of studies emerged, focusing on foundational aspects such as theoretical FTN systems with QAM [58], energy derivation for FTN signals [59], and the characterization of minimum Euclidean distance in FTN frameworks [60]. Although these contributions established a theoretical groundwork for FTN signaling, research soon entered a prolonged dormant phase, hindered by insufficient technological advancements and computational resources. The prohibitive complexity of transceiver designs at the time rendered ISI mitigation infeasible, leading many to dismiss FTN as impractical. Consequently, subsequent studies during this period primarily focused on incremental refinements to Mazo's work, such as pulse shaping optimization [59] and further analysis of minimum Euclidean distance [60].

In recent decades, with increasing demands for higher throughput and spectral efficiency, coupled with the emergence of other advanced technologies, FTN signalling has re-emerged as a promising candidate in future-generation wireless communication systems. Advancements in signal processing have also made it possible to achieve effective ISI cancellation and accurate data recovery in FTN systems. As a step in this direction, FTN signalling was integrated with the International Telecommunications Union (ITU) V. 92 modem in [61], where an MMSE equaliser was employed. Through multiple iterations, the proposed equaliser demonstrated robust performance across various challenging channel conditions.

In further exploration of FTN signalling, Anderson et al. made significant contributions. While earlier research primarily focused on TD FTN signalling, the studies in [62], [63] expanded the exploration into FD transmission by adapting the concept of OFDM for FTN signalling. Using the FFT, the authors introduced a multicarrier strategy known as MFTN, representing a novel direction in FTN research. In this approach, data is divided into multiple streams, each decoded independently. Similar to TD-FTN, the frequency intervals of each stream are reduced, resulting in overlapping frequency carriers and, consequently, non-orthogonal signalling.

Furthermore, a novel receiver incorporating a truncated VA and turbo equalisation was proposed in [56]. By employing a discrete-time model, this design reduced computational complexity while maintaining an equivalent BER. Compared to the Nyquist system, this approach achieved a 30% reduction in the required bandwidth.

To further enhance FTN decoding, Rusek et al. introduced a sub-optimal iterative BCJR decoder at the receiver side [64]. This decoder utilised a time-frequency grid to facilitate time-frequency separation and projection using discrete Fourier transform (DFT) and inverse fast Fourier transform (IFFT). With this innovative receiver design, the system's throughput was shown to be twice that of orthogonal Nyquist signalling, presenting a promising potential for hardware implementation.

2.2 Existing Technologies in FTN Systems

As discussed in Chapter 1, the primary challenge in FTN research lies in developing low-complexity, high-efficiency methods for mitigating ISI. Existing technologies in FTN systems are mainly divided into four aspects:

- **Optimisation of Conventional Approaches**

  Conventional approaches, such as the VA [65] and the BCJR algorithm [66], require computational complexity far exceeding practical limits. Their reduced-complexity alternatives, such as the truncated VA [56] and the M-BCJR algorithm [67], have been demonstrated to facilitate accurate data recovery adopting binary phase shift keying (BPSK) modulation in AWGN channels. However, the application of these two algorithms is restricted when employing higher-order QAM modulations. This limitation arises because both algorithms have to traverse all possible states when decoding received symbols, with the number of states increasing exponentially as the modulation level rises. Similarly, the truncated VA, as employed in [31], symmetrically truncates the infinite waveform while disregarding components with negligible frequency response.

  However, the truncated length remains substantial in practice, leading to high computational complexity in VA. Furthermore, this method becomes ineffective when the truncated portion contains essential information that cannot be overlooked. To address this, Franz et al. refined the M-BCJR algorithm based on the Forney observation model in [38] by eliminating redundant small-probability states [39]. However, the Forney observation model only accounts for white noise, making the derivation of a whitening filter challenging. To overcome this limitation, Li et al. proposed a simplified M-BCJR algorithm based on the Ungerboeck observation model [68]. Instead of computing both forward and backward metrics, this approach considered only limited backward metrics along a specific path, requiring the selection of the correct path in advance. Despite its improvements, the algorithm is effective only within a restricted ISI range, and the parameters for path selection vary depending on channel conditions.

- **Matrix-Computation-Based Estimation Techniques**

Several alternative methods aim to reduce complexity through matrix decomposition techniques. In 2014, Baek et al. proposed a novel interference cancellation scheme based on ISI QR matrix decomposition, assuming that ISI primarily affected two adjacent symbols [69]. However, it was not feasible to account for the entire infinite ISI trellis. Instead of detecting symbols individually, they were grouped and detected sequentially. A small ISI matrix was selected for QR decomposition at each step, leading to the development of the partial decision feedback equalisation (DFE) scheme. Despite this approach, the computational complexity remained high. Later in [70], an improved scheme was introduced, incorporating a QR decomposition-M algorithm based on BCJR. This version selected branch metrics based on the minimum Euclidean distances between received signals and feedback. By considering interference from N adjacent symbols, the complexity significantly increased compared to the original two-symbol approach. Simulation results demonstrated that QR matrix computation performance could approach that of the BCJR algorithm, with a 10% reduction in system complexity. However, when the block size exceeds several hundred, QRD-based algorithms encounter impractically high computational complexity.

In contrast, algorithms based on singular value decomposition (SVD), such as those in [71]–[73], have demonstrated promising performance in ISI cancellation. SVD allows for a more simplified representation of the channel model, facilitating analysis of Euclidean distance and signal power. Similarly, eigenvalue decomposition (EVD)-based algorithms [34], [44], [74], [75] substantially reduce computational complexity, particularly when the transformed channel matrix is Hermitian.

- **Symbol-based ISI Cancellation Methods**

To handle long-block FTN signals, several symbol-based methods have been proposed in the time domain. In [54], an SSSSE method is introduced along with its enhanced version, the SSSgbKSE method. The core idea of SSSSE is to calculate the ISI matrix after matched filtering and then cancel ISI on a symbol-by-symbol basis, using each estimated ISI component. SSSgbKSE builds upon SSSSE by re-estimating each symbol based on the previous K estimated symbols to improve accuracy. Both methods rely heavily on the precise estimation of the first symbol, addressing only interference from preceding symbols due to the system's causality, while neglecting interference from future symbols. Consequently, these methods face challenges under stringent FTN conditions (characterised by a low acceleration factor) or when using higher modulation levels.

- **Integretion with Advanced Technologies**

  FTN signalling also integrates well with next-generation technologies such as MIMO and non-orthogonal multiplex access (NOMA). For example, Park et al. combined FTN with a MIMO digital-video-broadcasting-satellite-second-generation (DVB-S2)-based satellite communication system, employing turbo coding and a BCJR soft-decision FTN structure, which demonstrated a performance gain of up to 30% [76]. Wen et al. evaluated the ergodic capacity of MIMO-FTN systems under fast-fading channels, demonstrating that the multicarrier-induced inter-tap correlation and ISI can both be effectively mitigated to an acceptable level. On the other hand, Yuan et al. introduced factor graph-based algorithms to mitigate both ISI and inter-user interference in FTN-NOMA systems. Additionally, sparse code multiple access (SCMA) was explored as a potential integration with FTN signalling [77], [78]. The integreation of FTN and advanced 5G technologies further enhances spectral efficiency without degrading the system performance, which is a promising direction of FTN study.

Consequently, although FTN-induced ISI is a well-known problem in digital communications, the methods developed in conventional systems do not directly apply or remain effective in the FTN context. This is due to the intentional violation of orthogonality and the resulting tightly packed signal structure in FTN systems, which leads to more severe and structured ISI. The aim of this thesis is therefore to develop novel, low-complexity, and implementable solutions specifically tailored to FTN systems. The proposed framework—including the frame-based DDSIC algorithm, adaptive precoding schemes, and compensation for hardware impairments—contributes to making FTN signalling viable for future practical deployment. This thesis addresses the key challenge of balancing performance, complexity, and robustness, which remains insufficiently resolved in existing literature.

2.3 FTN Systems over Fast-Fading Channels

The study of FTN signalling over fast-fading channels is crucial due to the dynamic nature of wireless environments, where rapid channel variations pose significant challenges to reliable communication. Fast-fading channels are characterized by time-varying multipath propagation effects, resulting in fluctuations in signal amplitude and phase. These variations introduce additional complexity in FTN signal detection and equalisation, necessitating robust receiver designs that can mitigate the combined effects of ISI and fading. Moreover, in fast-fading scenarios, Doppler shift results in continuously varying CSIs in each frame, which is a significant challenge for conventional equalisation and interference mitigation. For example, most of the conventional works focusing on AWGN channels [54], [74], [79], [80] lose their effectiveness under varying channel conditions. In [74], the data recovery highly relies on accurate CSIs, and thus the CSI uncertainty will destroy the robustness of this system while transmitting over fast-fading channels. To solve this problem, real-time channel estimation as well as fast-fading effects cancellation are potential solutions.

- **Channel-Coding-Aided Detectors**

  With the aid of channel coding techniques, some FTN schemes originally designed for AWGN environments can work effectively in fast-fading conditions, achieving comparable performance to those in AWGN environments. These conventionally schemes include the truncated BCJR algorithm [81], FD equalisation [82], [83], multicarrier transmission methods [84], the turbo soft detector [84]–[86], and expectation propagation-based decoders [87]. Additionally, joint channel estimation and equalisation schemes have demonstrated the ability to achieve accurate CSI acquisition with channel coding. However, how to reduce computational complexity is a tough issue in these coded scenarios. In particular, the work presented in [88] addresses this by truncating both the ISI and inter-carrier interference (ICI) vectors and applying eigenvalue decomposition to the equivalent interference matrix, thus significantly reducing the overall complexity. In [89], the multicarrier

FTN system without inserting CP achieves good robustness in fast-fading transmission. This scheme integrate open-loop differential and modulation and coherent demodulation, whereas the application of turbo coding requires further complexity in multicarrier environment. Similarly, Yuan et al. explored the capacity of multicarrier FTN systems under fast fading channels in [90], which transformed the posterior distribution to facilitate the use of FD-MMSE equalisation.

- **Transmitter-Side Pre-Methods**

Conversely, several transmitter-side techniques, such as precoders [44], [46] and pre-equalisers [42], have been proposed to avoid the additional complexity associated with channel coding design.

Tomlinson-Harashima Precoding (THP), which is first introduced in [91], is a nonlinear pre-equalisation technique. It employs a feedback filter to cancel interference, followed by a modulo operator that keeps the transmitted signal within a predefined range, reducing power fluctuations. At the receiver, a corresponding feedforward filter and another modulo operator are used to recover the transmitted symbols while maintaining signal integrity. Recent studies [42], [92] have explored the application of THP in combating Doppler effects and avoiding spectral broadening, demonstrating its effectiveness in enhancing performance under fast-fading channels. However, the effectiveness of THP strongly relies on the availability of accurate CSI at the transmitter. Without precise CSI, the interference prediction and cancellation at the transmitter become unreliable, significantly degrading the overall system performance. This requirement makes THP particularly sensitive in scenarios involving high mobility or rapidly varying channels.

Additionally, as highlighted in [93], transceiver design can be simplified by determining the weight matrix of the precoder at the receiver. Ishihara et al. employ an EVD-based precoder for optimal power allocation, thereby enhancing BER performance in frequency-selective channels [44]. Li et al. [46] introduce a precoding method integrated with channel estimation and data detection to improve system performance. Wang et al. further propose an adaptive FTN scheme that allows dynamic adjustments of mapping order, code rate, and sampling rate [47]. Note that dispersive Rayleigh channels, as considered in most existing works [83], [87], [88], lack the generality required for a comprehensive analysis of fast-fading scenarios. In fast-fading environments, diversity order becomes significantly more challenging to analyse, as it depends on the multipath components, each of which exhibits non-uniform and time-varying power levels.

Moreover, all the above precoding schemes suffer considerable performance degradation when the available CSI is inaccurate or outdated. In practice, CSI at the transmitter is often obtained through feedback from the receiver, which may incur latency or quantisation errors, especially in high-mobility scenarios. As a result, mismatches between the assumed and actual channel conditions can lead to incorrect interference prediction and suboptimal precoding. Similarly, the accuracy of MMSE-based or SIC-based detectors at the receiver is heavily dependent on precise CSI, where errors in the estimated channel matrix directly affect the equalisation and interference cancellation performance. Therefore, robust FTN receiver designs must account for such imperfections, potentially through adaptive or predictive CSI tracking mechanisms. To address these challenges, advanced CSI acquisition techniques such as pilot-aided estimation [94], Kalman filtering [95], or deep learning-based prediction [96], [97] can be employed to enable real-time CSI tracking even under rapidly varying channel conditions.

2.4 I/Q Imbalance Problem

Besides fast-fading transmission, another significant aspect that must be focused on for practical implementation is broadband wireless broadcasting. In particular, for successful deployment, the challenges introduced by hardware impairments must be effectively addressed. I/Q imbalance is a critical issue in modern communication systems that utilize quadrature modulation, such as QAM and OFDM, where signals are represented by I and Q components. It arises due to hardware imperfections, such as mismatches in the amplitude and phase of the I and Q branches, often caused by non-ideal local oscillators, mixers, or analog components. This imbalance leads to signal distortion, mirror frequency interference, reducing system perfor-

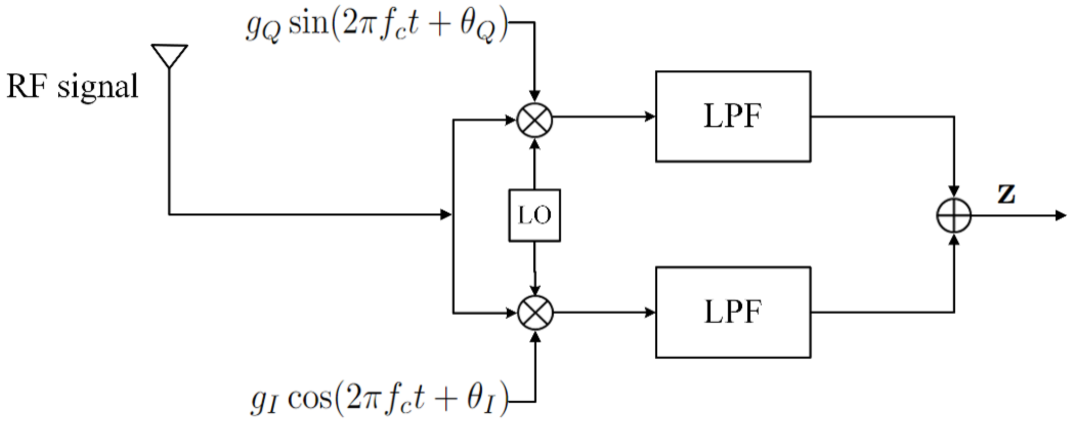

Figure 2.1: Illustration of non-ideal receiver with I/Q imbalance.

mance. Commonly observed in direct-conversion transceivers, I/Q imbalance poses significant challenges in wireless communication systems, including 4G LTE, 5G NR, Wi-Fi, and radar systems. To address this, various compensation techniques, such as calibration, adaptive algorithms, and digital pre-distortion, are employed to mitigate its effects and ensure reliable communication. Understanding and correcting I/Q imbalance is essential for maintaining the efficiency and accuracy of high-performance communication systems.

2.4.1 Principle of I/Q Imbalance

Nowadays, wireless communication systems always suffer from distortion and attenuation in the RF analog front end, which is a trade-off for compressing the complexity cost and improving energy efficiency [98]. For instance, direct-conversion architecture, also known as zero intermediate frequency (zero-IF) architecture, is illustrated in Figure 2.1. It is an approach for RF transceivers where the incoming RF signals are directly converted to baseband in the mixing process. This eliminates the need for intermediate frequency stages used in traditional superheterodyne receivers. However, the signals at the I and Q branches of the local oscillator cannot be equal in amplitude and perfectly quadratic. As shown in Figure 2.2, the image band signals remain and interfere with the original signals on the receiver side, thus degrading the system performance [99]. There is currently limited work on how to address the IQI problem in FTN systems, which is one of the primary focuses of this thesis.

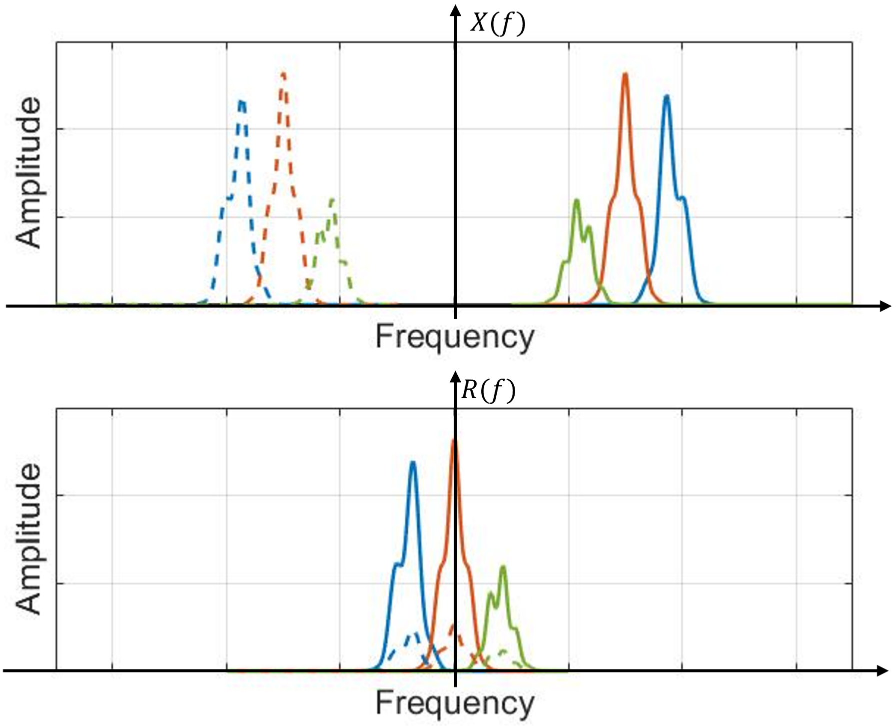

Figure 2.2: Spectrum of RF signal (top) and I/Q mismatched signal (bottom).

2.4.2 Existing IQI Cancellation Methods

Digital signal processing (DSP) techniques have shown promising capability for wide-band IQI mitigation, as demonstrated in various studies [100]–[102]. In [103], a pilot-assisted technique is used to estimate IQI parameters and phase noise within a single OFDM symbol. However, in extreme IQI conditions, residual degradation remains if the phase noise model significantly deviates from the ideal. To address similar challenges, [104] introduces a novel self-interference coordination method aimed at improving the performance of single-antenna, multi-carrier systems suffering from IQI. This method attains second-order frequency diversity without additional power cost. Nevertheless, the encoding scheme requires two consecutive time intervals for each data block to capture image band signals, resulting in a reduction in transmission rate. On the other hand, [105] explores the effectiveness of an iterative decision feedback receiver under the SC-FDE modulation scheme. This approach is robust to imperfect CSI through training sequences, but it requires high computational complexity when applied to multi-carrier transmission or fast-fading scenarios.

2.4.3 IQI Cancellation in FTN Systems

Due to the image band effect, conventional interference cancellation methods become less effective when considering IQI in FTN systems. For instance, the previously mentioned THP fails in an I/Q imbalanced system because it operates by generating an effective data sequence using a modulo operation to pre-cancel predicted interference before pulse shaping. However, this approach does not simultaneously process image signals, making it unsuitable for mitigating IQI. Additionally, THP introduces a modulo loss in performance, which is typically compensated by employing soft-input-soft-output (SISO) or powerful channel coding schemes. While these enhancements improve performance, they also significantly increase system complexity, making THP less practical for FTN systems with IQI.

Additionally, the most existing signal models that account for IQI are formulated in an FD bin-to-bin structure [106], [107], which is complex for simultaneous operation. These FD-based models process each frequency bin separately and fail to capture the correlation between original and image signals effectively, leading to suboptimal performance in IQI compensation. In contrast, the work in [108] takes a different approach by analyzing the behavior of an analog least mean square (ALMS) loop. Instead of treating the original and image signals independently, it integrates both into a unified matrix representation. This joint formulation allows for a more comprehensive understanding of the IQI effect and enables more effective compensation techniques. By leveraging this matrix-based approach, [108] provides deeper insights into the interaction between IQI and ISI cancellation algorithms, making it more suitable for applications requiring precise IQI mitigation, such as FTN systems with strong interference.

Notably, while this thesis primarily addresses IQI, other hardware impairments also significantly impact the performance of FTN systems. For instance, phase noise caused by imperfections in local oscillators leads to random phase fluctuations that degrade signal coherence and can deteriorate ISI in densely packed FTN transmissions [109]. Time and frequency offsets (TFO), often arising from synchronisation mismatches between transmitter and receiver, introduce further distortion, particularly in short-packet or high-mobility scenarios [94]. In particular, CFO, induced by oscillator mismatches and Doppler shifts, introduces time-varying phase rotation across symbols and results in FD interference, which is particularly detrimental in FTN systems due to their intentional TD overlap [110]. These impairments, when combined with FTN-induced ISI, pose significant challenges to system robustness and demand advanced compensation strategies. Future extensions of this work will aim to jointly address IQI, CFO, and phase noise within a unified signal model, thereby further improving the practicality of FTN implementation in real-world RF systems.

Chapter 3

Proposed FTN System and ISI Cancellation Algorithm

To address the problem discussed in previous chapters, this chapter formulates a unified baseband model for FTN signalling, beginning with signal generation and pulse shaping, and extending to multipath channel propagation. Furthermore, the proposed DDSIC algorithm relies on the system model performs frame-based detection by combining FD-MMSE equalisation with iterative symbol regeneration and interference removal. The simplified linear structure of DDSIC enables low-complexity implementation. This model enables realistic performance evaluation and directly supports the design and justification of the proposed frame-based algorithms introduced in subsequent chapters.

3.1 System and Signal Model

In this section, the basic FTN system and signal models of this thesis are presented.

As illustrated in Figure 3.1, binary bits are first generated and modulated into constellation points by an M-QAM mapper. Next, these M-QAM symbols are divided into frames and transmitted. In order to avoid inter-frame interference, a CP is added in the head of each data frame. Note that these symbols are transmitted at an accelerated interval of αT, where α represents the time acceleration factor, $0 < \alpha < 1$ and T represents the symbol interval for

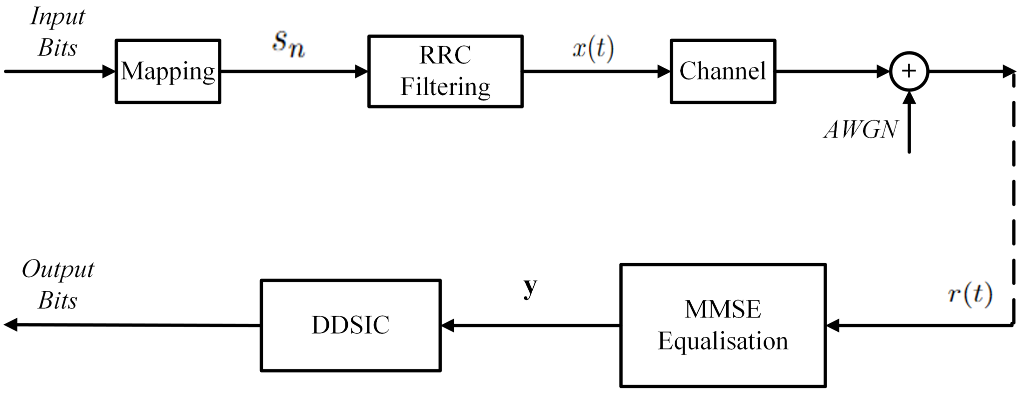

Figure 3.1: Block diagram of the proposed FTN system with DDSIC

Nyquist transmission. Next, a root-raised-cosine (RRC) filter, which is characterised by a 3 dB cut-off bandwidth of $1/T$ and a roll-off factor of β, is employed to shape the signal pulse and limit the signal bandwidth to the Nyquist bandwidth, i.e., $1/T$. After the RRC pulse shaping, ISI is inevitably introduced. The FTN accelerated signal $x(t)$ after the RRC filter is expressed as

$$x(t) = \sum_{n=0}^{N-1} s_n u(t - n\alpha T), \tag{3.1}$$

where s_n represents the n-th data symbol with an average power of σ_s^2, $n = 0, 1, 2, ..., N-1$, N is the number of symbols in each frame, $u(t)$ represents the RRC pulse with unit energy. Note that the pulse shaping process reduces the bandwidth, which consequently decreases the power of $x(t)$. The length of the CP is chosen to be longer than the overall channel impulse response (including the RRC filter).

Then, the symbols are passed through a wireless channel $h(t)$ and added by an AWGN. After CP-removal and sampled at an interval of αT, the received signal can be expressed as

$$r(t) = \sum_{n=0}^{N-1} s_n g(t - n\alpha T) + w(t), \tag{3.2}$$

where $g(t) = \int_{-\infty}^{\infty} h(\tau)u(t-\tau)d\tau$, and $w(t)$ is the zero mean AWGN with a variance of σ_w^2. Furthermore, denoting the discrete-time version of the data signal vector as $\mathbf{s} = [s_0, s_1, ..., s_{N-1}]^\mathbf{T}$ and the AWGN noise vector as $\mathbf{w}$, the discrete-time form of the received signal vector can be expressed as

$$\begin{aligned}\mathbf{r} &= [r_0, r_1, ..., r_{N-1}]^{\mathbf{T}} \\ &= \mathbf{Gs} + \mathbf{w},\end{aligned} \tag{3.3}$$

where **G** is the equivalent channel matrix. For an AWGN channel, **G** can be expressed as a circular convolution matrix of order $N \times N$, given by

$$\mathbf{G} = \begin{pmatrix} g(0) & g(\alpha T) & \cdots & g((N-1)\alpha T) \\ g((N-1)\alpha T) & g(0) & \cdots & g((N-2)\alpha T) \\ \vdots & \vdots & \ddots & \vdots \\ g(\alpha T) & g(2\alpha T) & \cdots & g(0) \end{pmatrix}. \tag{3.4}$$

Note that although the elements of **G** are sampled in an interval of αT, the bandwidth of **G** is $1/T$, which is consistent with the Nyquist bandwidth.

At the receiver side, the frame-based DDSIC will be processed to recover the data bits. To efficiently mitigate ISI in practical FTN systems, a low complexity frame-based DDSIC algorithm is proposed. As illustrated in Figure. 3.2, the DDSIC algorithm is divided into two stages: the FD-MMSE equalisation as the first stage and the iterative ISI cancellation as the second stage. To assess the effectiveness of the proposed algorithm, theoretical BER expressions for each iteration and a BER lower bound for M-QAM FTN systems are derived. Finally, simulation results are provided to validate the accuracy of the derived expressions and to evaluate the performance of the proposed scheme under practical channel conditions.

3.2 Frequency Domain MMSE Equalisation

The FD-MMSE equalisation is employed to perform the initial interference cancellation and defined as the first iteration of DDSIC. The principle of MMSE equalisation is to minimise the output MSE, thereby reducing ISI. The MMSE equalisation matrix is defined as

$$\mathbf{E} = \mathbf{G}^{\mathbf{H}}(\mathbf{G}\mathbf{G}^{\mathbf{H}} + \frac{1}{\gamma_{in}}\mathbf{I}_N)^{-1}, \tag{3.5}$$

where γ_{in} represents the input SNR of the MMSE equaliser and $\mathbf{I}_N$ represents the identity matrix of order N.

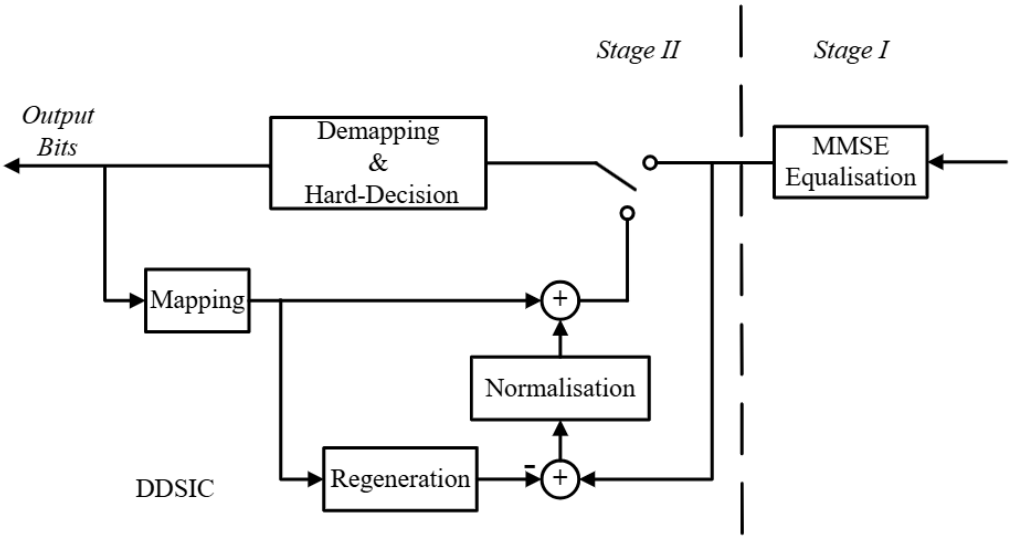

Figure 3.2: Block diagram of the proposed DDSIC receiver, including FD-MMSE equalisation and iterative symbol detection.

As discussed in Section 1.3, MMSE equalisation outperforms finite-length ZF equalisation, especially at low SNRs, as ZF equalisation tends to amplify noise. Moreover, the zero samples at the edges of the FTN signal bandwidth result in infinity values due to matrix inversion, leading to severe degradation in ZF equalisation performance [111]. In contrast, MMSE equalisation is less affected by this issue, as it accounts for the input SNR, thereby providing greater robustness under these conditions. Compared with the matched filtering as in most existing systems [54], MMSE equalisation produces a shorter response for a data symbol and thus performs better in ISI mitigation.

The MMSE equalised signal can be expressed as

$$\begin{aligned} \mathbf{y} &= \mathbf{E}\mathbf{r} \\ &= \mathbf{P}\mathbf{s} + \mathbf{E}\mathbf{w}, \end{aligned} \tag{3.6}$$

where $\mathbf{P} = \mathbf{G^H}(\mathbf{G}\mathbf{G^H} + \frac{1}{\gamma_{in}}\mathbf{I}_N)^{-1}\mathbf{G}$ is the equivalent transfer matrix from $\mathbf{s}$ to $\mathbf{y}$. Note that $\mathbf{P}$ is an $N \times N$ circular Toeplitz matrix with the first row as $[p_0, p_1, ..., p_{N-1}]$, and can be further processed with eigenvalue decomposition to analyse the performance.

The direct implementation of MMSE equalisation in TD is computationally intensive due to the involved matrix inversion and circular convolution operations. To solve this issue, the proposed system adopts a frame-based FD equalisation approach. This method is favored for its substantially reduced computational complexity compared to TD techniques, leveraging the FFT to replace linear convolution operations with efficient element-wise multiplications in FD [112]. Additionally, in the proposed FD approach, the length of TD ISI, which is an important factor in conventional FTN signalling models, becomes less significant. This is because multi-tap channels are represented by a single-tap weight for each subcarrier. Specifically, assuming that the CSI is perfectly known on the receiver side, let $G[k]$ denote the DFT of $g(n\alpha T)$ in Eq. (3.4), where $k = 0, 1, ..., N-1$ and $n = 0, 1, ..., N-1$, the elements of FD-MMSE equalisation can be derived from Eq. (3.5) as

$$E[k] = \frac{G^*[k]}{|G[k]|^2 + \frac{1}{\gamma_{in}}}. \tag{3.7}$$

Furthermore, the output signal in FD form is simply given by the inverse discrete Fourier transform (IDFT) of $E[k]R[k]$, where $R[k]$ denotes the DFT of $r(n\alpha T)$.

The frequency responses of RRC-shaped pulses with various pairs of $[\alpha, \beta]$ are illustrated in Figure 3.3. The bandwidth occupied by the RRC pulse signal is given by $B = (1+\beta)/T$, while the bandwidth of the FTN signal (before RRC filtering) is $1/(\alpha T)$. Consequently, when an RRC filter with $\beta > 1/\alpha - 1$ is used, part of the transmitted data information may be lost due to filtering. Conversely, if $\beta < 1/\alpha - 1$, as illustrated in the lower subfigure, there will be zero samples at the edges of the frequency band carrying no data but only noise. These null samples result in zeros for $G[k]$, which can lead to distortion during data recovery. In this chapter, it is chosen that $\beta \leqslant 1/\alpha - 1$ to ensure all data information is preserved while accepting some level of distortion from zero samples.

Compared with the conventional SC-FDE approach in [113], FTN signalling operates at a higher transmission rate, while signals in the SC-FDE method are transmitted at the Nyquist rate. Consequently, additional interference cancellation is not necessary in a Nyquist SC-FDE scheme. In contrast, the proposed technique employs MMSE equalisation to generate an initial estimate of the data bits following demapping and hard decision processes. This estimation acts as the first iteration of the interference cancellation process known as DDSIC, which will be elaborated in Section 3.3. Following demapping, the DDSIC algorithm iteratively eliminates ISI until performance stabilises. Both MMSE equalisation and DDSIC are executed frame-

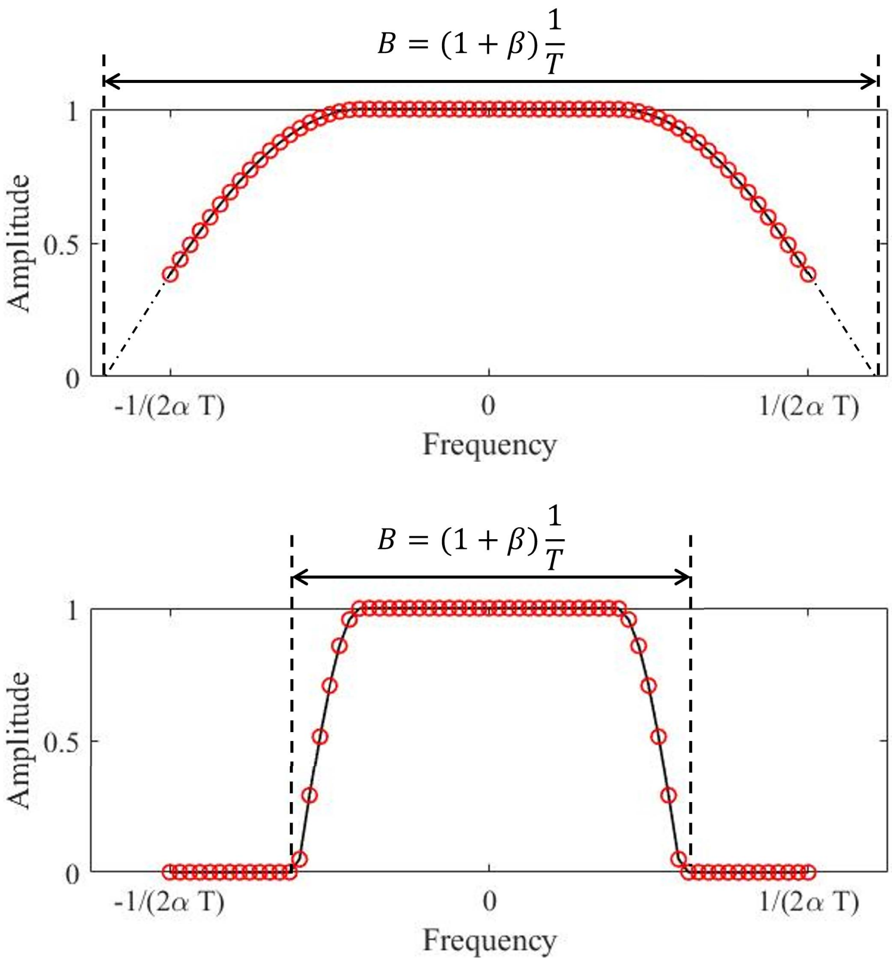

Figure 3.3: Frequency responses of RRC filter with various pairs of $[\alpha, \beta]$ (markers in red indicate the FD samples).

by-frame within the frequency domain, significantly lowering complexity compared to other symbol-by-symbol techniques.

3.3 Decision-Directed Successive Interference Cancellation

Following MMSE equalisation, the successive interference cancellation performs as the second stage. After the second iteration, it is assumed that most of the ISI is eliminated, resulting in a near-accurate data recovery. To further approach an ISI-free outcome, the DDSIC process can be repeated for multiple iterations, progressively refining the estimated symbols and achieving a highly accurate result.

The equalised signal is first decomposed in Eq. (3.6) into three components as

$$\begin{aligned} \mathbf{y} &= \mathbf{P}\mathbf{s} + \mathbf{E}\mathbf{w} \\ &= p_0\mathbf{s} + (\mathbf{P} - p_0\mathbf{I}_N)\mathbf{s} + \mathbf{E}\mathbf{w}, \end{aligned} \tag{3.8}$$

where the first term on the right side of Eq. (3.8) indicates the desired data signal, the second term represents ISI and the third term represents the noise component. For instance, considering one single input symbol s_0, the output from the noise-free MMSE equaliser can be expressed as $y_0 = p_0 s_0 + p_1 s_1 + ... + p_{N-1} s_{N-1}$. In this formulation, the term $p_0 s_0$ represents the desired signal, while all remaining terms constitute ISI arising from other symbols within the same frame. Obviously, the coefficient p_0 is critical for accurately scaling and recovering the desired signal.

Building on this decomposed signal model, an interference cancellation algorithm is applied after the FD-MMSE equalisation. In the subsequent iterations, the objective is to remove ISI from the MMSE-equalised signal using data symbols determined in prior steps. Letting $\mathbf{y}^i$ represent the equalised received signal at the i-th iteration, the hard-decided data symbols can be expressed as

$$\hat{\mathbf{s}}^i = \text{Dec}\left\{\mathbf{y}^i\right\}, \tag{3.9}$$

where Dec$\{\cdot\}$ represents the hard-decision operation. Following this, the signal is regenerated by passing the decided symbols $\hat{\mathbf{s}}^i$ through the same RRC filter, channel response (excluding noise), and MMSE equaliser, whose combined response is represented by $\mathbf{P}$ as outlined beneath Eq. (3.6), i.e., $\hat{\mathbf{y}}^i = \mathbf{P}\hat{\mathbf{s}}^i$. It is important to note that this process involves circular convolution, which can be executed directly in TD or alternatively in FD using DFT/IDFT techniques as discussed earlier.

After regeneration, the amplitude of the desired signal has already been attenuated following MMSE equalisation. Therefore, it is necessary to normalise both the equalised and regenerated signals by p_0 before making decisions in the next iteration. After normalisation by p_0, and with the decided symbols added back in, an equalised and ISI-mitigated signal is obtained as

$$\mathbf{y}^{i+1} = \hat{\mathbf{s}}^i + (\mathbf{y} - \hat{\mathbf{y}}^i)/p_0, \tag{3.10}$$

which can then be used in the subsequent iteration decision process.

Through iterative application of the interference cancellation process, the estimated symbol progressively converges towards being ISI-free. After sufficient iterations, the algorithm achieves a highly accurate symbol estimate, effectively mitigating residual interference.

It is important to note that despite this section focusing on hard decisions, soft-decision can also be incorporated within DDSIC. By employing a soft-output demodulator in conjunction with a soft-decision decoder, likelihood probabilities can be calculated and leveraged in subsequent iterations. Although a detailed design of this approach falls outside the scope of this thesis, simulation results will be provided for scenarios in which soft outputs from the final iteration are used as inputs to a decoder.

3.4 Comparison with Existing Symbol-based Methods

As discussed in Section 2.2, conventional ISI cancellation methods for FTN signalling, such as the SSSSE and its enhanced version, the SSSgbKSE presented in [54], mainly operate on a symbol-by-symbol basis, making them highly sensitive to the accuracy of initial symbol decision. The fundamental principle of SSSSE is to compute the ISI matrix after applying the matched filtering and subsequently remove ISI for each subsequent symbol, highly relying on the estimation of individual ISI components. The SSSgbKSE extends this framework by leveraging the previously estimated K symbols to refine the current symbol estimate, thereby improving the overall accuracy of symbol recovery.

However, a key limitation of both methods lies in their approach to estimating the first symbol. Both these two methods are carried out by simply selecting the nearest constellation point, disregarding the influence of ISI on this symbol. The accuracy of this initial estimation is critical, as any errors can propagate and significantly degrade the overall system performance. Furthermore, both methods only consider the interference from preceding symbols due to the nature of systems, whereas symbols can be significantly influenced by subsequent symbols after practical matched filtering. As a result, under severe FTN conditions with low values of α, and/or adopting higher-order modulation schemes, both SSSSE and SSSgbKSE exhibit suboptimal performance due to their limited capability in managing the complete ISI impact.

In contrast, the proposed frame-based DDSIC algorithm achieves higher robustness by jointly estimating all symbols within a single transmission frame rather than relying on the precision of any individual symbol decision. This collective approach significantly enhances the reliability of ISI cancellation and reduces the susceptibility to errors that arise from incorrect initial decisions. Compared with SSSSE and SSSgbKSE which perform convolutions in TD due to their symbol-by-symbol nature, the proposed DDSIC leverages FD processing, implementing equalisation and signal regeneration efficiently through FFT/IFFT operations. By addressing ISI simultaneously within an entire frame, the DDSIC algorithm substantially mitigates the challenges posed by severe FTN signalling conditions and higher-order modulation, providing a more effective solution for data recovery, which will be demonstrated in the following sections.

3.5 Computational Complexity Comparison

In this subsection, a comprehensive comparison of computational complexity is conducted between the proposed DDSIC algorithm and several existing methods, including SSSSE, SSSgbKSE, as well as the truncated VA in [56] and the M-BCJR algorithm incorporating CS technique in [57]. The specific comparison and analysis, including the number of numerical operations, the states per frame and the complexity order of traversing, are outlined in Table 3.1 on the next page. In this table, N represents the number of symbols per frame, L represents the element number of the truncated ISI channel, and K denotes the length of the go-back sequence for the SSSgbKSE approach. For the truncated VA and M-BCJR algorithms, m represents the constellation points, L_{ISI} represents the truncated ISI length, and M_S corresponds to the number of survivors in the M-BCJR algorithm.

The computational complexity of the DDSIC algorithm primarily arises from the following terms. Firstly, the TD transfer matrix $\mathbf{P}$ is established only once in stage I, which requires $2N^2$ additions/subtractions and $2N^2$ multiplications/divisions for FFT/IFFT to the channel matrix $\mathbf{G}$. In each iteration of stage II, the ISI cancellation for each frame, as defined in Eq. (3.10), involves $2N$ additions/subtractions and $2N$ multiplications/divisions. As indicated in

Table 3.1: Computational Complexity Comparison

Operations	**Addition/ Subtraction**	**Multiplication/ Division**	**Exponentiation/ Logarithm**	**States for Traversing per Frame**
DDSIC (Stage I)	$2N^2 + 2N$	$2N^2 + 2N$	0	
DDSIC (per iteration in Stage II)	$2N$	$2N$	0	
SSSSE in [54]	$N(L-2)$	$N(L-1)$	0	
SSSgbKSE in [54]	$N(K(L-2)$ $+K(K-1)/2)$	$N(K(L-1)$ $+K(K+1)/2)$	0	
Truncated VA in [56]	Nm	Nm	Nm	$m^{L_{ISI}-1} \cdot (L_{ISI}-1)$
M-BCJR with CS in [57]	$2(N + L_{ISI})$	$10(N + L_{ISI})$	$7(N + L_{ISI})$	NMm

Table 3.1, the complexity of the proposed DDSIC algorithm remains comparable to that of the SSSSE and the SSSgbKSE, due to its frame-based principle. Moreover, the entire frame is processed concurrently, eliminating the need for segmentation into N individual processes.

When compared to the truncated VA and M-BCJR algorithms, DDSIC demonstrates significantly reduced computational complexity, as it avoids both exponential operations and the need for traversing processes. Furthermore, under high-order modulation scenarios, such as 16-QAM and 64-QAM, the number of states in the truncated VA and M-BCJR algorithms is far beyond the practical implementation limitation. Conversely, the DDSIC algorithm maintains a low computational burden, rendering it a more feasible choice for practical implementation, particularly under challenging channel conditions and with higher modulation orders.

3.6 Performance Analysis

In this section, the mathematical forms of system performance, i.e., the BER expressions of each iteration of DDSIC are derived. Moreover, a BER lower bound where ISI is completely removed is derived.

3.6.1 Eigenvalue Decomposition

To analyse the BER of each iteration, some foundation expressions for the DDSIC algorithm are first derived.

As mentioned in Section 3.2, $\mathbf{G}$ is a circular convolution matrix, which can be further expanded with eigenvalue-based matrix decomposition as

$$\mathbf{G} = \mathbf{F^H}\text{diag}\left\{G[k]\right\}\mathbf{F}, \tag{3.11}$$

where $\mathbf{F}$ and $\mathbf{F^H}$ denotes the DFT and the IDFT matrix, respectively. $\mathbf{F}$ and $\mathbf{F^H}$ satisfy that $\mathbf{FF^H} = \mathbf{F^HF} = \mathbf{I}_N$. diag $\{G[k]\}$ represents a diagonal matrix with $G[k]$ being the k-th diagonal element. Note that the diagonal elements are the eigenvalues of matrix $\mathbf{G}$.

Furthermore, $\mathbf{P}$ can be decomposed as

$$\begin{aligned}\mathbf{P} &= \mathbf{G^H}(\mathbf{GG^H} + \frac{1}{\gamma_{in}}\mathbf{I}_N)^{-1}\mathbf{G} \\ &= \mathbf{F^H}\text{diag}\left\{G^*[k]\right\}\mathbf{F}(\mathbf{F^H}\text{diag}\left\{|G[k]|^2\right\}\mathbf{F} \\ &+ \frac{1}{\gamma_{in}}\mathbf{I}_N)^{-1}\mathbf{F^H}\text{diag}\left\{G[k]\right\}\mathbf{F} \\ &= \mathbf{F^H}\text{diag}\left\{\frac{\gamma_{in}|G[k]|^2}{\gamma_{in}|G[k]|^2+1}\right\}\mathbf{F}.\end{aligned} \tag{3.12}$$

Based on the principle of EVD, the normalisation factor p_0 can be expressed as

$$p_0 = \frac{1}{N}\text{Tr}\left\{\mathbf{P}\right\} = \frac{1}{N}\sum_{n=0}^{N-1}\frac{\gamma_{in}|G[k]|^2}{\gamma_{in}|G[k]|^2+1}, \tag{3.13}$$

where Tr$\{\cdot\}$ indicates the trace of a matrix.

From Eq. (3.8), the received signal is divided into three components, i.e., desired signal, ISI and noise. Therefore, the output SNR of the i-th iteration can be expressed as

$$\gamma_{out}^{i} = \frac{\text{Power}\left\{\text{desired signal}\right\}}{\text{Power}\left\{\text{residual ISI}\right\} + \text{Power}\left\{\text{noise}\right\}}. \tag{3.14}$$

As a foundation of signal power computation, the decomposed covariance matrix of the transfer matrix $\mathbf{P}$ is first derived as

$$\begin{aligned}\mathbf{P}\mathbf{P}^{\mathbf{H}} &= \mathbf{F}^{\mathbf{H}}\mathbf{\Psi}\mathbf{F}\mathbf{F}^{\mathbf{H}}\mathbf{\Psi}^{\mathbf{H}}\mathbf{F} \\ &= \mathbf{F}^{\mathbf{H}}\mathbf{\Psi}\mathbf{\Psi}^{\mathbf{H}}\mathbf{F} \\ &= \mathbf{F}^{\mathbf{H}}\mathrm{diag}\left\{(\frac{\gamma_{in}|G[k]|^2}{\gamma_{in}|G[k]|^2+1})^2\right\}\mathbf{F},\end{aligned} \tag{3.15}$$

where $\mathbf{\Psi} = \mathrm{diag}\left\{\frac{\gamma_{in}|G[k]|^2}{\gamma_{in}|G[k]|^2+1}\right\}$ is a diagonal matrix. The elements on the diagonal of $\mathbf{\Psi}$ are eigenvalues of $\mathbf{P}$.

From Eqs. (3.5) and (3.6), the covariance matrix of $\mathbf{y}$ is derived as

$$\begin{aligned}\mathbb{E}[\mathbf{y}\mathbf{y}^{\mathbf{H}}] &= \mathbb{E}[(\mathbf{P}\mathbf{s}+\mathbf{E}\mathbf{w})(\mathbf{P}\mathbf{s}+\mathbf{E}\mathbf{w})^{\mathbf{H}}] \\ &= \mathbf{P}\mathbb{E}[\mathbf{s}\mathbf{s}^{\mathbf{H}}]\mathbf{P}^{\mathbf{H}} + \mathbf{E}\mathbb{E}[\mathbf{w}\mathbf{w}^{\mathbf{H}}]\mathbf{E}^{\mathbf{H}} \\ &= \sigma_s^2\mathbf{P}\mathbf{P}^{\mathbf{H}} + \sigma_w^2\mathbf{E}\mathbf{E}^{\mathbf{H}} \\ &= \sigma_s^2(\mathbf{P}\mathbf{P}^{\mathbf{H}} + \frac{1}{\gamma_{in}}\mathbf{E}\mathbf{E}^{\mathbf{H}}) \\ &= \sigma_s^2(\mathbf{E}\mathbf{G}\mathbf{G}^{\mathbf{H}}\mathbf{E}^{\mathbf{H}} + \frac{1}{\gamma_{in}}\mathbf{E}\mathbf{E}^{\mathbf{H}}) \\ &= \sigma_s^2\mathbf{E}(\mathbf{G}\mathbf{G}^{\mathbf{H}} + \frac{1}{\gamma_{in}}\mathbf{I}_{\mathbf{N}})\mathbf{E}^{\mathbf{H}} \\ &= \sigma_s^2\mathbf{E}\mathbf{E}^{\mathbf{-1}}(\mathbf{E}\mathbf{G})^{\mathbf{H}} \\ &= \sigma_s^2\mathbf{P}^{\mathbf{H}}.\end{aligned} \tag{3.16}$$

3.6.2 Theoretical BER of Stage I

In the first stage of DDSIC, only MMSE equalisation is applied, and the output SNR can be derived as

$$\begin{aligned}\gamma_{out}^{(1)} &= \frac{\frac{1}{N}\mathrm{Tr}\left\{\mathbb{E}[p_0\mathbf{s}(p_0\mathbf{s})^{\mathbf{H}}]\right\}}{\frac{1}{N}\mathrm{Tr}\left\{\mathbb{E}[\mathbf{y}\mathbf{y}^{\mathbf{H}}]\right\} - \frac{1}{N}\mathrm{Tr}\left\{\mathbb{E}[p_0\mathbf{s}(p_0\mathbf{s})^{\mathbf{H}}]\right\}} \\ &= \frac{\sigma_s^2|p_0|^2}{\frac{1}{N}\mathrm{Tr}\left\{\sigma_s^2\mathbf{P}^{\mathbf{H}}\right\} - \sigma_s^2|p_0|^2} \\ &= \frac{|p_0|^2}{p_0^* - |p_0|^2} \\ &= \frac{p_0}{1-p_0} \\ &= \frac{\sum_{k=0}^{N-1}\frac{\gamma_{in}|G[k]|^2}{\gamma_{in}|G[k]|^2+1}}{\sum_{k=0}^{N-1}\frac{1}{\gamma_{in}|G[k]|^2+1}}.\end{aligned} \tag{3.17}$$

Denoting $P_s^{(1)}$ as the symbol error probability for the first iteration of DDSIC, the relationship between $P_s^{(1)}$ and $\gamma_{out}^{(1)}$ for an M-QAM system can be formulated as

$$P_s^{(1)} \approx 1 - \left\{ 1 - 2(1 - \frac{1}{\sqrt{M}})Q\left(\sqrt{\frac{3\gamma_{out}^{(1)}}{M-1}}\right) \right\}^2, \tag{3.18}$$

where the Q-function is defined as $Q(x) = \frac{1}{\sqrt{2\pi}}\int_x^{\infty} e^{-\frac{t^2}{2}}dt$.

Denoting $P_b^{(1)}$ as the bit error probability, the BER of the first iteration for an M-QAM system is derived as

$$\begin{aligned} P_b^{(1)} &\approx \frac{1}{\log_2 M} P_s^{(1)} \\ &\approx \frac{1}{\log_2 M}\left\{ 1 - \left[1 - 2(1 - \frac{1}{\sqrt{M}})Q\left(\sqrt{\frac{3\gamma_{out}^{(1)}}{M-1}}\right)\right]^2 \right\} \\ &= \frac{1}{\log_2 M}\left\{ 1 - \left[1 - 2(1 - \frac{1}{\sqrt{M}}) \right.\right. \\ &\qquad \left.\left. Q\left(\sqrt{\frac{3}{M-1}\frac{\sum_{k=0}^{N-1}\frac{\gamma_{in}|G[k]|^2}{\gamma_{in}|G[k]|^2+1}}{\sum_{k=0}^{N-1}\frac{1}{\gamma_{in}|G[k]|^2+1}}}\right)\right]^2 \right\}. \end{aligned} \tag{3.19}$$

3.6.3 Theoretical BER of Stage II

In the direct decision process, the symbols are demapped to their nearest constellation points. These constellation points are systematically organised according to Gray code, which ensures that each neighboring point differs by only a single bit. Assuming a low symbol error rate, where only one bit is likely to be in error for each incorrect decision, the erroneously chosen constellation point will invariably be one of its adjacent neighbors. As a result, the Euclidean distance between an incorrectly selected point and the correct point can be expressed as $2d$, where d is the scaling factor for the spacing between constellation points. Under normalisation to unit power, this distance is given by $d = \frac{1}{\sqrt{\frac{2}{3}(M-1)}}$ for M-QAM system.

Figure 3.4 provides illustrative examples of the demapping process for a 16-QAM system. Observe that after the ISI cancellation, any wrongly decided symbol will effectively double the interference introduced into the subsequent signal estimation. As a result, the residual ISI power becomes $(4d)^2$ times the original ISI power, scaled by the symbol error rate. Consequently, the

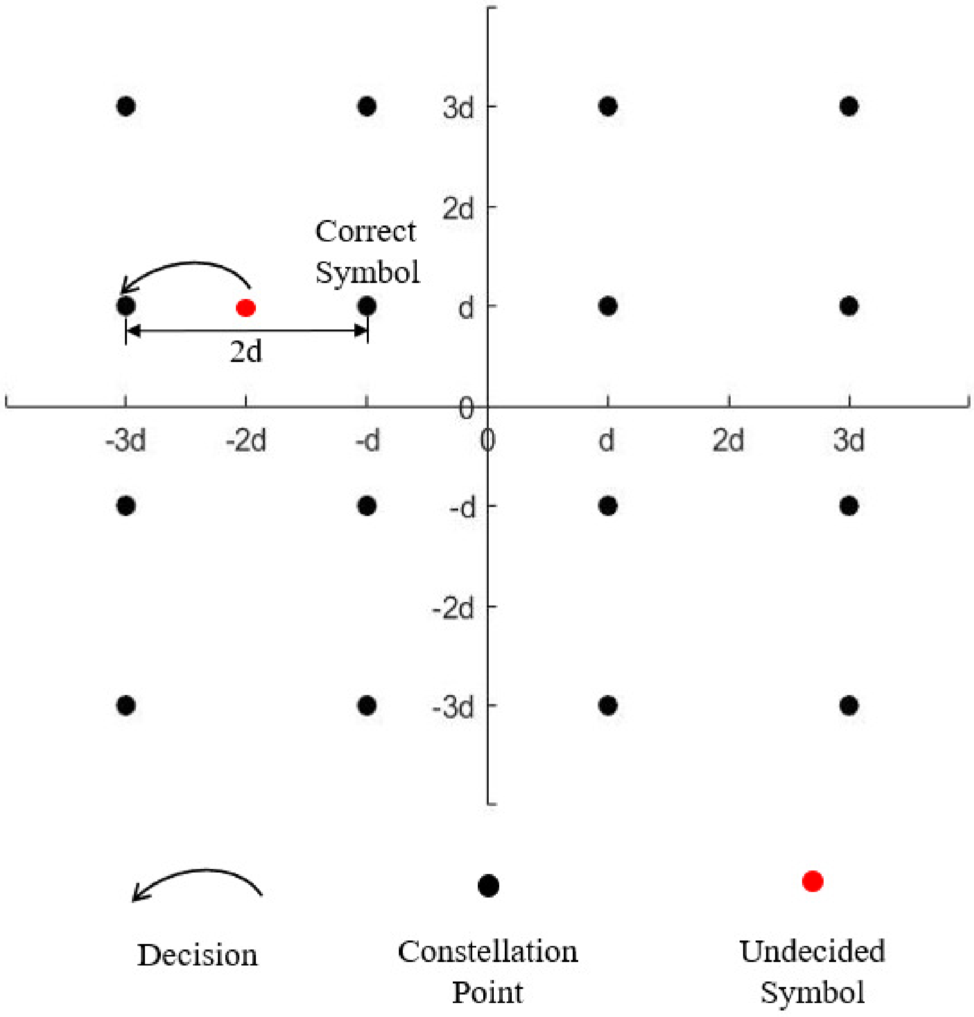

Figure 3.4: Illustration of decision errors for 16-QAM symbols.

residual ISI power after the first iteration can be derived as

$$\begin{aligned}\mathrm{ISI}_{re}^{(1)} &= (\frac{4}{\sqrt{\frac{2}{3}(M-1)}})^2 \frac{1}{N}\mathrm{Tr}\left\{(\mathbf{P}-p_0\mathbf{I}_N)(\mathbf{P}-p_0\mathbf{I}_N)^{\mathbf{H}}\right\} P_s^{(1)} \\ &= \frac{24}{M-1}\frac{1}{N}\mathrm{Tr}\left\{(\mathbf{P}-p_0\mathbf{I}_N)(\mathbf{P}-p_0\mathbf{I}_N)^{\mathbf{H}}\right\} P_s^{(1)} \\ &= \frac{24}{M-1}\frac{1}{N}(\mathrm{Tr}\left\{\mathbf{PP^H}\right\} - {p_0}^2)P_s^{(1)} \\ &= \frac{24}{M-1}\frac{1}{N}[\sum_{k=0}^{N-1}(\frac{\gamma_{in}|G[k]|^2}{\gamma_{in}|G[k]|^2+1})^2 - \\ &\quad (\sum_{k=0}^{N-1}\frac{\gamma_{in}|G[k]|^2}{\gamma_{in}|G[k]|^2+1})^2]P_s^{(1)}.\end{aligned} \tag{3.20}$$

Therefore, $\gamma_{out}^{(2)}$ can be expressed as

$$\begin{aligned}\gamma_{out}^{(2)} &= \frac{\frac{1}{N}\mathrm{Tr}\left\{\mathbb{E}[p_0\mathbf{s}(p_0\mathbf{s})^{\mathbf{H}}]\right\}}{\mathrm{ISI}_{re}^{(1)} + \frac{1}{N}\mathrm{Tr}\left\{\mathbb{E}[\mathbf{yy^H}]\right\} - \frac{1}{N}\mathrm{Tr}\left\{\mathbb{E}[\mathbf{Ps}(\mathbf{Ps})^{\mathbf{H}}]\right\}} \\ &= \frac{(\sum_{k=0}^{N-1}\frac{\gamma_{in}|G[k]|^2}{\gamma_{in}|G[k]|^2+1})^2}{\mathrm{ISI}_{re}^{(1)} + \sum_{k=0}^{N-1}\frac{\gamma_{in}|G[k]|^2}{(\gamma_{in}|G[k]|^2+1)^2}}.\end{aligned} \tag{3.21}$$

Then the BER of the second iteration for an M-QAM system can be derived as

$$\begin{aligned}P_b^{(2)} \approx \frac{1}{\log_2 M}\Bigg\{1 - \Bigg[1 - 2(1-\frac{1}{\sqrt{M}}) \\ Q\left(\sqrt{\frac{3}{M-1}\frac{(\sum_{k=0}^{N-1}\frac{\gamma_{in}|G[k]|^2}{\gamma_{in}|G[k]|^2+1})^2}{\mathrm{ISI}_{re}^{(1)} + \sum_{k=0}^{N-1}\frac{\gamma_{in}|G[k]|^2}{(\gamma_{in}|G[k]|^2+1)^2}}}\right)\Bigg]^2\Bigg\}.\end{aligned} \tag{3.22}$$

Without loss of generality, the BER expressions after the i-th iteration ($i > 1$) is derived as

$$P_b^{(i)} \approx \frac{1}{\log_2 M}\left\{1 - \left[1 - 2(1-\frac{1}{\sqrt{M}})Q\left(\sqrt{\frac{3\gamma_{out}^{(i)}}{M-1}}\right)\right]^2\right\} \tag{3.23}$$

where

$$\gamma_{out}^{(i)} = \frac{(\sum_{k=0}^{N-1}\frac{\gamma_{in}|G[k]|^2}{\gamma_{in}|G[k]|^2+1})^2}{\mathrm{ISI}_{re}^{(i-1)} + \sum_{k=0}^{N-1}\frac{\gamma_{in}|G[k]|^2}{(\gamma_{in}|G[k]|^2+1)^2}} \tag{3.24}$$

and

$$\begin{aligned}\mathrm{ISI}_{re}^{(i-1)} = (\frac{4}{\sqrt{\frac{2}{3}(M-1)}})^2\frac{1}{N}\mathrm{Tr}\{(\mathbf{P}-p_0\mathbf{I}_N) \\ (\mathbf{P}-p_0\mathbf{I}_N)^{\mathbf{H}}\}\log_2 M P_b^{(i-1)}.\end{aligned} \tag{3.25}$$

3.6.4 BER Lower Bound Derivation

To evaluate the best BER performance of the proposed algorithm, a BER lower bound is derived assuming all the ISI is removed, i.e., the interference all arises from the **Ew** component in Eq. (3.8). Denoted as γ_0, the output SNR without any ISI is expressed as

$$\begin{aligned}\gamma_0 &= \frac{\frac{1}{N}\mathrm{Tr}\left\{\mathbb{E}[p_0\mathbf{s}(p_0\mathbf{s})^{\mathbf{H}}]\right\}}{\frac{1}{N}\mathrm{Tr}\left\{\mathbb{E}[\mathbf{y}\mathbf{y}^{\mathbf{H}}]\right\}-\frac{1}{N}\mathrm{Tr}\left\{\mathbb{E}[\mathbf{Ps}(\mathbf{Ps})^{\mathbf{H}}]\right\}} \\ &= \frac{|p_0|^2}{p_0^*-\frac{1}{N}\mathrm{Tr}\left\{\mathbf{P}\mathbf{P}^{\mathbf{H}}\right\}} \\ &= \frac{1}{N}\frac{(\sum_{k=0}^{N-1}\frac{\gamma_{in}|G[k]|^2}{\gamma_{in}|G[k]|^2+1})^2}{\sum_{k=0}^{N-1}\frac{\gamma_{in}|G[k]|^2}{\gamma_{in}|G[k]|^2+1}-\sum_{k=0}^{N-1}(\frac{\gamma_{in}|G[k]|^2}{\gamma_{in}|G[k]|^2+1})^2} \\ &= \frac{1}{N}\frac{(\sum_{k=0}^{N-1}\frac{\gamma_{in}|G[k]|^2}{\gamma_{in}|G[k]|^2+1})^2}{\sum_{k=0}^{N-1}\frac{\gamma_{in}|G[k]|^2}{(\gamma_{in}|G[k]|^2+1)^2}}.\end{aligned} \tag{3.26}$$

Therefore, the BER lower bound for the M-QAM system is derived as

$$\begin{aligned}P_{bLB} &\approx \frac{1}{\log_2 M}\left\{1-\left[1-2(1-\frac{1}{\sqrt{M}})Q\left(\sqrt{\frac{3\gamma_0}{M-1}}\right)\right]^2\right\} \\ &= \frac{1}{\log_2 M}\left\{1-\left[1-2(1-\frac{1}{\sqrt{M}})\right.\right. \\ &\qquad \left.\left. Q\left(\sqrt{\frac{3}{M-1}\frac{1}{N}\frac{(\sum_{k=0}^{N-1}\frac{\gamma_{in}|G[k]|^2}{\gamma_{in}|G[k]|^2+1})^2}{\sum_{k=0}^{N-1}\frac{\gamma_{in}|G[k]|^2}{(\gamma_{in}|G[k]|^2+1)^2}}}\right)\right]^2\right\}.\end{aligned} \tag{3.27}$$

3.7 Simulation Results

In this section, the BER is regarded as the primary performance metric to assess the effectiveness of the proposed DDSIC algorithm.

Initially, the impulse and frequency responses of the MMSE equaliser and the conventional MF are analysed and compared. Additionally, the MMSE equalisation is replaced with match filtering as the first stage of DDSIC. In this case, the BER performances are compared to verify the superiority of the MMSE equaliser over the MF in mitigating interference.

Second, the BER performance of the proposed DDSIC algorithm is compared with the derived theoretical BERs across different modulation schemes and channel conditions. To assess the practicality of this approach, three types of channel are considered: AWGN channel, LOS and

Table 3.2: Simulation Parameters

Carrier Frequency (f_c)	6 GHz		Multipath Delay Spread	363 ns
No. of Frames	1500		Bandwidth (B)	7.68 MHz
No. of Symbols per Frame (N)	256		Duration of Frame (excluding CP) (N/B)	33.33 μs
Time Acceleration Factor (α)	0.8		Roll-off Factor of RRC Filter (β)	0.25

NLOS multipath fading channels. For the LOS and NLOS scenarios, two tapped delay line (TDL) channel models with multipath delays recommended by the European Telecommunications Standards Institute (ETSI) [114] are employed. The detailed parameters of TDL-A and TDL-D channel models are listed in Section 3.9 of this chapter. Additionally, the BER performance of the DDSIC algorithm with existing methods are compared, including the symbol-based SSSSE and SSSgbKSE in [54], the truncated VA in [56], and the M-BCJR algorithm with CS technique in [57]. The simulation parameters are detailed in Table 3.2, where the urban macrocell (UMa) channel under a normal-delay profile with a scenario-specific scaling factor of 363 ns as recommended in [114] is adopted. To achieve optimal transmission while avoiding both information loss and zero-sample distortion, the parameters $[\alpha, \beta]$ are set to maintain the relationship $\beta = 1/\alpha - 1$.

Finally, the potential for practical implementation is further demonstrated by evaluating the BER performance of the DDSIC algorithm combined with LDPC coding.

3.7.1 Comparison between MMSE Equaliser and Matched Filter

Figure 3.5 presents the impulse and frequency responses of the MMSE equaliser and the MF for a data symbol transmitted over an AWGN channel with equivalent noise bandwidth. The sampling period is denoted by αT, with $\beta = 0.25$ and an SNR of 20 dB. The corresponding

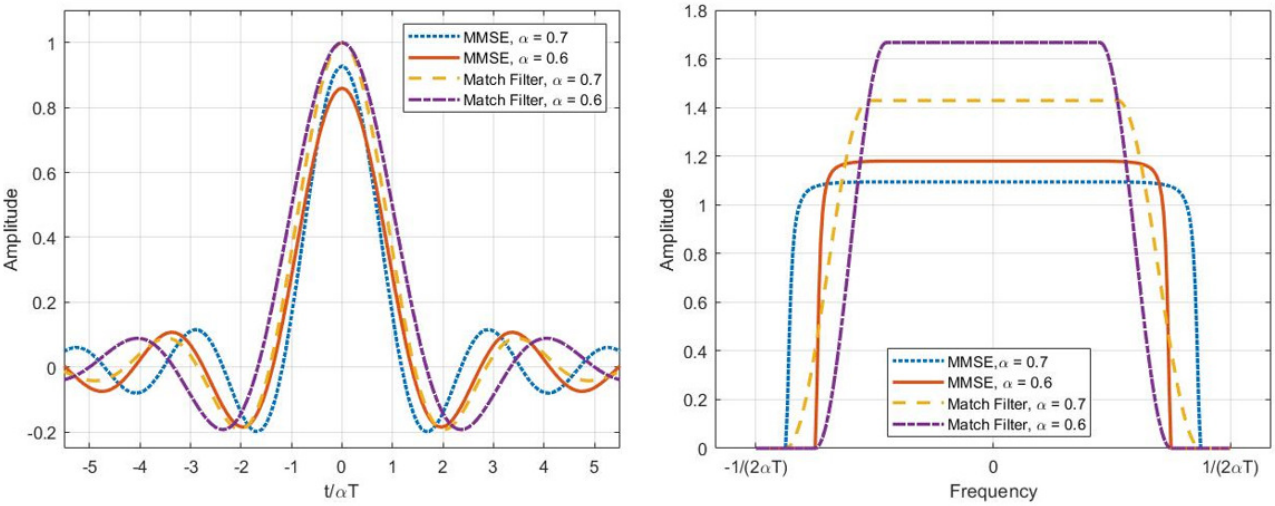

(a) (b)

Figure 3.5: Comparison of MMSE equaliser and MF under AWGN channel with $\beta = 0.25$ and SNR of 20 dB; (a) impulse response and (b) frequency response.

results for the TDL-D channel are illustrated in Figure 3.6. From Eq. (3.7), the amplitude at the center of the MMSE impulse response is always less than 1, whereas for the MF, it is consistently 1. It is also evident that with the same β, the MMSE equaliser's impulse response amplitude at $t = \pm\alpha T$ is lower than that of the MF. In other words, under identical noise conditions, MMSE equalisation results in reduced ISI compared to conventional matched filtering.

The BER performance comparisons between DDSIC employing MMSE equaliser and MF are presented in Figures 3.7 and 3.8. Observe that there is a notable performance enhancement of the MMSE equaliser over the MF after the first iteration without interference cancellation. While employed in DDSIC, MMSE equaliser consistently outperforms MF adopting both quadrature phase shift keying (QPSK) and 16-QAM modulations. For a target BER of 10^{-4}, a 0.5 dB performance gap is observed after the fifth iteration for QPSK modulation, whereas for 16-QAM modulation, the gap increases to 1.5 dB. Notably, performance after the third iteration of DDSIC with the MMSE equaliser is almost the same as that after the fifth iteration, indicating that four to five iterations are sufficient for effective interference cancellation. In contrast, when employing the MF, the BER continues to improve until the fifth iteration, illustrating that more iterations are required for adequate interference cancellation, i.e., more

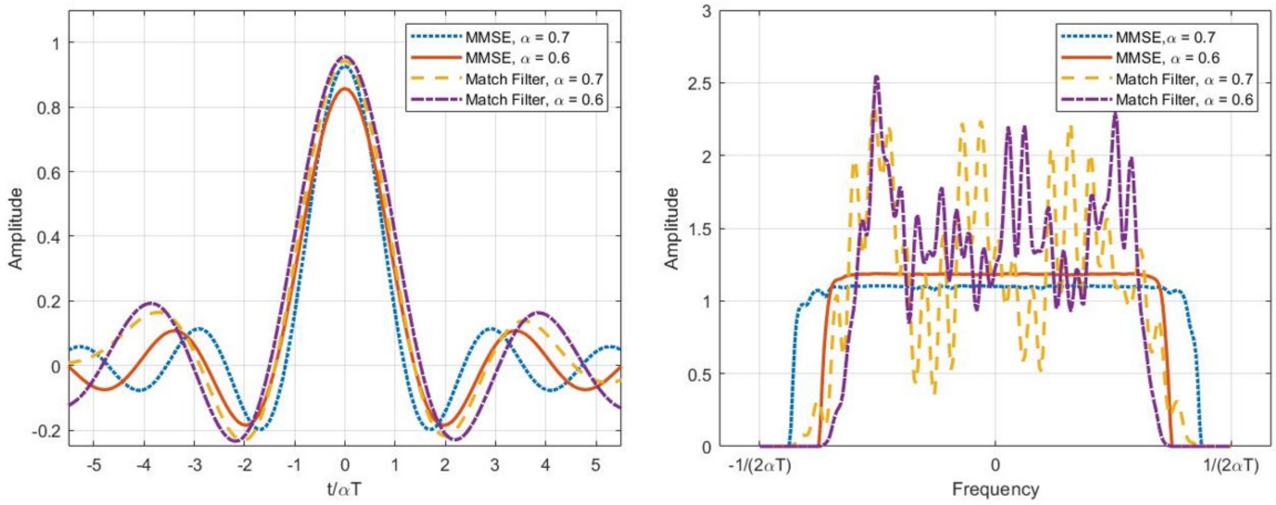

(a) (b)

Figure 3.6: Comparison of MMSE equaliser and MF under TDL-D channel with $\beta = 0.25$ and SNR of 20 dB; (a) impulse response (real parts only) and (b) frequency response.

complexity costs.

3.7.2 BER Performance Comparison

In this subsection, the BER performance of several algorithms under various settings is compared. For the SSSSE and SSSgbKSE methods, the ISI length L is set to 6 symbols, while the go-back sequence length K is set to 3 symbols. For the truncated VA and M-BCJR algorithms, the truncated ISI length L_{ISI} is set to 3, and the number of survivors M is set to 4.

The BER performance comparison for $\alpha = 0.8$, $\beta = 0.25$, and QPSK modulation in an AWGN channel is illustrated in Figure 3.9. The results show that the simulated BER curves for the DDSIC algorithm approach closely to the theoretical curves. In the first iteration, the proposed scheme outperforms SSSSE, while the performance after the second iteration surpasses that of SSSgbKSE and the truncated VA algorithm for SNR values greater than 10 dB.

In Figure 3.10, the BER performance comparison with $\alpha = 0.8$, $\beta = 0.25$, and 16-QAM modulation is presented. With 16-QAM modulation, the M-BCJR algorithm involves traversing 4096 states during each recursion to recover a single symbol, resulting in an unacceptable computational complexity for practical implementation. It is also observed that the SSSSE and SSSgbKSE algorithms fail under these conditions. Conversely, both DDSIC and truncated

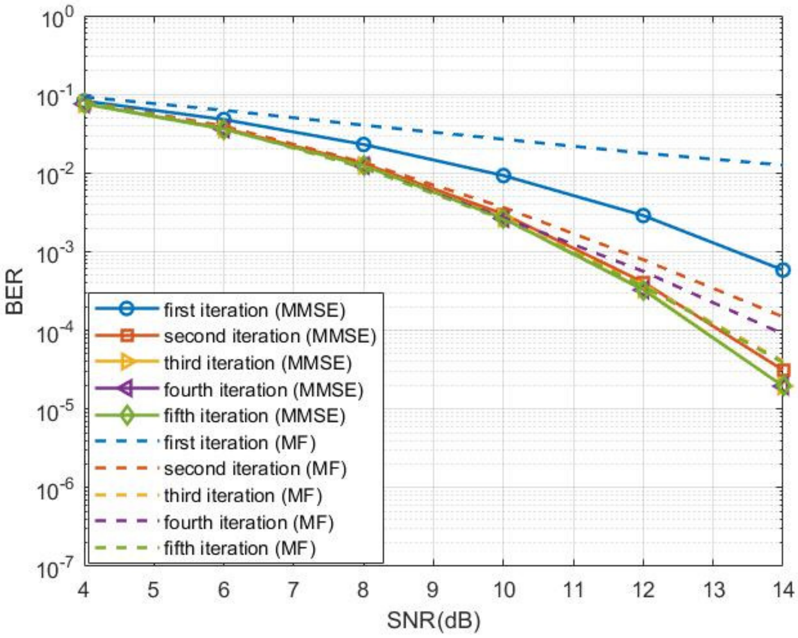

Figure 3.7: BER performance of DDSIC algorithm with MMSE equaliser and with MF under AWGN channel adopting QPSK modulation.

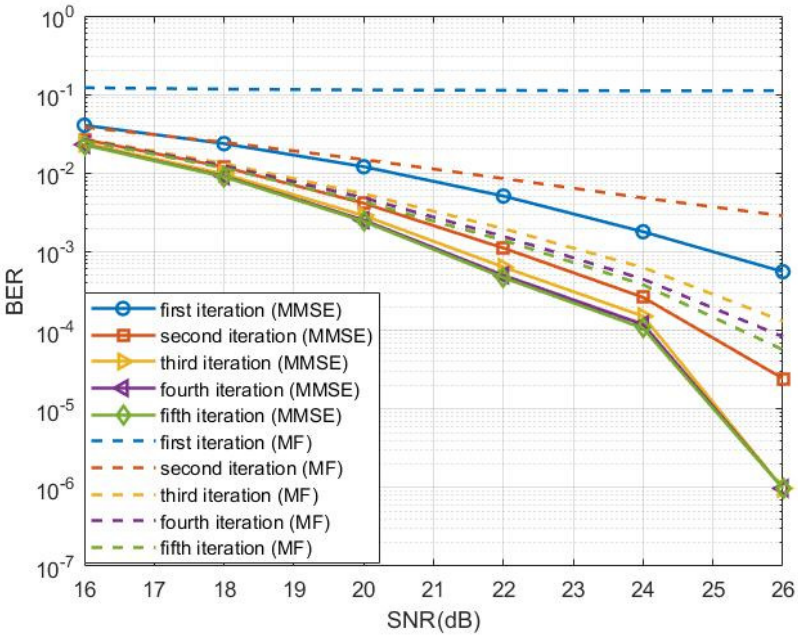

Figure 3.8: BER performance of DDSIC algorithm with MMSE equaliser and with MF under AWGN channel adopting 16-QAM modulation.

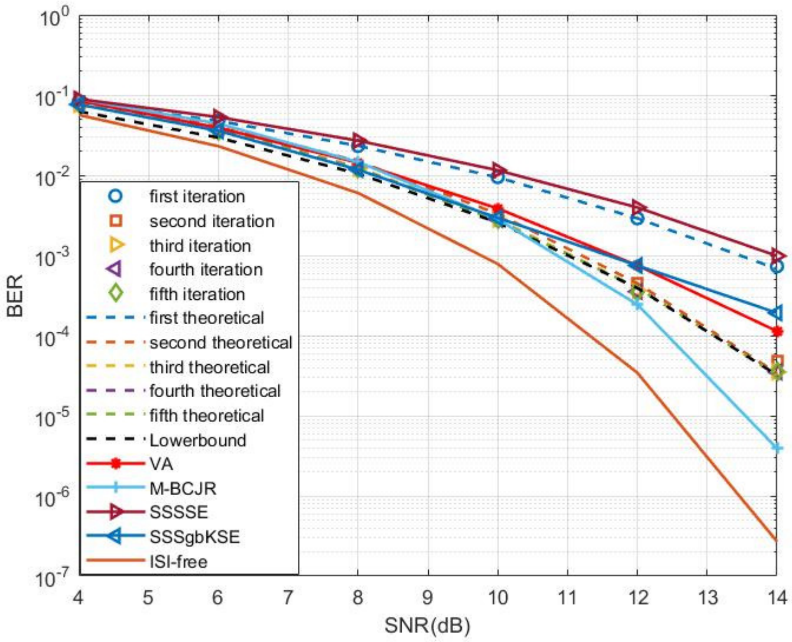

Figure 3.9: BER performance of various algorithms under AWGN channel with QPSK modulation.

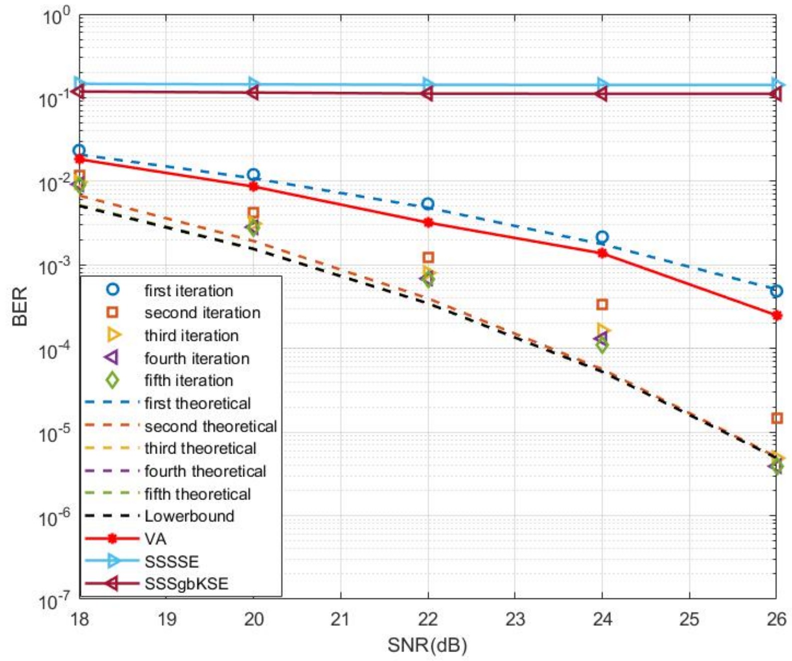

Figure 3.10: BER performance of various algorithms under AWGN channel with 16-QAM modulation.

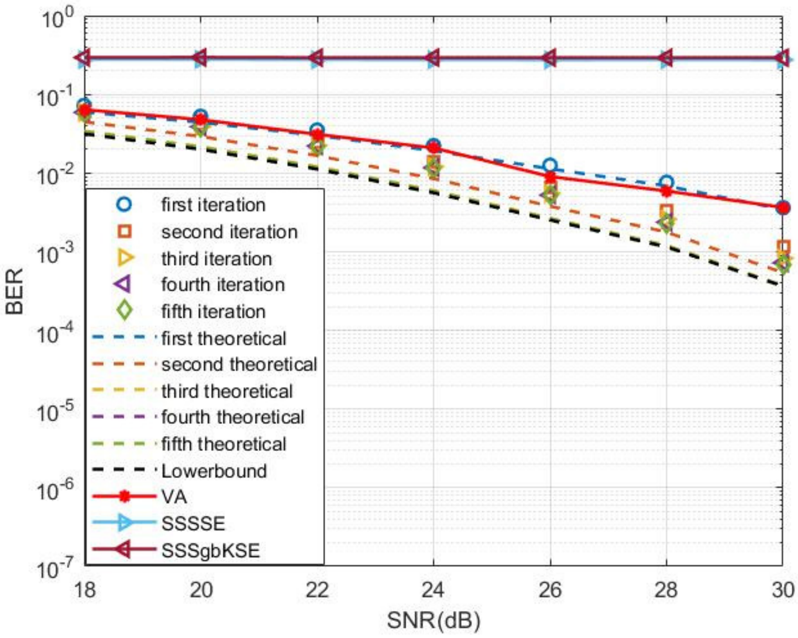

Figure 3.11: BER performance of various algorithms under TDL-A channel with 16-QAM modulation.

VA algorithms remain effective, with truncated VA only slightly outperforming DDSIC during the first iteration. Observe that a small offset exists between the theoretical and simulated BER values, mainly due to approximations in the residual ISI estimation. Similar to Figure 3.9, after the fourth iteration, the BER performance becomes nearly the same, suggesting that most of the ISI has been effectively mitigated by then.

The BER performance of the proposed DDSIC algorithm under realistic channel conditions is illustrated in Figures 3.11 and 3.12. It is worth noting that, in multipath fading channels, the instantaneous SNR varies across different realizations for a given average SNR. Consequently, the BER curves in these figures represent an ensemble average over multiple realizations, plotted against the average SNR. The results confirm that the proposed DDSIC algorithm remains highly effective even in multipath fading environments. Furthermore, the theoretically derived BER curves align closely with the simulated results, exhibiting only a minor deviation. As the DDSIC algorithm progresses through successive iterations, the incremental improvement diminishes, as the majority of residual ISI is eliminated in the early stages. For the TDL-A channel, the BER performance stabilises after the third iteration, indicating that the residual

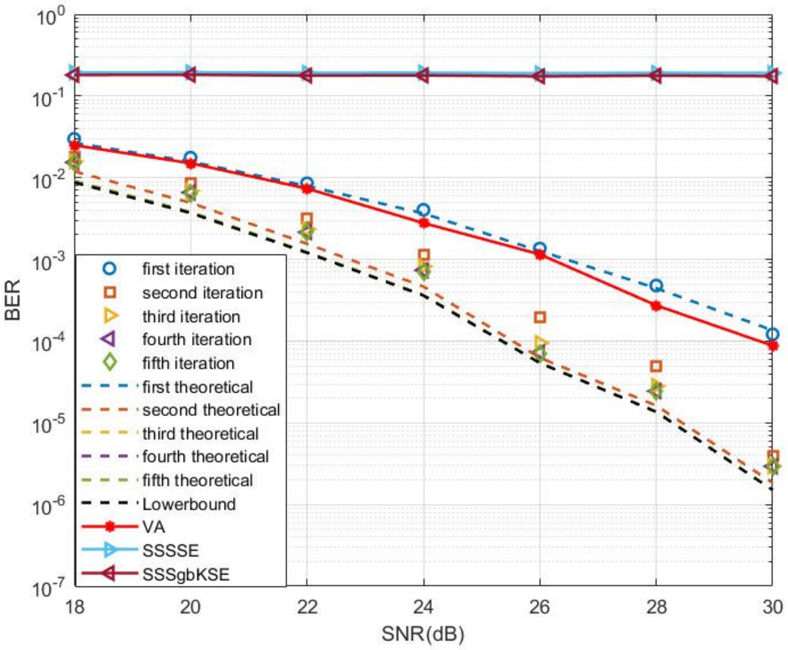

Figure 3.12: BER performance of various algorithms under TDL-D channel with 16-QAM modulation.

ISI becomes negligible compared to the noise floor. A similar trend is observed for the TDL-D channel, where the performance at each iteration marginally exceeds that of the TDL-A channel. In both scenarios, five iterations of the DDSIC algorithm are sufficient to achieve near-optimal interference cancellation.

For a target BER of 10^{-4}, the DDSIC algorithm at the fifth iteration provides an SNR gain of 1.2 dB over SSSgbKSE and 1 dB over the truncated VA algorithm. However, for a target BER of 10^{-5}, DDSIC's performance at the fifth iteration is approximately 1 dB superior to that of the M-BCJR algorithm. Furthermore, compared with ISI-free transmission using Nyquist signalling, the DDSIC algorithm shows a performance gap of about 1.8 dB at the fifth iteration. Notably, the BER performance of the DDSIC algorithm after the third iteration closely approaches the theoretical lower bound, indicating that the majority of ISI has been effectively mitigated.

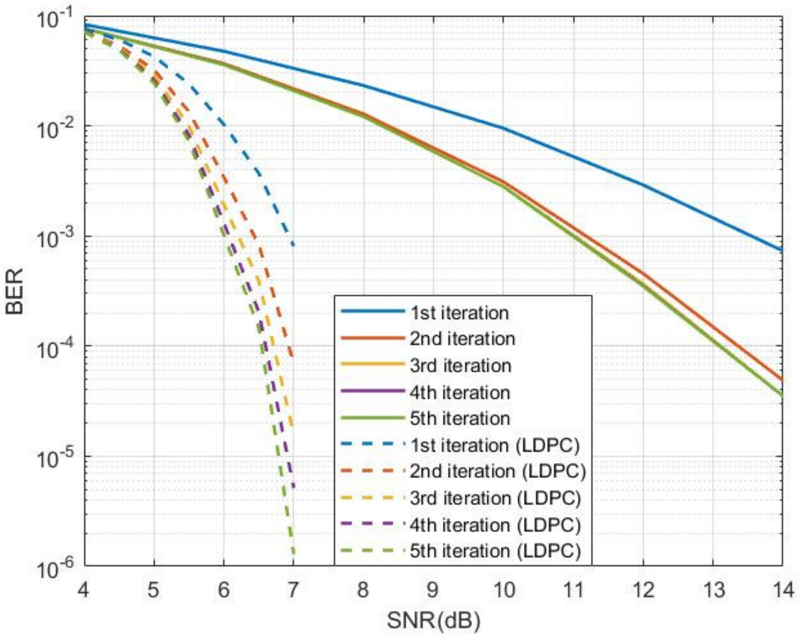

Figure 3.13: BER performance of DDSIC with and without LDPC coding under AWGN channel with QPSK modulation.

3.7.3 DDSIC with Channel Coding Technique

LDPC codes are extensively employed across numerous wireless communication systems, including satellite communication and digital video broadcasting, due to their efficiency in error correction. In this subsection, the BER performance of the DDSIC algorithm is evaluated when applying LDPC coding. Specifically, quasi-cyclic (QC) LDPC coding is employed, where the soft outputs from the final iteration of DDSIC serve as inputs to the LDPC decoder.

For this evaluation, the LDPC code rate is set as 0.75, with a block length of 648 bits, comprising 486 information bits and 162 parity-check bits. Note that this relatively high-rate code is chosen to maintain spectral efficiency and reflect typical settings in practical systems. Although lower-rate LDPC codes can provide stronger error correction capability, they introduce additional redundancy and reduce throughput [115]. Future work may explore performance under different coding rates to assess the trade-off between reliability and efficiency.

Figures 3.13 and 3.14 illustrate the BER performance comparison between the original DDSIC algorithm without channel coding and the LDPC-coded DDSIC scheme employing QPSK modulation. Simulation results demonstrate that the LDPC-coded DDSIC algorithm significantly

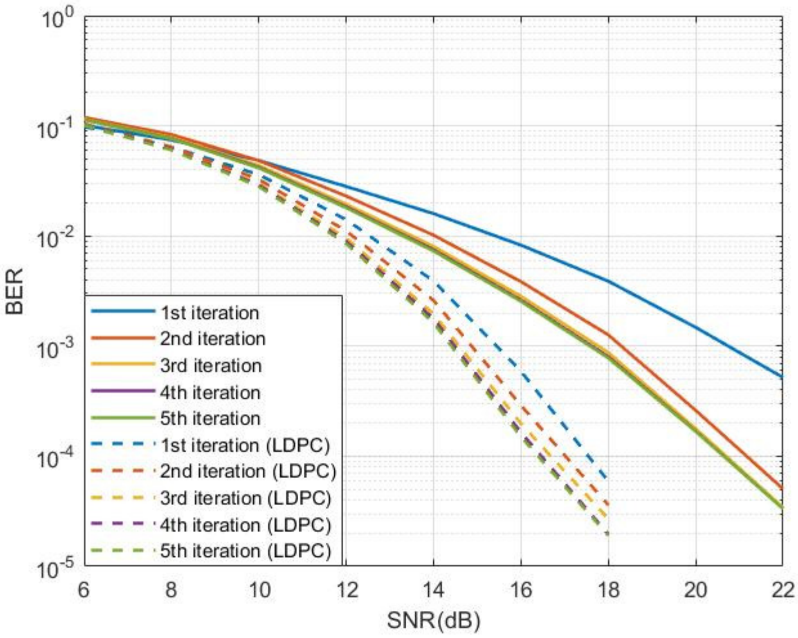

Figure 3.14: BER performance of DDSIC with and without LDPC coding under TDL-A channel with QPSK modulation.

outperforms the original DDSIC scheme without coding. In an AWGN channel, the LDPC-enhanced DDSIC shows an improvement of approximately 6.5 dB in SNR for achieving a target BER of 10^{-4}. Similarly, under the TDL-A channel conditions, the LDPC-coded DDSIC enhances performance by approximately 4.5 dB compared to the fifth iteration of the original DDSIC scheme without coding, also for a target BER of 10^{-4}.

These results indicate that incorporating LDPC coding into the proposed DDSIC algorithm yields substantial performance gains, making the scheme more suitable for practical implementation in real-world wireless communication systems.

3.8 Conclusions

This chapter presents a low-complexity, frame-based DDSIC algorithm for FTN signalling systems. By combining FD-MMSE equalisation with iterative interference cancellation, the proposed approach achieves a significant reduction in computational complexity compared to TD symbol-by-symbol methods.

Theoretical BER expressions are derived for each iteration of DDSIC, along with a lower bound for the algorithm's BER performance. Extensive simulation results validate the robustness of the proposed DDSIC algorithm across diverse modulation schemes and channel conditions, including AWGN, NLOS, and LOS multipath fading environments. The algorithm's superiority is further demonstrated through comparative analysis with state-of-the-art techniques, such as symbol-based methods, the truncated VA, and the M-BCJR algorithm. The derived theoretical BER expressions provide a critical benchmark for evaluating system performance in practical FTN implementations.

Notably, the BER converges rapidly within a few iterations, with significant performance gains achieved at each step. This rapid convergence makes FTN systems viable even for cost-constrained devices. The findings of this work underscore the potential for practical, efficient, and cost-effective deployment of FTN signalling in next-generation wireless communication systems.

3.9 Appendix

The parameters of TDL-A and TDL-D channels are detailed as follows.

Table 3.3: Parameters of TDL-A Channel Model

Tap#	Normalised Delay	Power in dB	Fading Distribution
1	0.000	-13.4	Rayleigh
2	0.3819	0	Rayleigh
3	0.4025	-2.2	Rayleigh
4	0.5868	-4	Rayleigh
5	0.4610	-6	Rayleigh
6	0.5375	-8.2	Rayleigh
7	0.6708	-9.9	Rayleigh
8	0.5750	-10.5	Rayleigh
9	0.7618	-7.5	Rayleigh
10	1.5375	-15.9	Rayleigh
11	1.8978	-6.6	Rayleigh
12	2.2242	-16.7	Rayleigh
13	2.1718	-12.4	Rayleigh
14	2.4942	-15.2	Rayleigh
15	2.5119	-10.8	Rayleigh
16	3.0582	-11.3	Rayleigh
17	4.0810	-12.7	Rayleigh
18	4.4579	-16.2	Rayleigh
19	4.5695	-18.3	Rayleigh
20	4.7966	-18.9	Rayleigh
21	5.0066	-16.6	Rayleigh
22	5.3043	-19.9	Rayleigh
23	9.6586	-29.7	Rayleigh

Table 3.4: Parameters of TDL-D Channel Model

Tap#	Normalised Delay	Power in dB	Fading Distribution
1	0	-0.2	LOS path
1	0	-13.5	Rayleigh
2	0.035	-18.8	Rayleigh
3	0.612	-21	Rayleigh
4	1.363	-22.8	Rayleigh
5	1.405	-17.9	Rayleigh
6	1.804	-20.1	Rayleigh
7	2.596	-21.9	Rayleigh
8	1.775	-22.9	Rayleigh
9	4.042	-27.8	Rayleigh
10	7.937	-23.6	Rayleigh
11	9.424	-24.8	Rayleigh
12	9.708	-30.0	Rayleigh
13	12.525	-27.7	Rayleigh

Chapter 4

Adaptive FTN Signalling over Fast-Fading Channels

To ensure the feasibility of the proposed FTN system in fast-fading channels, the challenge of mitigating Doppler shift, which is among the most significant problems in such environments, is addressed in this chapter. This chapter builds upon the unified FTN system model introduced in Section 3.1, extending it to the delay-Doppler domain. Based on this model, an ATPC module is developed at the transmitter, aiming to mitigate Doppler shifts and convert dynamic CSIs into statistical forms. This transformation enhances the stability and reliability of the DDSIC algorithm under fluctuating channel conditions. Simulation results demonstrate the effectiveness of the ATPC method across various scenarios, highlighting the robustness of the proposed approach in preserving signal integrity in fast-fading environments.

4.1 System Model and Modulation Descriptions

In this section, the FTN system is established employing the ATPC method. OFDM [116], SC-FDE [117], and OTFS [118] modulation schemes are respectively combined with FTN signalling. Additionally, their diversities are evaluated in both TD and FD. The ATPC module is proposed as one modulation alternative to these three modulation schemes.

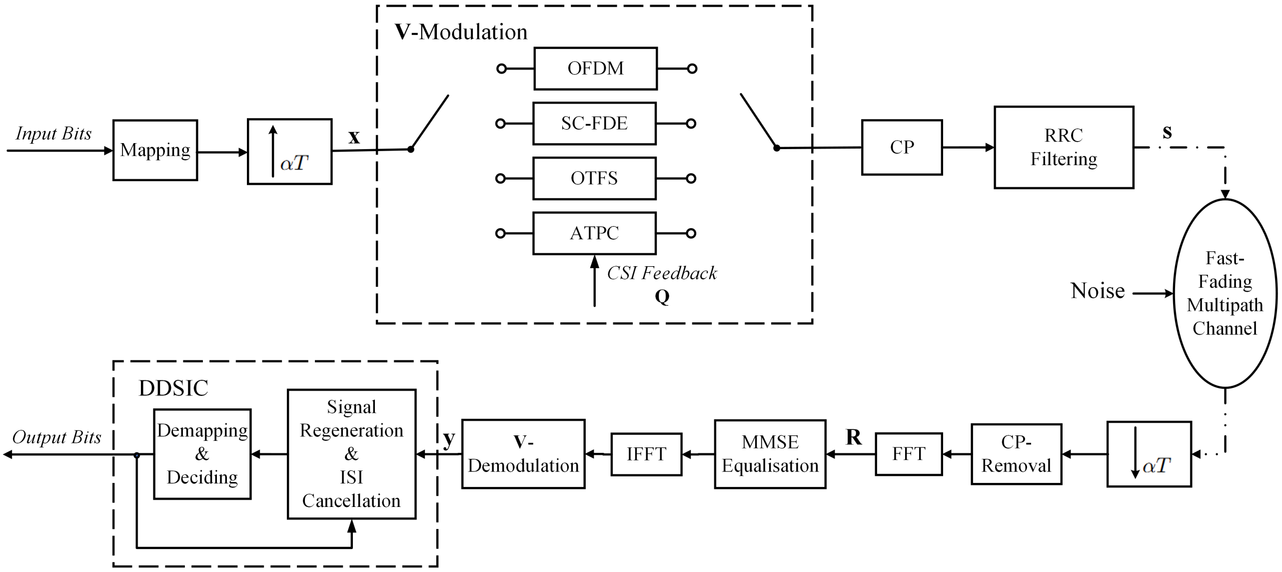

Figure 4.1: Block diagram of the proposed FTN system with ATPC method.

4.1.1 FTN Signal Model and System Model

Figure 4.1 illustrates the proposed FTN system relying on the ATPC method. Initially, input bits are mapped to $M \times N$ QAM symbols and vectorised into an $MN \times 1$ vector $\mathbf{s} = [s_0, s_1, ..., s_{MN-1}]^{\mathbf{T}}$ where M is the number of subcarriers, and N is the number of symbols per subcarrier. Next, symbols are passed through the modulation module which is represented by matrix $\mathbf{V}$. The $\mathbf{V}$-modulation module includes OFDM, SC-FDE, OTFS and the proposed ATPC schemes. Modulated data symbols can be expressed as $\mathbf{x} = \mathbf{V}\mathbf{s}$.

The modulation schemes can be flexibly adjusted by employing different $\mathbf{V}$ matrices and various frame lengths:

- OFDM and SC-FDE modulations: The frame length is set to M symbols (plus overhead), with N set to 1. The modulation matrix is defined as $\mathbf{V} = \mathbf{F}_M^{\mathbf{H}}$ for OFDM and $\mathbf{V} = \mathbf{I}_M$ for SC-FDE, where $\mathbf{F}_M^{\mathbf{H}}$ is the IDFT matrix and $\mathbf{I}_M$ is the identity matrix of order M.
- OTFS modulation: The frame length is set as MN (plus overhead) symbols and N is larger than 1. The modulation matrix is set as $\mathbf{V} = \mathbf{F}_M^{\mathbf{H}} \otimes \mathbf{I}_M$ where $\otimes$ represents the Kronecker product operator.
- ATPC modulation: While employing ATPC, M and N are set as the same as the original three schemes, but the modulation matrix is set as $\mathbf{V} = \mathbf{F}_{MN}^{\mathbf{H}}\mathbf{Q}\mathbf{F}_{MN}$ where $\mathbf{Q}$ is the

CSI feedback matrix obtained from fast-fading channel matrix. The selection of $\mathbf{V}$ is to maximise the output SNR, which will be elaborated in Section 4.2. In this case, OFDM and SC-FDE signals are converted to short-frame signals with a length of M and OTFS signals are converted to long-frame signals with a length of MN.

After $\mathbf{V}$-modulation, a CP is added to avoid inter-frame interference, and signals are then passed through an RRC filter, which is characterised by the roll-off factor β and 3 dB cut-off bandwidth of $1/T$, where T is the Nyquist symbol duration. In this chapter, the RRC filter is configured with $\beta < 1/\alpha - 1$ to avoid the data information loss as previously discussed in Figure 3.3. The accelerated FTN signals are expressed as

$$x(t) = \sum_{i=0}^{MN-1} s_n u(t - n\alpha T), 0 < \alpha < 1, \tag{4.1}$$

where s_n denotes the n-th modulated data symbol with an average power of σ_s^2, $n = 0, 1, 2, ..., MN-1$, and $u(t)$ is the unit-energy RRC shaping pulse.

In this chapter, a fast-fading channel model is defined in the dealy-Doppler domain. The delay-Doppler spreading function is defined as

$$h(\tau, \nu) = \sum_{i=1}^{P} h_i u(\tau - \tau_i) g(\nu - \nu_i), \tag{4.2}$$

where h_i, τ_i, and ν_i denote the channel gain, delay, and Doppler shifts for the i-th path. The term $g(\cdot)$ is defined as a sinc function given by $g(x) = \frac{\sin(\pi x)}{\pi x}$, under the assumption that only rectangular windowing is applied in TD. This formula accommodates both integral and fractional values for time delays and Doppler shifts. Additionally, P represents the total number of paths in the fading channel impulse response (CIR). The corresponding representation of the channel in the frequency-Doppler domain is described as follows:

$$H_\nu(f, \nu) = \int_{-\infty}^{+\infty} h(\tau, \nu) e^{-j2\pi f \tau} d\tau, \tag{4.3}$$

which is determined by h_i, τ_i and ν_i in such a sparse P-path channel.

After passing through the channel, the received signals are sampled with a rate of αT. After CP-removal, the discrete FD signal can be expressed as

$$\mathbf{R} = \mathbf{H}_\nu \mathbf{X} + \mathbf{W}, \tag{4.4}$$

where $\mathbf{X}$ is the FFT of $\mathbf{x}$ and $\mathbf{W}$ is the FD zero-mean AWGN vector with a variance of σ_w^2 for each channel element. $\mathbf{H}_\nu$ is the frequency-Doppler channel matrix defined as

$$\mathbf{H}_\nu = \begin{pmatrix} H_\nu[0,0] & \cdots & H_\nu[0,MN-1] \\ H_\nu[1,0] & \cdots & H_\nu[1,MN-1] \\ \vdots & \ddots & \vdots \\ H_\nu[MN-1,0] & \cdots & H_\nu[MN-1,MN-1] \end{pmatrix}. \tag{4.5}$$

Defining $f_r = 1/(MN\alpha T)$ as the frequency resolution, the element at the i-th row and j-th column of $\mathbf{H}_\nu$ is given by $H_\nu[i,j] = H_\nu(if_r, jf_r)$. Considering Doppler shift, $\mathbf{H}_\nu$ has a stripe diagonal structure, and the stripe width is $2K_{max}+1$, where K_{max} is the maximum Doppler shift.

At the receiver side, the signals are equalised by an FD-MMSE equaliser defined as

$$\mathbf{E}_\nu = \mathbf{H}_\nu^{\mathbf{H}}(\mathbf{H}_\nu\mathbf{H}_\nu^{\mathbf{H}} + \frac{1}{\gamma_{in}}\mathbf{I}_{MN})^{-1}, \tag{4.6}$$

and thus the equalised FD signal is derived as

$$\hat{\mathbf{X}} = \mathbf{E}_\nu\mathbf{R} = \mathbf{E}_\nu\mathbf{H}_\nu\mathbf{X} + \mathbf{E}_\nu\mathbf{W}. \tag{4.7}$$

Then, the $\mathbf{V}$-demodulation is applied to recover the equalised signals, followed by the application of the DDSIC algorithm, as introduced in Section 3.3, to mitigate the ISI effect. It is important to note that the operation of the DDSIC algorithm is significantly disrupted by the dynamic CSI under fast-fading channel conditions. In such scenarios, the continuously varying CSIs hinder the algorithm's ability to accurately estimate and cancel ISI. As a result, when conventional modulation schemes such as OFDM, SC-FDE, and OTFS are employed, the system performance experiences notable degradation in fast-fading environments. In contrast, the proposed ATPC scheme, which will be introduced in detail in Section 4.2, ensures a more robust system performance. By mitigating the adverse effects of fast-fading channels, the ATPC scheme demonstrates superior compatibility with the DDSIC algorithm, leading to significantly improved ISI cancellation and overall performance.

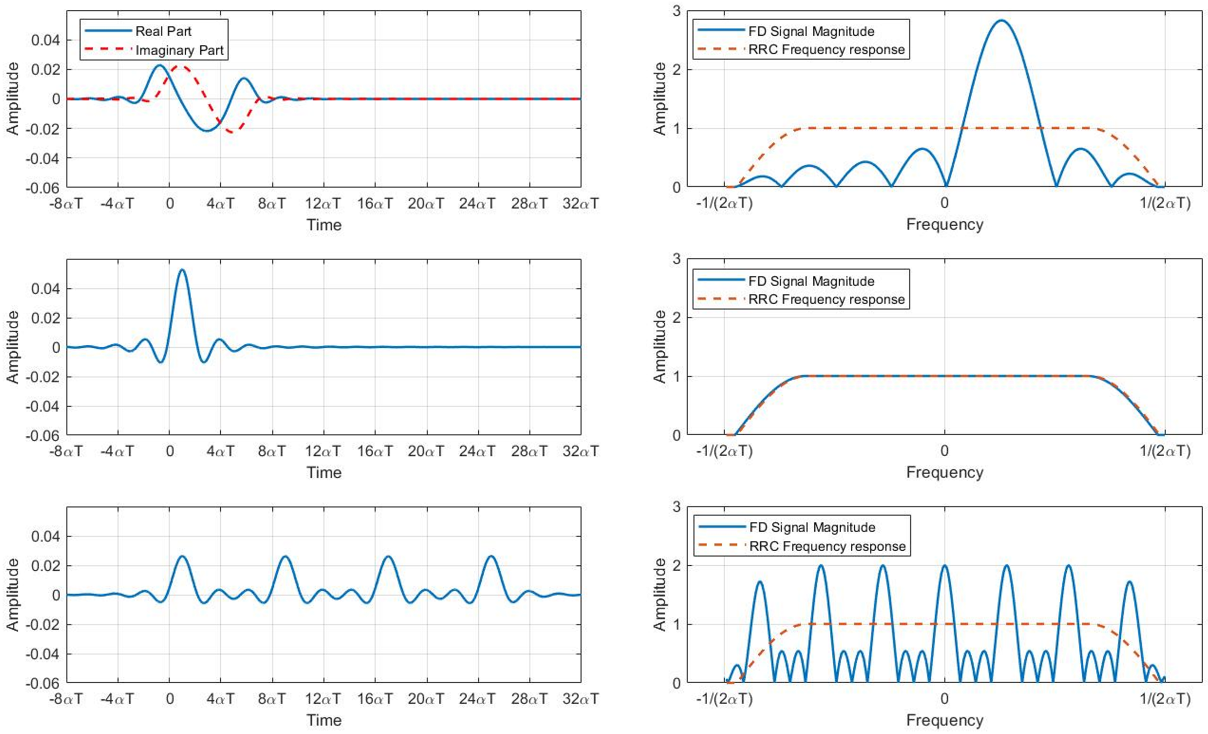

(a)

(b)

Figure 4.2: Illustrations of modulated signal waveforms in (a) TD and (b) FD. The subplots from top to bottom represent OFDM ($M = 8, N = 1$), SC-FDE ($M = 8, N = 1$) and OTFS ($M = 8, N = 4$) schemes, respectively.

4.1.2 Diversity Order of Various Modulation Schemes

The diversity order in fast-fading channels is a critical metric for system design, as it directly impacts the reliability and performance of wireless communication systems [49]. In this chapter, time diversity and frequency diversity are employed as benchmarks to evaluate the potential compatibility of the three non-adaptive modulation schemes in FTN systems. For illustration purposes, a single data sequence $\mathbf{s} = [0, 1, 0, 0, 0, 0, 0, 0]^{\mathbf{T}}$ is transmitted with unit power adopting system parameters as $[\alpha, \beta] = [0.8, 0.2]$, $M = 8$ and $N = 1$ or 4. Both the TD and FD waveforms of modulated signals are presented in Figure 4.2.

The TD and FD signals for OFDM integrated with FTN are illustrated in the first subplots of Figure 4.2 (a) and Figure 4.2 (b), respectively. In TD, the OFDM signal represents a superposition of sinusoidal waves within a single FTN symbol duration ($8\alpha T$). This characteristic ensures that the time-variant channel has a limited impact on information recovery because each data symbol persists throughout the entire OFDM symbol duration. This persistence grants OFDM time diversity. However, in FD, some subcarrier components are suppressed due to FTN pulse shaping, which filters out a portion of the data signal. The situation further degrades subcarrier components, making symbol recovery more challenging in frequency-selective channels. Consequently, OFDM integrated with FTN fails to achieve frequency diversity.

In contrast, the second subplots of Figure 4.2 (a) and Figure 4.2 (b) present the waveforms for SC-FDE with FTN signalling. In this scheme, the data information is carried by a single carrier, spreading the signal power across the available bandwidth. In TD, SC-FDE signals can be severely affected by channel fluctuations in time-varying environments, causing SC-FDE to fail in achieving time diversity. However, in FD, frequency-selective fading has a limited effect on data recovery because the frequency components are spread across the entire spectrum, enabling SC-FDE to achieve frequency diversity.

OTFS, as shown in the third subplots of Figure 4.2 (a) and Figure 4.2 (b), emerges as a promising solution for fast-fading channels due to its high reliability and diversity gain. Its potential for integration with FTN transmission remains largely unexplored in the literature. In TD, OTFS spreads each data symbol across N time slots. This replication provides resilience against time-varying propagation, thereby offering time diversity. In FD, OTFS divides the bandwidth into M sub-bands, distributing the signal components across all these sub-bands. Although the RRC filter used for FTN transmission might suppress edge components in the passband, critical data information is retained in other FD sub-bands. This allows for symbol recovery at the receiver, ensuring that FTN-OTFS also achieves frequency diversity. Thus, the integration of FTN signalling with OTFS does not destroy either time or frequency diversity, making it an ideal candidate for practical fast-fading channels, combining robustness with spectral efficiency.

4.2 Performance Analysis and ATPC Method

In this section, the ATPC method is introduced in detail. As the aim of this method is to maximise the output SNR, conventional systems under fast-fading conditions are analysed.

Following this, the mathematical formulas of the proposed ATPC method are derived to present how ATPC mitigates Doppler effects and enhances overall system performance.

4.2.1 V-Demodulation

After FD-MMSE equalisation, signals are processed by IFFT and then demodulated by the conjugate transpose of $\mathbf{V}$ matrix, i.e., $\mathbf{V^H}$. Assume that $\mathbf{V}$-modulation and $\mathbf{V}$-demodulation are reciprocal processes, $\mathbf{V}$ and $\mathbf{V^H}$ satisfy $\mathbf{VV^H} = \mathbf{V^HV} = \mathbf{I}_{MN}$. Building upon this, the demodulated signals are expressed as

$$\begin{aligned} \mathbf{y} &= \mathbf{V^H F^H}_{MN}\hat{\mathbf{X}} \\ &= \mathbf{V^H F^H}_{MN}\mathbf{E}_\nu \mathbf{H}_\nu \mathbf{F}_{MN}\mathbf{V}\mathbf{s} + \mathbf{V^H F^H}_{MN}\mathbf{E}_\nu \mathbf{F}_{MN}\mathbf{w}. \end{aligned} \tag{4.8}$$

Observe that this is still a linear system similar to Eq. (3.6). Therefore, the new transfer matrix from $\mathbf{s}$ to $\mathbf{y}$ is defined as

$$\mathbf{P} = \mathbf{V^H F^H}_{MN}\mathbf{E}_\nu \mathbf{H}_\nu \mathbf{F}_{MN}\mathbf{V}. \tag{4.9}$$

In fast-fading scenarios, channel matrix $\mathbf{H}_\nu$ is no longer a circular matrix as in Chapter 3 and thus cannot be directly decomposed. To solve this problem, the Hermitian matrix $\mathbf{H}_\nu^{\mathbf{H}}\mathbf{H}_\nu$ is eigenvalue-based decomposed as

$$\mathbf{H}_\nu^{\mathbf{H}}\mathbf{H}_\nu = \mathbf{Q}\mathbf{\Psi}\mathbf{Q^H}, \tag{4.10}$$

where $\mathbf{Q}$ involves the CSI and is later fed back to the transmitter for ATPC. It is a unitary matrix of order $MN \times MN$, satisfying $\mathbf{QQ^H} = \mathbf{Q^HQ} = \mathbf{I}_{MN}$. The matrix $\mathbf{\Psi}$ is diagonal, with its diagonal elements denoted as λ_i, representing the eigenvalues of the matrix $\mathbf{H}_\nu^{\mathbf{H}}\mathbf{H}_\nu$.

Defining $\mathbf{U} = \mathbf{V^H F^H}_{MN}\mathbf{Q}$, the decomposed form of $\mathbf{P}$ is derived as (see Appendix in Section 4.6)

$$\mathbf{P} = \mathbf{I}_{MN} - \mathbf{U}\mathrm{diag}\left\{\frac{1}{\gamma_{in}\lambda_i + 1}\right\}\mathbf{U^H}, \tag{4.11}$$

Based on the MMSE principle, the normalised noise-plus-interference power for the j-th equalised data symbol y_j which is the j-th element in $\mathbf{y}$ can be expressed as

$$\begin{aligned} J_j &= 1 - \sum \mathbf{P}[j,j] \\ &= \sum_{i=0}^{MN-1} \frac{1}{\gamma_{in}\lambda_i + 1}|\mathbf{U}[j,i]|^2. \end{aligned} \tag{4.12}$$

The output SNR for the j-th symbol after MMSE equalisation can also be derived as

$$\gamma_{out}[j] = \frac{1 - J_j}{J_j}. \tag{4.13}$$

It is highlighted that the output SNR is independent of the transmitted data symbol $\mathbf{x}[j]$. This is because both the average power of the transmitted signal and the shaping pulse have been normalised to 1. This expression remains consistently reliable and applicable across different modulation techniques, providing a consistent and reliable metric for evaluating signal quality in various communication scenarios.

4.2.2 Adaptive Transmission Precoding

The purpose of ATPC is in two aspects. Firstly, ATPC should ensure that the power of noise is minimised. By achieving this, the output SNR should be maximised. Secondly, this scheme also requires to effectively alleviate the Doppler effect. This can be accomplished by establishing a decomposed matrix form with slow-fading characteristics. Such a form guarantees the effectiveness and reliability of the DDSIC algorithm even in fast-fading circumstances.

As can be inferred from Eq. (4.12), the power of noise-plus-interference is dependent on the matrix $\mathbf{U}$, which is affected by the modulation matrix $\mathbf{V}$ and the eigenvector matrix $\mathbf{Q}$. Since the BER for the symbol determined on the j-th element of $\mathbf{y}$ is established based on a convex transformation of J_j via the SNR $\gamma_{out}[j]$ and a $Q(\cdot)$ function [111], the average BER for all symbols can be considered as the mean implemented following the convex transformation. According to *Jensen's Inequality*[1], the average BER is minimised when all J_j are the same and equal to the mean of J_j. From Eq. (4.12), the average value of J_j can be expressed as

$$\begin{aligned} J &= 1 - \frac{1}{MN}\mathrm{Tr}\{\mathbf{P}\} \\ &= \frac{1}{MN}\sum_{i=0}^{MN-1}\frac{1}{\gamma_{in}\lambda_i + 1}. \end{aligned} \tag{4.14}$$

From Eqs. (4.12) and (4.14), it is obvious that when $|\mathbf{U}[j,i]|^2 = 1$, all J_j are the same and equal to J. Then, the average BER is minimised. As $\mathbf{U}$ is an orthogonal matrix, it can be set

---

[1] Jensen's inequality states that the convex transformation of a mean is always less than or equal to the mean applied after convex transformation [119].

as the IFFT matrix, i.e., $\mathbf{U} = \mathbf{F}_{MN}^{\mathbf{H}}$.

Therefore, the modulation matrix V while employing ATPC is derived from $\mathbf{U}$ as

$$\mathbf{V} = \mathbf{F}_{MN}^{\mathbf{H}} \mathbf{Q} \mathbf{F}_{MN}. \tag{4.15}$$

It is shown that in Eq. (4.15), the modulation matrix is chosen according to $\mathbf{Q}$, which is adaptive to fluctuated channel conditions.

Furthermore, with ATPC applied, $\mathbf{P}$ becomes

$$\begin{aligned} \mathbf{P} &= \mathbf{I}_{MN} - \mathbf{F}_{MN}^{\mathbf{H}} \mathrm{diag}\left\{ \frac{1}{\gamma_{in}\lambda_i + 1} \right\} \mathbf{F}_{MN} \\ &= \mathbf{F}_{MN}^{\mathbf{H}} \mathrm{diag}\left\{ \frac{\gamma_{in}\lambda_i}{\gamma_{in}\lambda_i + 1} \right\} \mathbf{F}_{MN}, \end{aligned} \tag{4.16}$$

which is a circular matrix with the same diagonal elements.

Additionally, Eqs. (4.12) and (4.13) become

$$J = \frac{1}{MN} \sum_{i=0}^{MN-1} \frac{1}{\gamma_{in}\lambda_i + 1} \tag{4.17}$$

and

$$\gamma_{out} = \frac{1-J}{J} = \frac{1}{\frac{1}{MN} \sum_{i=0}^{MN-1} \frac{1}{\gamma_{in}\lambda_i + 1}} - 1. \tag{4.18}$$

In this thesis, the feedback matrix $\mathbf{Q}$ is assumed to be constant. Although the CSI changes rapidly across all OTFS schemes, MN samples fall within a coherent processing interval. Within this interval, the channel parameters can be approximated as invariant. Additionally, the principles of channel reciprocity and robustness in rapidly fading time division duplex (TDD) systems still hold [120].

4.2.3 Performance after DDSIC

As discussed in the last subsection, the demodulated signals are in the same form as in Chapter 3. Therefore, defining $\mathbf{G} = \mathbf{V}^{\mathbf{H}} \mathbf{F}_{MN}^{\mathbf{H}} \mathbf{E}_{\nu} \mathbf{F}_{MN}$, the ISI-aware decomposed $\mathbf{y}$ as

$$\begin{aligned} \mathbf{y} &= \mathbf{P}\mathbf{s} + \mathbf{G}\mathbf{w} \\ &= p_0 \mathbf{s} + (\mathbf{P} - p_0 \mathbf{I}_{MN})\mathbf{s} + \mathbf{G}\mathbf{w}, \end{aligned} \tag{4.19}$$

where p_0 is the diagonal element in $\mathbf{P}$, $\mathbf{w}$ represents the TD noise vector before equalisation. The three components, from left to right, represent the desired signal, ISI, and noise, respectively.

Similar to Eq. (3.26), assuming all the ISI is removed by DDSIC, the output SNR can be derived in the presence of noise only as

$$\begin{aligned}\gamma_0 &= \frac{\text{Power}\left\{\text{desired signal}\right\}}{\text{Power}\left\{\text{noise}\right\}} \\ &= \frac{1}{MN}\frac{\left(\sum_{i=0}^{MN-1}\frac{\gamma_{in}\lambda_i}{\gamma_{in}\lambda_i+1}\right)^2}{\sum_{i=0}^{MN-1}\frac{\gamma_{in}\lambda_i}{(\gamma_{in}\lambda_i+1)^2}}.\end{aligned} \tag{4.20}$$

The detailed derivation is provided in Section 4.7.

Then, the BER lower bound is derived as

$$\begin{aligned}P_b &\approx \frac{2(1-2^{-k})}{k}Q\left(\sqrt{\frac{3}{4^k-1}\gamma_0}\right) \\ &= \frac{2(1-2^{-k})}{k}Q\left(\sqrt{\frac{3}{4^k-1}}\sqrt{\frac{1}{MN}\frac{\left(\sum_{i=0}^{MN-1}\frac{\gamma_{in}\lambda_i}{\gamma_{in}\lambda_i+1}\right)^2}{\sum_{i=0}^{MN-1}\frac{\gamma_{in}\lambda_i}{(\gamma_{in}\lambda_i+1)^2}}}\right).\end{aligned} \tag{4.21}$$

where k is the modulation order (for 4-QAM, $k=1$, and for 16-QAM, $k=2$, etc.)

4.3 Performance Benchmarks in Extreme Conditions

In this section, two extreme channel conditions including infinite CIR paths and infinite maximum Doppler frequencies are considered. Corresponding BER expressions are derived to evaluate the system performance under these conditions.

4.3.1 Eigenvalue Distribution Discussion

Since the roll-off factor of the RRC filter is configured as $\beta < 1/\alpha - 1$, zero samples are transmitted and result in zero eigenvalues after the decomposition of $\mathbf{H}_\nu^{\mathbf{H}}\mathbf{H}_\nu$. Therefore, the conventional eigenvalue probability density functions (PDFs) of a full-rank Hermitian matrix should be improved to account for the FTN environment.

As shown in the lower subfigure in Figure 3.3, non-zero samples, which are characterised by the conventional PDFs, account for a fraction of $\alpha(1+\beta)$ of the FTN signal bandwidth. Therefore, considering that all zero eigenvalues induced by the RRC filtering are represented by an impulse function as $MN \to \infty$ in the eigenvalue PDFs, and defining $\eta = \alpha(1+\beta)$, the improved eigenvalue PDFs can be expressed as $\eta p_\lambda(\rho) + (1-\eta)\delta(\rho)$, where $p_\lambda(\cdot)$ denotes the conventional full-rank eigenvalue PDFs, ρ is the eigenvalue variable, and $\delta(\cdot)$ represents the Dirac delta function.

Then, the output SNR in ISI-free condition is reformulated as

$$\gamma_0 = \frac{(1 - \frac{1}{MN}\sum_{i=0}^{MN-1}\frac{1}{\gamma_{in}\lambda_i+1})^2}{\frac{1}{MN}\sum_{i=0}^{MN-1}\frac{1}{\gamma_{in}\lambda_i+1} - \frac{1}{MN}\sum_{i=0}^{MN-1}\frac{1}{(\gamma_{in}\lambda_i+1)^2}}, \tag{4.22}$$

which is the foundation of follow-up analysis.

4.3.2 Extreme Case One: Zero Doppler

In the first extreme condition, it is assumed that there are infinite independent fading CIR paths without Doppler shifts in any of the multipath components. In this situation, the signal transmission achieves full frequency diversity, and thus, the BER approaches its lower bound, which indicates an extremely slow-fading condition.

The FD channel matrix is expressed as $\mathbf{H}_\nu = \mathrm{diag}\{\psi_i\}$ where ψ_i represents the fading gain of each path obeying Gaussian distribution. Therefore, the eigenvalue $\lambda_i = |\psi_i|^2$ follows a chi-square distribution with two degrees of freedom, following a PDF of $p_\lambda(\rho) = e^{-\rho}$ [121]. For FTN systems, the PDF is modified to $\eta e^{-\rho} + (1-\eta)\delta(\rho)$, where η accounts for the fraction of non-zero eigenvalues, while $(1-\eta)$ represents the fraction of zero-eigenvalues resulting from RRC filtering. Consequently, for the adaptive transmission regime as $MN \to \infty$, the output SNR for the ISI-decontaminated symbols can be expressed as

$$\begin{aligned} \gamma_{low} &= \frac{[1 - \int_0^\infty \frac{\eta e^{-\rho}+(1-\eta)\delta(\rho)}{\gamma_{in}\rho+1}d\rho]^2}{\int_0^\infty \frac{\eta e^{-\rho}+(1-\eta)\delta(\rho)}{\gamma_{in}\rho+1}d\rho - \int_0^\infty \frac{\eta e^{-\rho}+(1-\eta)\delta(\rho)}{(\gamma_{in}\rho+1)^2}d\rho} \\ &= \frac{\eta\gamma_{in}(1 - \frac{1}{\gamma_{in}}E_1(\frac{1}{\gamma_{in}})e^{\frac{1}{\gamma_{in}}})^2}{E_1(\frac{1}{\gamma_{in}})e^{\frac{1}{\gamma_{in}}} + \frac{1}{\gamma_{in}}E_1(\frac{1}{\gamma_{in}}) - e^{-\frac{1}{\gamma_{in}}}}, \end{aligned} \tag{4.23}$$

where $E_1(\cdot)$ is the first-order exponential integral function defined as

$$E_1(z) = \int_z^\infty \frac{e^{-t}}{t}dt. \tag{4.24}$$

The BER lower bound is derived as

$$P_{b,low} = \frac{2(1-2^{-k})}{k} Q\left(\sqrt{\frac{3}{4^k-1}\frac{\eta\gamma_{in}(1-\frac{1}{\gamma_{in}}E_1(\frac{1}{\gamma_{in}})e^{\frac{1}{\gamma_{in}}})^2}{E_1(\frac{1}{\gamma_{in}})e^{\frac{1}{\gamma_{in}}}+\frac{1}{\gamma_{in}}E_1(\frac{1}{\gamma_{in}})-e^{-\frac{1}{\gamma_{in}}}}}\right). \tag{4.25}$$

4.3.3 Extreme Case Two: Infinite Doppler

The second extreme case assumes the severe impact caused by Doppler effects. In this case, the Doppler frequencies are uniformly distributed in infinite paths with $K_{max} \to \infty$. Every element in $\mathbf{H}_\nu$ obeys Gaussian random distribution. Therefore, $\mathbf{H}_\nu^{\mathbf{H}}\mathbf{H}_\nu$ obeys Wishart distribution and $p_\lambda(\rho) = \frac{1}{2\pi}\sqrt{\frac{4-\rho}{\rho}}, 0 \leqslant \rho \leqslant 4$ [122] in Nyquist systems. In FTN system, the PDF is approximated as $\eta\frac{1}{2\pi}\sqrt{\frac{4-\rho}{\rho}} + (1-\eta)\delta(\rho)$, and the ISI-free output SNR under the adaptive transmission regime can be formulated for $MN \to \infty$, as

$$\begin{aligned}\gamma_{up} &= \frac{[1-\int_0^4 \frac{\frac{1}{2\pi}\sqrt{\frac{4-\rho}{\rho}}\eta+(1-\eta)\delta(\rho)}{\gamma_{in}\rho+1}d\rho]^2}{\int_0^4 \frac{\frac{1}{2\pi}\sqrt{\frac{4-\rho}{\rho}}\eta+(1-\eta)\delta(\rho)}{\gamma_{in}\rho+1}d\rho - \int_0^4 \frac{\frac{1}{2\pi}\sqrt{\frac{4-\rho}{\rho}}\eta+(1-\eta)\delta(\rho)}{(\gamma_{in}\rho+1)^2}d\rho} \\ &= \frac{\eta(1-\frac{\sqrt{4\gamma_{in}+1}-1}{2\gamma_{in}})^2}{\frac{\sqrt{4\gamma_{in}+1}-1}{2\gamma_{in}} - \frac{1}{\sqrt{4\gamma_{in}+1}}}.\end{aligned} \tag{4.26}$$

Therefore, the infinite-Doppler BER expression is given by

$$P_{b,up} = \frac{2(1-2^{-k})}{k} Q\left(\sqrt{\frac{3}{4^k-1}\frac{\eta(1-\frac{\sqrt{4\gamma_{in}+1}-1}{2\gamma_{in}})^2}{\frac{\sqrt{4\gamma_{in}+1}-1}{2\gamma_{in}} - \frac{1}{\sqrt{4\gamma_{in}+1}}}}\right). \tag{4.27}$$

4.4 Simulation Results

In this section, the BER performance of the proposed ATPC-aided FTN system under various channel conditions are assessed. The system parameters are summarised in Table 4.1. As discussed in Section 4.1.1, after applying ATPC, $\mathbf{V}$ depends solely on the feedback information $\mathbf{Q}$, the number of subcarriers M, and the number of symbols per subcarrier N. Therefore, the OFDM and SC-FDE modulations become equivalent and are collectively referred to as a short-frame adaptive scheme, characterised by a frame length of M symbols with the addition of a CP. Similarly, OTFS applying ATPC is denoted as a long-frame adaptive scheme, with a frame length of MN symbols along with a CP.

Table 4.1: Simulation Parameters I

No. of Subcarriers (M)	256	No. of Symbols in Each Subcarrier (N)	32
Time Acceleration Factor (α)	0.8	Roll-off Factor of RRC Filter (β)	0.2
Carrier Frequency (f_c)	6 GHz	Subcarrier Spacing (Δf)	6.144 MHz
Nyquist Bandwidth ($W = \alpha M \Delta f$)	30 kHz	Nyquist Symbol Duration ($T = 1/W$)	162.76 ns
Delay Resolution ($d_r = \alpha T$)	162.76 ns	Doppler Resolution ($f_r = 1/(MN\alpha T)$)	750.002 Hz
Bandwidth of FTN Symbols ($B = (1+\beta)/T)$)	7.37 MHz		

To explore the feasibility of integrating FTN signalling with these three modulation methods, the BER performances of OFDM-FTN, SC-FDE-FTN, and OTFS-FTN using both QPSK and 16-QAM mapping schemes are compared. Without loss of generality, both LOS and NLOS multipath fading channels are considered for evaluating BER performance. The remaining parameters of the TDL-A and TDL-D channel models, including multipath time delay information, are detailed in Table 4.2.

Table 4.2: Simulation Parameters II

Maximum Speed (v_{max})	500 km/h	Maximum Doppler Frequency ($f_{max} = f_c \frac{v_{max}}{v_c}$, $v_c = 3 \times 10^8$m/s)	2777.8 Hz
No. of Doppler Shifts (Positive or Negative) ($K_{max} = \lceil \frac{f_{max}}{f_r} \rceil$)	≈ 3	Maximum Delay (d_{max})	3820.6 ns (LOS), 3506.1 ns (NLOS)
No. of Multipaths ($L_{max} = \lceil \frac{d_{max}}{d_r} \rceil$)	29 (LOS), 27 (NLOS)		

4.4.1 Resistance of ATPC to Doppler Effect

To evaluate whether ATPC can create a relatively Doppler-free environment for effective ISI cancellation, it is assumed that each path has equal power, maintaining $P = M$ to ensure full multipath diversity. In this case, the BER performance of long-frame adaptive transmission comprising MN data symbols per frame is observed by adjusting the value of K_{max}.

As shown in Figure 4.3, when K_{max} is below a threshold of 8, the BERs of FTN adaptive transmission without DDSIC remain nearly identical, demonstrating that ATPC effectively mitigates the Doppler effect. While employing QPSK modulation and $K_{max} < 8$, where the maximum speed reaches up to 1350 km/h, the Doppler effect is effectively eliminated, which corresponds to an aircraft-level scenario. Furthermore, when K_{max} exceeds this threshold, ATPC is unable to entirely eliminate the Doppler effect, leading to a deterioration in BER performance. However, this degradation remains within an acceptable range, enabling the effective application of DDSIC.

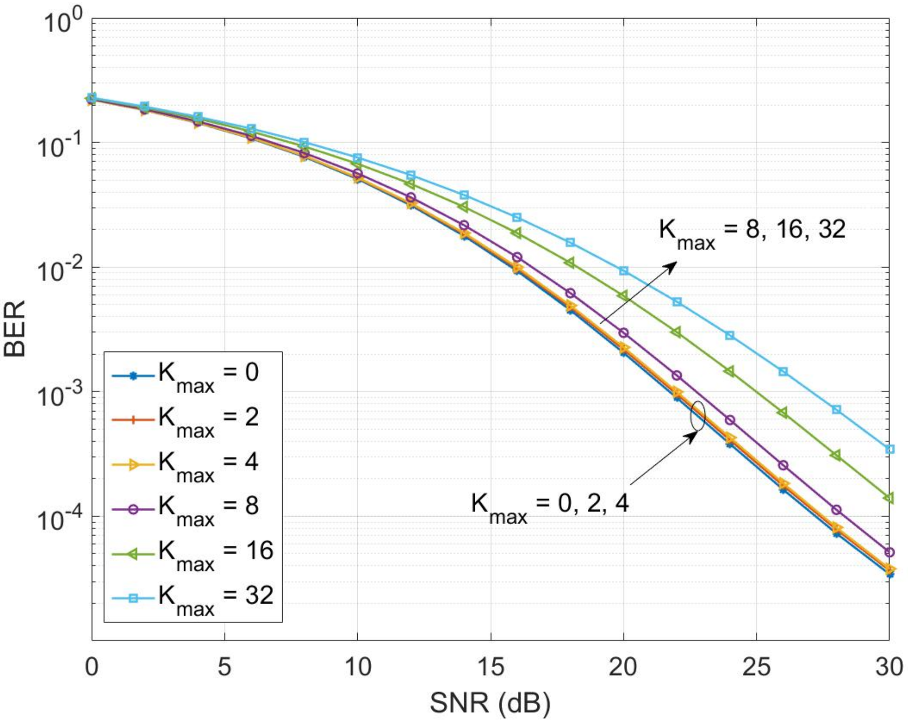

Figure 4.3: BER comparison between adaptive transmission (without DDSIC), with different maximum Doppler shift under fast-fading channel with QPSK mapping.

4.4.2 BER Performance Comparison after DDSIC

All the simulated modulation schemes are presented in Table 4.3, and the BER comparisons are displayed in Figures 4.4 and 4.5. Observe in these two figures that the proposed ATPC-aided DDSIC scheme demonstrates a satisfactory performance under both LOS and NLOS channels and for both QPSK and 16-QAM mappings. As the time-selectivity is relatively moderate, while the frequency-selectivity is prominent in the considered channels, the influence of time variability is lower compared to the significant effects of frequency selectivity. Therefore, the OFDM-FTN scheme is unable to achieve full diversity and presents a deteriorated performance in every condition. Adopting QPSK mapping and a target BER of 10^{-5}, the ATPC shows a 12 dB gain when DDSIC is utilised. It is notable that long-frame transmission leads to better performance than short-frame transmission. For the target BER of 10^{-5}, there is a 1 dB difference between the two transmission schemes under LOS channels and a 2 dB difference under NLOS channels. When 16-QAM is adopted, the ISI has such a serious impact on the system performance, so the schemes without interference cancellation do not function. However,

Table 4.3: Modulation Scheme Description

No.	Modulation Scheme	Frame Length (Short for $M = 256, N = 1$ Long for $M = 256$, $N = 32$)	Channel Type	Combined with ATPC	Combined with DDSIC
1	OFDM	Short	LOS	×	×
2	SC-FDE	Short	LOS	×	×
3	OTFS	Long	LOS	×	×
4	OFDM/SC-FDE	Short	LOS	✓	×
5	OTFS	Long	LOS	✓	×
6	OFDM/SC-FDE	Short	LOS	✓	✓
7	OTFS	Long	LOS	✓	✓
8	OFDM	Short	NLOS	×	×
9	SC-FDE	Short	NLOS	×	×
10	OTFS	Long	NLOS	×	×
11	OFDM/SC-FDE	Short	NLOS	✓	×
12	OTFS	Long	NLOS	✓	×
13	OFDM/SC-FDE	Short	NLOS	✓	✓
14	OTFS	Long	NLOS	✓	✓

ATPC-aided DDSIC still performs well and for the target BER of 10^{-5}, there is only a 0.2 dB difference between the long and short-frame adaptive transmission schemes under LOS channels and a 4 dB difference under NLOS channels.

Considering the practical transmission related to imperfect channel states, the BER performance comparison of an ideal and two practical long-frame transmission scenarios is presented in Figure 4.6. The first scenario considers fractional time delays and Doppler shifts, and the second considers channel estimation errors simulated by introducing zero-mean AWGN with a variance of $\frac{1}{2\gamma_{in}}$, leading to imperfect CSI feedback. The simulation outcomes show that the proposed scheme is resilient to both practical scenarios. In the first scenario, for the target BER of 10^{-5}, the differences between fractional delay-Doppler and perfect transmission are

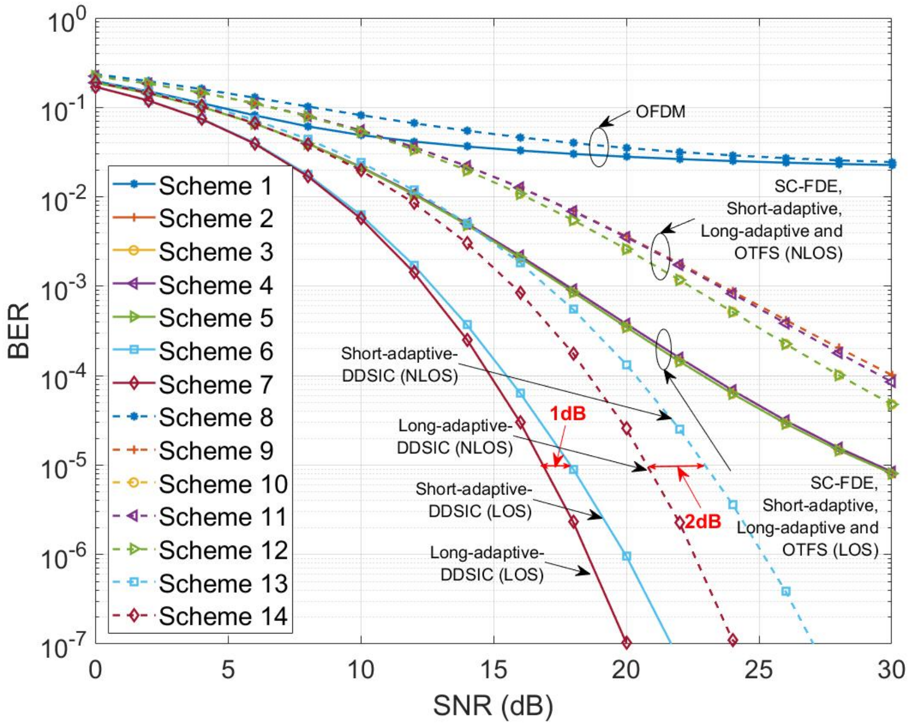

Figure 4.4: BER comparison between different modulation schemes with QPSK mapping under LOS and NLOS channels.

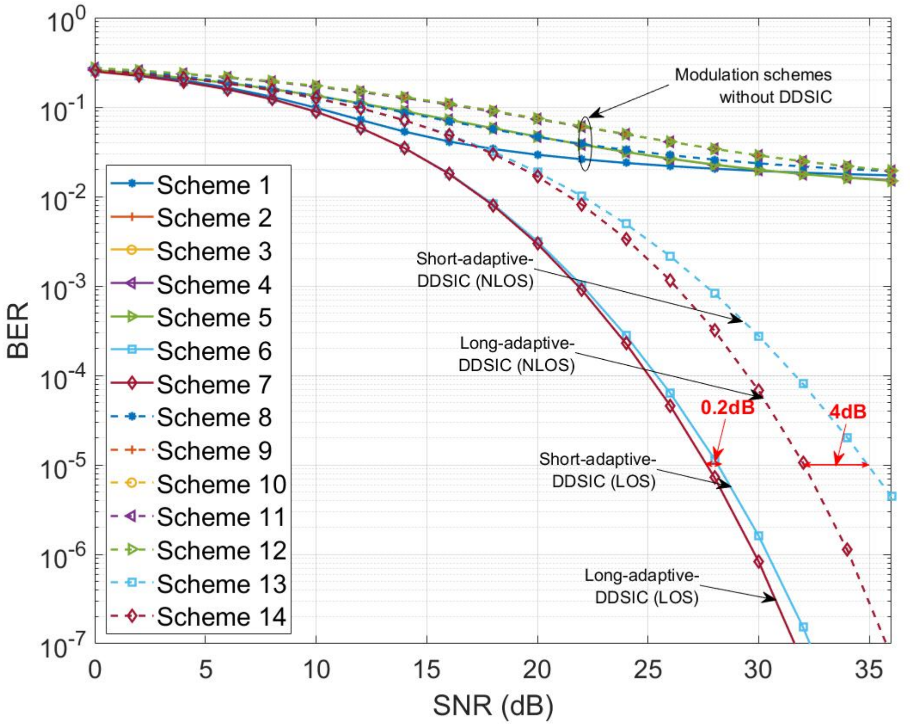

Figure 4.5: BER comparison between different modulation schemes with 16-QAM mapping under LOS and NLOS channels.

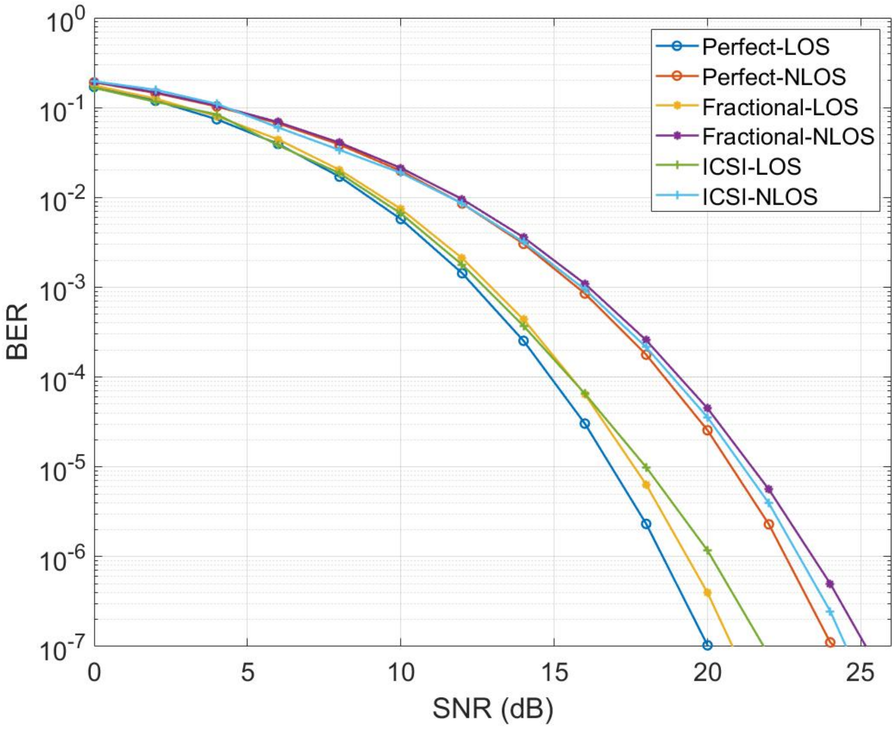

Figure 4.6: BER comparison of perfect and imperfect transmission scenarios under LOS and NLOS channels with QPSK mapping.

merely 1 dB under LOS channels and 0.5 dB under NLOS channels. Concerning the second scenario, for the target BER of 10^{-5}, the differences between imperfect CSI feedback and perfect transmission are only 1.5 dB under LOS channels and 1 dB under NLOS channels.

4.4.3 Extreme Case Benchmarks

In this subsection, the BER performances in two extreme cases discussed in Section 4.3 are evaluated. Frequency-selective Rayleigh fading channels are utilised where all paths are independent and have equal power, and the Doppler shift is assumed to be static and uniformly distributed from $-K_{max}$ to K_{max}.

In the first extreme case, K_{max} is maintained as 0 but P increases. Then the theoretical BER curves are compared with the derived lower bound. Observe in Figure 4.7 that, as P approaches M, the BER curves increasingly converge towards the derived lower bound. Due to the approximation of the eigenvalue PDF, there is a gap of approximately 2 dB between the lower bound derived and the theoretical BER curve for $P = M$ at the target BER of 10^{-5}.

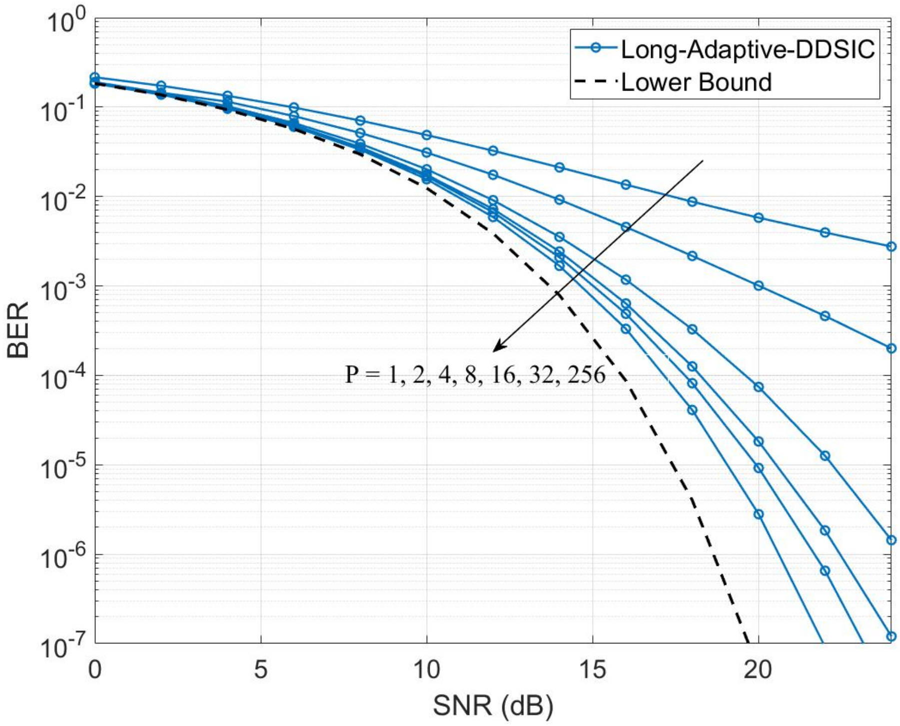

Figure 4.7: Derived lower bound and BER performances of ATPC-aided DDSIC adopting different multipath numbers. The curves from right to left correspond to $P = 1, 2, 4, 8, 16, 32, 256$.

This gap is considered an acceptable level of deviation.

In the second extreme case, the BER performance trend is observed concerning the maximum diversity order by keeping $P = M$ and gradually increasing K_{max}. The slopes of the BER curves represent the diversity order when the SNR increases towards infinity. Since $P = M$ is fixed, all elements in the channel matrix are independent and random. The various BER curves recorded for different K_{max} and the infinite-Doppler BER curve derived for the low SNR region are shown in Figure 4.8. As mentioned in Section 4.4.1, under the threshold of $K_{max} = 8$, the Doppler effects are regarded as completely eliminated by ATPC. In this case, the infinite-Doppler curve can represent the upper bound of the BER performance. In the high SNR region, observe from Figure 4.9 that the slope of the infinite-Doppler curve is the steepest among all. This is close to the theoretical BER curve for $K_{max} = 32$. Generally, it can be concluded that the larger K_{max}, the higher the diversity order. However, note that the results for $K_{max} = 1$ in Figure 4.9 are special, because the slope has not stabilised as the selected SNR region has not been extended to infinity. When SNR approaches infinity, the

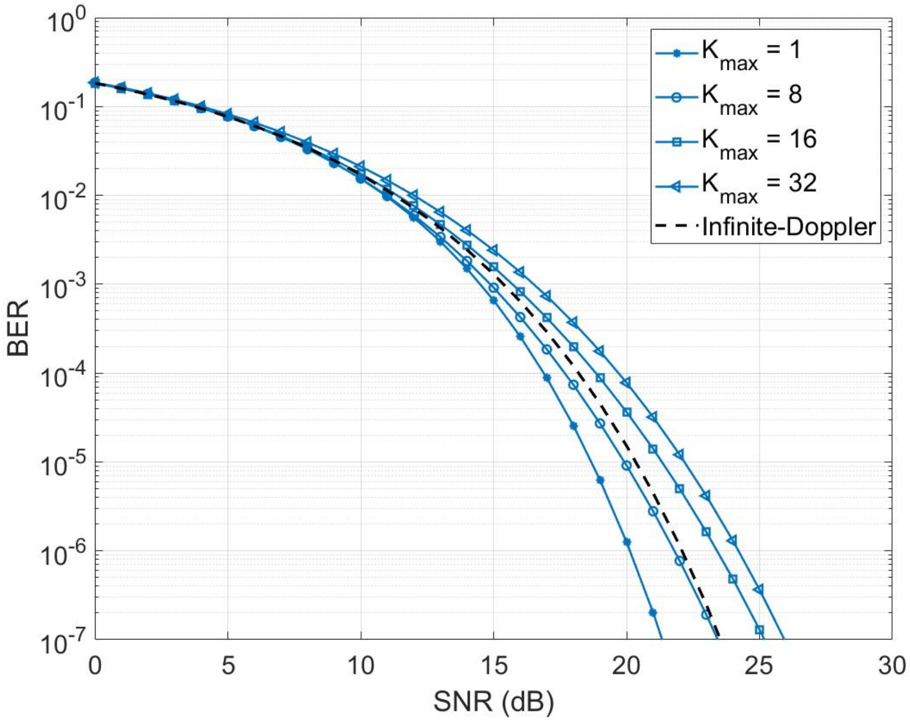

Figure 4.8: BER comparison between derived infinite-Doppler curve and theoretical curves under different maximum Doppler frequencies with $P = M$.

curve corresponding to $K_{max} = 1$ does not have a steeper slope compared to the other curves. Consequently, the derived infinite-Doppler BER curve has the highest diversity order, which demonstrates the accuracy of the derived infinite-Doppler BER expression.

4.4.4 Comparison with Existing Schemes and Combination with Channel Coding

To evaluate the performance benefits brought by ATPC rather than the theoretical expressions, the BER performances for the proposed scheme with the BCJR-turbo detector and truncated VA detector are compared. In particular, QPSK mapping and OTFS modulation are employed. Additionally, LDPC channel coding is applied to improve the robustness of data recovery. For simulation parameters, the truncated ISI length for the VA detector is set to 4, and the code rates for both turbo and LDPC coding are fixed at 0.75.

The BER comparisons under both LOS and NLOS channels are shown in Figures 4.10 and 4.11, respectively. For the LOS channel, the conventional DDSIC scheme (without ATPC) strug-

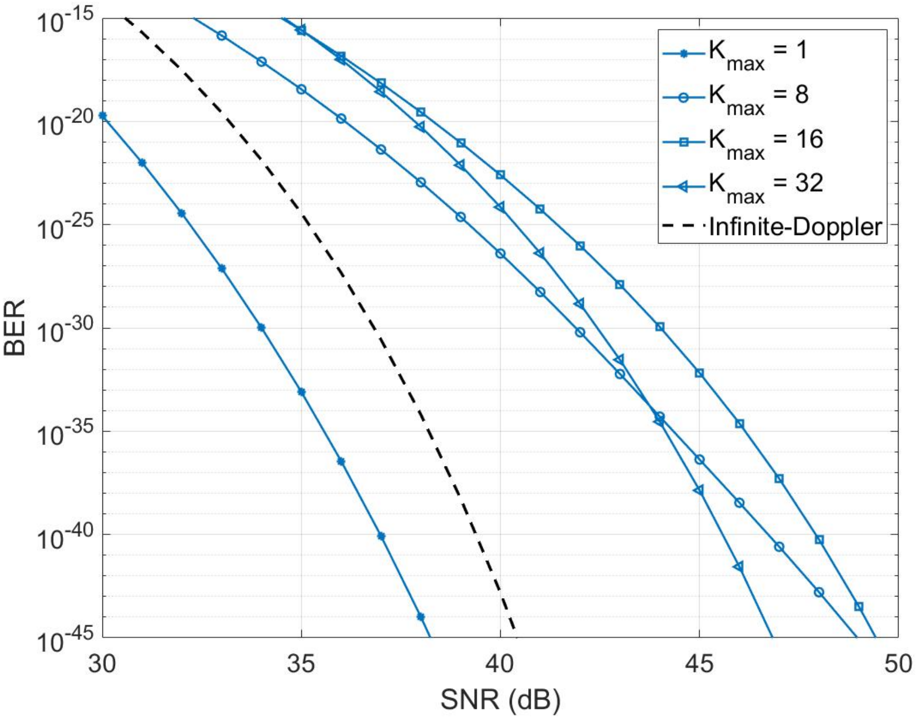

Figure 4.9: BER comparison between derived infinite-Doppler curve and theoretical curves under different maximum Doppler frequencies in high SNR region.

gles to achieve competitive BER performance, especially at higher SNRs. On the other hand, ATPC-aided DDSIC consistently demonstrates lower BER values compared to the truncated VA detector for SNRs above 8 dB. While the BCJR-turbo detector shows better performance with ATPC in the low SNR region, it reaches an error floor beyond an SNR of 16 dB, which is a limitation corresponding to turbo coding. Notably, the LDPC-coded scheme provides a significant improvement, surpassing the ATPC-aided DDSIC without channel coding by approximately 6 dB at a target BER of 10^{-4}. Furthermore, the LDPC-coded and ATPC-aided DDSIC outperforms the ATPC-aided BCJR for SNRs beyond 16 dB.

In NLOS channels, the conventional DDSIC loses effectiveness and ATPC-aided truncated VA performs poorly, whereas both the ATPC-aided DDSIC and BCJR show resilience. However, the ATPC-aided BCJR encounters an error floor beyond an SNR of 15 dB, resulting in a stable BER of 9×10^{-5}. In contrast, the ATPC-aided DDSIC with LDPC coding not only overcomes this limitation but also surpasses the BCJR scheme beyond an SNR of 16 dB. Moreover, for the target BER of 5×10^{-4}, the LDPC-coded ATPC-aided DDSIC provides an additional gain

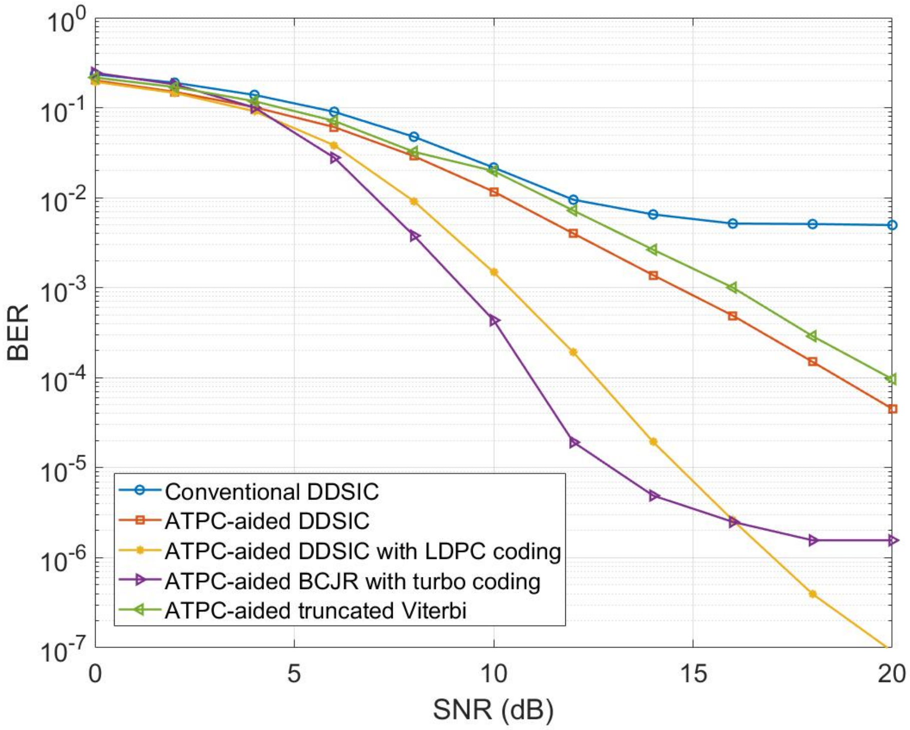

Figure 4.10: BER performance of various data recovery schemes under LOS channel.

of about 4.8 dB compared to the uncoded ATPC-aided DDSIC.

4.5 Conclusions

In this chapter, the ATPC method is integrated into the FTN system to address the challenges in fast-fading channels. Leveraging a feedback-based mechanism, ATPC effectively transforms a fast-fading channel into its slow-fading equivalent, a critical enhancement for the success of the DDSIC algorithm. The robustness of the proposed scheme is validated through a comprehensive analysis of BER performance. Furthermore, two closed-form BER expressions are derived for extreme channel conditions, serving as both theoretical benchmarks and practical tools for evaluating FTN signalling performance in fast-fading environments. Simulation results confirm the feasibility of the adaptive FTN scheme in dynamic fading scenarios. While the results are promising, future work could explore replacing the direct feedback of the $\mathbf{Q}$ matrix with a codebook-based feedback mechanism. This modification would reduce feedback overhead, enhancing the efficiency and practicality of the adaptive FTN system for real-world applications.

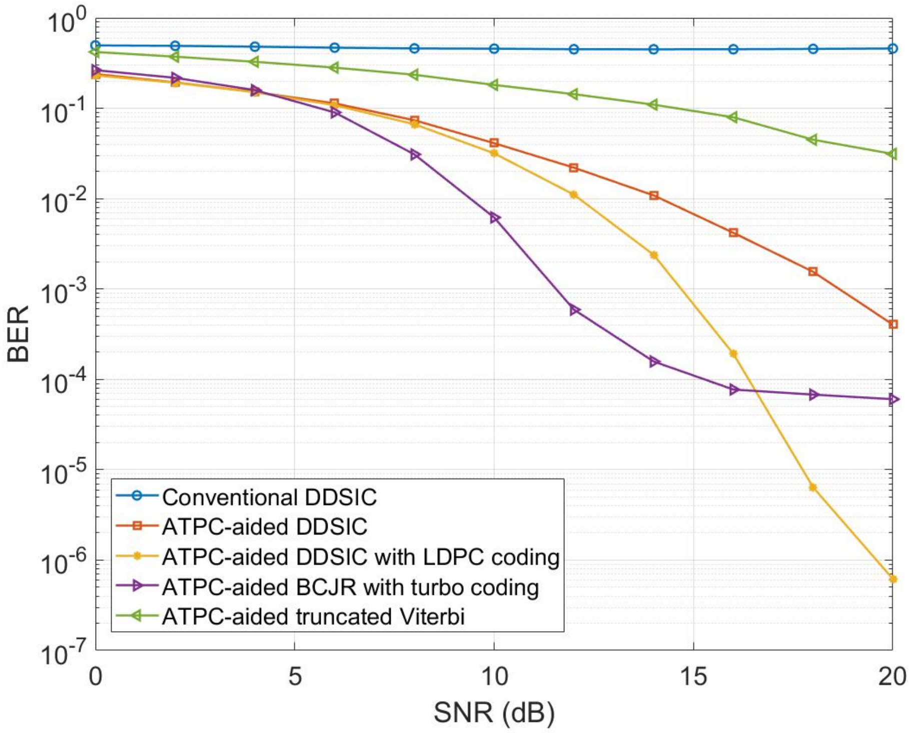

Figure 4.11: BER performance of various data recovery schemes under NLOS channel.

4.6 Appendix A

Based on Eqs. (4.6) and (4.9), $\mathbf{P}$ can be further expanded as

$$\begin{aligned}\mathbf{P} &= \mathbf{V}^{\mathbf{H}}\mathbf{F}_{MN}^{\mathbf{H}}\mathbf{E}_{\nu}\mathbf{H}_{\nu}\mathbf{F}_{MN}\mathbf{V} \\ &= \mathbf{V}^{\mathbf{H}}\mathbf{F}_{MN}^{\mathbf{H}}\mathbf{H}_{\nu}^{\mathbf{H}}(\mathbf{H}_{\nu}\mathbf{H}_{\nu}^{\mathbf{H}} + \frac{1}{\gamma_{in}}\mathbf{I}_{MN})^{-1}\mathbf{H}_{\nu}\mathbf{F}_{MN}\mathbf{V} \\ &= (\mathbf{I}_{MN} + \frac{1}{\gamma_{in}}(\mathbf{V}^{\mathbf{H}}\mathbf{F}_{MN}^{\mathbf{H}}\mathbf{H}_{\nu}^{\mathbf{H}}\mathbf{H}_{\nu}\mathbf{F}_{MN}\mathbf{V})^{-1})^{-1}.\end{aligned} \tag{4.28}$$

Given $\mathbf{U} = \mathbf{V}^{\mathbf{H}}\mathbf{F}_{MN}^{\mathbf{H}}\mathbf{Q}$, this equation can be simplified as

$$\begin{aligned}\mathbf{P} &= (\mathbf{I}_{MN} + \frac{1}{\gamma_{in}}\mathbf{U}\boldsymbol{\Psi}^{-\mathbf{1}}\mathbf{U}^{\mathbf{H}})^{-1} \\ &= \mathbf{I}_{MN} - \mathbf{U}\mathrm{diag}\left\{\frac{1}{\gamma_{in}\lambda_i + 1}\right\}\mathbf{U}^{\mathbf{H}}.\end{aligned} \tag{4.29}$$

4.7 Appendix B

From Eq. (4.11), the weighting coefficient p_0 can be expressed as

$$p_0 = \frac{1}{MN}\mathrm{Tr}\left\{\mathbf{P}\right\} = \frac{1}{MN}\sum_{i=0}^{MN-1}\frac{\gamma_{in}\lambda_i}{\gamma_{in}\lambda_i + 1}. \tag{4.30}$$

In order to derive the power of the recovered signal, $\mathbf{PP^H}$ is first derived from Eq. (4.11) as

$$\mathbf{PP^H} = \mathbf{F}_{MN}^{\mathbf{H}} \mathrm{diag}\left\{ (\frac{\gamma_{in}\lambda_i}{\gamma_{in}\lambda_i + 1})^2 \right\} \mathbf{F}_{MN}. \tag{4.31}$$

The covariance matrix of $\mathbf{y}$ is expressed as

$$\begin{aligned}
\mathbb{E}[\mathbf{yy^H}] &= \mathbb{E}[(\mathbf{Ps} + \mathbf{Gw})(\mathbf{Ps} + \mathbf{Gw})^{\mathbf{H}}] \\
&= \mathbf{P}\mathbb{E}[\mathbf{ss^H}]\mathbf{P^H} + \mathbf{G}\mathbb{E}[\mathbf{ww^H}]\mathbf{G^H} \\
&= \sigma_s^2 \mathbf{PP^H} + \sigma_w^2 \mathbf{GG^H} \\
&= \sigma_s^2 (\mathbf{PP^H} + \frac{1}{\gamma_{in}} \mathbf{GG^H}) \\
&= \sigma_s^2 (\mathbf{V^H F}_{MN}^{\mathbf{H}} \mathbf{E}_\nu \mathbf{H}_\nu \mathbf{H}_\nu^{\mathbf{H}} \mathbf{E}_\nu^{\mathbf{H}} \mathbf{F}_{MN} \mathbf{V} + \\
&\frac{1}{\gamma_{in}} \mathbf{V^H F}_{MN}^{\mathbf{H}} \mathbf{E}_\nu \mathbf{E}_\nu^{\mathbf{H}} \mathbf{F}_{MN} \mathbf{V}) \\
&= \sigma_s^2 \mathbf{V^H F}_{MN}^{\mathbf{H}} \mathbf{E}_\nu (\mathbf{H}_\nu \mathbf{H}_\nu^{\mathbf{H}} + \frac{1}{\gamma_{in}} \mathbf{I}_{MN}) \mathbf{E}_\nu^{\mathbf{H}} \mathbf{F}_{MN} \mathbf{V} \\
&= \sigma_s^2 \mathbf{V^H F}_{MN}^{\mathbf{H}} \mathbf{E}_\nu^{\mathbf{H}} \mathbf{H}_\nu^{\mathbf{H}} \mathbf{F}_{MN} \mathbf{V} \\
&= \sigma_s^2 \mathbf{P^H}.
\end{aligned} \tag{4.32}$$

Therefore, the expression of Eq. (4.20) can be obtained as

$$\begin{aligned}
\gamma_0 &= \frac{\text{Power}\{\text{desired signal}\}}{\text{Power}\{\text{noise}\}} \\
&= \frac{\frac{1}{MN}\mathrm{Tr}\left\{\mathbb{E}[p_0 \mathbf{s}(p_0 \mathbf{s})^{\mathbf{H}}]\right\}}{\frac{1}{MN}\mathrm{Tr}\left\{\mathbb{E}[\mathbf{yy^H}]\right\} - \frac{1}{MN}\mathrm{Tr}\left\{\mathbb{E}[\mathbf{Ps}(\mathbf{Ps})^{\mathbf{H}}]\right\}} \\
&= \frac{\sigma_s^2 |p_0|^2}{\frac{1}{MN}\mathrm{Tr}\left\{\sigma_s^2 \mathbf{P^H}\right\} - \frac{1}{MN}\mathrm{Tr}\left\{\sigma_s^2 \mathbf{PP^H}\right\}} \\
&= \frac{1}{MN} \frac{(\sum_{i=0}^{MN-1} \frac{\gamma_{in}\lambda_i}{\gamma_{in}\lambda_i+1})^2}{\sum_{i=0}^{MN-1} \frac{\gamma_{in}\lambda_i}{\gamma_{in}\lambda_i+1} - \sum_{i=0}^{MN-1} (\frac{\gamma_{in}\lambda_i}{\gamma_{in}\lambda_i+1})^2} \\
&= \frac{1}{MN} \frac{(\sum_{i=0}^{MN-1} \frac{\gamma_{in}\lambda_i}{\gamma_{in}\lambda_i+1})^2}{\sum_{i=0}^{MN-1} \frac{\gamma_{in}\lambda_i}{(\gamma_{in}\lambda_i+1)^2}}.
\end{aligned} \tag{4.33}$$

Chapter 5

Joint ISI and IQI Cancellation in FTN Systems

In this chapter, the practical issue of IQI, caused by RF hardware impairments, is addressed. To tackle this challenge, image signals are incorporated into the analysis, and the existing FTN signal model is extended from a one-dimensional formulation to an extended-dimension framework. Building on this enhanced signal model, the DDSIC algorithm is further refined to jointly mitigate ISI and IQI. Additionally, theoretical BER expressions are derived for each iteration of the DDSIC algorithm, along with a lower bound for the system's BER performance. Simulation results demonstrate that the improved DDSIC algorithm outperforms several state-of-the-art methods in both AWGN and multipath fading channels. The accuracy of the derived theoretical BER expressions is confirmed through these simulations, validating their utility as performance benchmarks. Furthermore, the robustness of the DDSIC scheme is highlighted by its consistent effectiveness across diverse ISI and IQI scenarios, underscoring its reliability in challenging and dynamic communication environments.

5.1 System and Signal Models

In this section, a broadband wireless system is established with a direct conversion architecture. Baseband signals are modulated by FTN signalling and up-converted to RF ones, and then down-converted to baseband at the receiver side. Frequency-dependent IQI is considered at

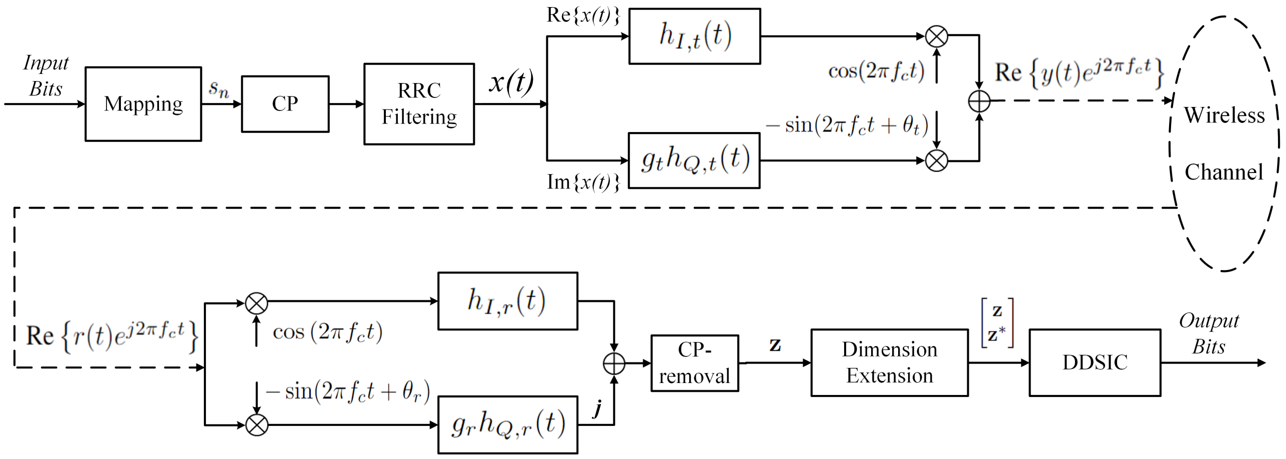

Figure 5.1: Block diagram of the proposed FTN system with I/Q imbalance.

both the transmitter and receiver sides.

The block diagram of the IQI-aware FTN system is presented in Figure 5.1. Input bits are first mapped into QAM symbols and then added by a CP to the head of each frame. Next, FTN transmitter symbols at an interval of αT are generated after the RRC filtering (characterised by a roll-off factor of β and a 3 dB cut-off bandwidth of $1/T$), which can be expressed as

$$x(t)=\sum_{n=0}^{N-1} s_n u(t-n\alpha T), \tag{5.1}$$

where s_n represents the n-th data symbol with an average power of σ_s^2, $(n=0,1,2,...,N-1)$, N is the number of symbols in each frame, $u(t)$ is the RRC shaping pulse with unit energy.

In the process of up-conversion, FTN signals are first separated into I and Q branches. The real and imaginary components are denoted as $x_I(t)$ and $x_Q(t)$, respectively, satisfying $x(t)=x_I(t)+jx_Q(t)$. Next, symbols in the I-branch pass through a reconstruction low pass filter (LPF) denoted as $h_{I,t}(t)$, whereas those in the Q-branch pass through a reconstruction LPF denoted as $h_{Q,t}(t)$ with an amplitude mismatch coefficient g_t and a phase mismatch θ_t. After being converted to carrier frequency f_c, the transmitted RF signal can be expressed as $\mathrm{Re}\{y(t)e^{j2\pi f_c t}\}$ where $y(t)$ is lowpass equivalent of the up-converted signal. The FD representation of $y(t)$ is given by

$$Y(f)=U_t(f)X(f)+V_t(f)X^*(-f), \tag{5.2}$$

where $X(f)$ is the FD representation of $x(t)$. According to [123], the frequency response components $U_t(f)$ and $V_t(f)$ are considered as part of the overall transmission channel frequency response, represented by

$$U_t(f) = \frac{1}{2}(H_{I,t}(f) + g_t H_{Q,t}(f)e^{j\theta_t}) \tag{5.3}$$

and

$$V_t(f) = \frac{1}{2}(H_{I,t}(f) - g_t H_{Q,t}(f)e^{j\theta_t}), \tag{5.4}$$

respectively, where $H_{I,t}(f)$ and $H_{Q,t}(f)$ represent the Fourier transforms of $h_{I,t}(t)$ and $h_{Q,t}(t)$, respectively. In the discrete domain, the frequency variable f can be expressed as $n/(N\alpha T)$ at the n-th frequency bin, while $-f$ corresponds to the frequency bin $(N-n)/(N\alpha T)$. For simplicity, f and $-f$ are used throughout this chapter without further differentiation.

After being transmitted through a zero mean AWGN wireless channel, the received signal $\mathrm{Re}\{r(t)e^{j2\pi f_c t}\}$ is down-converted to baseband and filtered by anti-aliasing LPFs $h_{I.r}(t)$ and $h_{Q,r}(t)$. Similar to the up-converter, there is an amplitude mismatch g_r and a phase mismatch θ_r presented in the LPF of Q-branch. The CP-removed lowpass equivalent signal $r(t)$ can be expressed as

$$r(t) = \sum_{n=0}^{N-1} s_n g(t - n\alpha T) + w(t), \tag{5.5}$$

where $g(t) = \int_{-\infty}^{\infty} h(\tau)u(t-\tau)\,d\tau$, and $w(t)$ is the zero mean AWGN with variance ${\sigma_w}^2$. Denoting $R(f)$ as the FD representation of $r(t)$, the FD down-converted signal $Z(f)$ can be expressed as

$$Z(f) = U_r(f)R(f) + V_r(f)R^*(-f). \tag{5.6}$$

The frequency response components $U_r(f)$ and $V_r(f)$ are considered as part of the transmission channel frequency response, represented by

$$U_r(f) = \frac{1}{2}(H_{I,r}(f) + g_r H_{Q,r}(f)e^{-j\theta_r}), \tag{5.7}$$

and

$$V_r(f) = \frac{1}{2}(H_{I,r}(f) - g_r H_{Q,r}(f)e^{j\theta_r}), \tag{5.8}$$

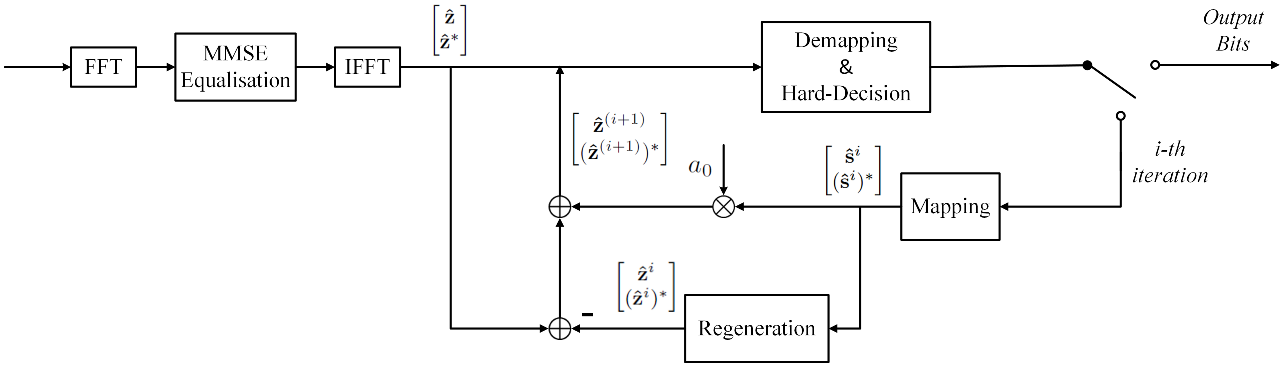

Figure 5.2: Diagram of the proposed joint interference cancellation algorithm.

respectively, with $H_{I,r}(f)$ and $H_{Q,r}(f)$ being the Fourier transforms of $h_{I,r}(t)$ and $h_{Q,r}(t)$, respectively.

It is highlighted that the employed LPFs can be accurately modeled and estimated applying various existing methods, such as training-sequence-aided estimation in [124] and expanded memory polynomial (EMP) parameter estimation in [53]. Built upon this accurate modeling, the IQI parameters are all assumed to be perfectly obtained at the receiver.

5.2 Joint Interference Cancellation Algorithm

This section presents the improved DDSIC algorithm designed for joint cancellation of both ISI and IQI. The block diagram of the improved DDSIC algorithm is presented in Figure 5.2. The process begins with dimension extension, allowing for the representation of the impact of image signals. Following this, extended-dimension FD-MMSE equalisation and finally, decision-directed iterative interference cancellation are applied.

5.2.1 Dimension Extension

After down-conversion and the removal of the CP, dimension extension is performed to facilitate joint interference cancellation. Specifically, the original signal vector, the equivalent channel matrix, and the noise vector are each combined with their conjugate counterparts. Defining the extended-dimension transmitted signal vector as $\begin{bmatrix}\mathbf{s}\\ \mathbf{s}^*\end{bmatrix} = [s_0, s_1, ..., s_{N-1}, s_0^*, s_1^*, ..., s_{N-1}^*]^{\mathbf{T}}$, the down-converted signal vector can be expressed as

$$\begin{aligned}\begin{bmatrix}\mathbf{z}\\ \mathbf{z}^*\end{bmatrix} &= [z_0, z_1, ..., z_{N-1}, z_0^*, z_1^*, ..., z_{N-1}^*]^{\mathbf{T}}\\ &= \begin{bmatrix}\mathbf{F}^{\mathbf{H}} & O\\ O & \mathbf{F}^{\mathbf{H}}\end{bmatrix}\mathbf{G}\begin{bmatrix}\mathbf{F} & O\\ O & \mathbf{F}\end{bmatrix}\begin{bmatrix}\mathbf{s}\\ \mathbf{s}^*\end{bmatrix}+\begin{bmatrix}\mathbf{w}\\ \mathbf{w}^*\end{bmatrix}.\end{aligned} \tag{5.9}$$

In Eq. (5.9), $\begin{bmatrix}\mathbf{w}\\ \mathbf{w}^*\end{bmatrix}$ denotes the extended noise vector where $\mathbf{w}$ represents a zero-mean AWGN vector, consisting of independent elements each with a variance of σ_w^2, and $\mathbf{w}^*$ is its conjugate counterpart. $\mathbf{G}$ is the equivalent channel matrix of order $2N \times 2N$ which can be derived from Eqs. (5.2) and (5.6) as

$$\mathbf{G} = \begin{bmatrix}\mathbf{U_f} & \mathbf{V_f}\\ \mathbf{V}^*_{-\mathbf{f}} & \mathbf{U}^*_{-\mathbf{f}}\end{bmatrix}, \tag{5.10}$$

where $\mathbf{U_f}$, $\mathbf{V_f}$, $\mathbf{U_{-f}}$, $\mathbf{V_{-f}}$ are diagonal matrices with $U_f[k]$, $V_f[k]$, $U_{-f}[k]$, $V_{-f}[k]$ being the k-th diagonal elements for $k = 0, 1, ..., N-1$, respectively. Let $\Delta f = 1/(N\alpha T)$ be the frequency resolution, the diagonal elements are expressed as

$$\begin{aligned}U_f[k] &= U_t(k\Delta f)H(k\Delta f)U_r(k\Delta f)\\ &\qquad + V_t^*(-k\Delta f)H^*(-k\Delta f)V_r(k\Delta f),\\ V_f[k] &= V_t(k\Delta f)H(k\Delta f)U_r(k\Delta f)\\ &\qquad + U_t^*(-k\Delta f)H^*(-k\Delta f)V_r(k\Delta f),\\ U_{-f}[k] &= U_t(-k\Delta f)H(-k\Delta f)U_r(-k\Delta f)\\ &\qquad + V_t^*(k\Delta f)H^*(k\Delta f)V_r(-k\Delta f),\\ V_{-f}[k] &= V_t(-k\Delta f)H(-k\Delta f)U_r(-k\Delta f)\\ &\qquad + U_t^*(k\Delta f)H^*(k\Delta f)V_r(-k\Delta f),\end{aligned} \tag{5.11}$$

where $H(f)$ is the wireless channel frequency response including the RRC filter.

Note that in Eq. (5.9), extending the vector dimension is essential to account for the impact of image signals and subsequent analysis of the received signals. Although the effective signal and noise vectors each retain a length of N, their extended conjugate counterparts are inherently dependent on the original versions.

5.2.2 Stage I: FD-MMSE Equalisation

The extended-dimension FD-MMSE equalisation matrix is given by

$$\mathbf{E} = \mathbf{G^H}(\mathbf{G}\mathbf{G^H} + \frac{1}{\gamma_{in}}\mathbf{I}_{2N})^{-1}, \tag{5.12}$$

where γ_{in} is the input SNR of the MMSE equaliser.

Then, the TD signals after the initial estimation can be expressed as

$$\begin{aligned}
\begin{bmatrix} \hat{\mathbf{z}} \\ \hat{\mathbf{z}}^* \end{bmatrix} &= \begin{bmatrix} \mathbf{F^H} & O \\ O & \mathbf{F^H} \end{bmatrix} \mathbf{E} \begin{bmatrix} \mathbf{F} & O \\ O & \mathbf{F} \end{bmatrix} \begin{bmatrix} \mathbf{z} \\ \mathbf{z}^* \end{bmatrix} \\
&= \begin{bmatrix} \mathbf{F^H} & O \\ O & \mathbf{F^H} \end{bmatrix} \begin{bmatrix} \mathbf{A_f} & \mathbf{B_f} \\ \mathbf{B^*_{-f}} & \mathbf{A^*_{-f}} \end{bmatrix} \begin{bmatrix} \mathbf{F} & O \\ O & \mathbf{F} \end{bmatrix} \begin{bmatrix} \mathbf{s} \\ \mathbf{s}^* \end{bmatrix} \\
&\qquad + \begin{bmatrix} \mathbf{F^H} & O \\ O & \mathbf{F^H} \end{bmatrix} \mathbf{E} \begin{bmatrix} \mathbf{F} & O \\ O & \mathbf{F} \end{bmatrix} \begin{bmatrix} \mathbf{w} \\ \mathbf{w}^* \end{bmatrix} \\
&= \begin{bmatrix} \mathbf{F^H}\mathbf{A_f}\mathbf{F} & \mathbf{F^H}\mathbf{B_f}\mathbf{F} \\ \mathbf{F^H}\mathbf{B^*_{-f}}\mathbf{F} & \mathbf{F^H}\mathbf{A^*_{-f}}\mathbf{F} \end{bmatrix} \begin{bmatrix} \mathbf{s} \\ \mathbf{s}^* \end{bmatrix} \\
&\qquad + \begin{bmatrix} \mathbf{F^H} & O \\ O & \mathbf{F^H} \end{bmatrix} \mathbf{E} \begin{bmatrix} \mathbf{F} & O \\ O & \mathbf{F} \end{bmatrix} \begin{bmatrix} \mathbf{w} \\ \mathbf{w}^* \end{bmatrix},
\end{aligned} \tag{5.13}$$

where the FFT and IFFT matrices are designed for the extended-dimension computation and thus comprise zero matrices of order N on the upper right and the lower left corner. $\mathbf{A_f}$ and $\mathbf{B_f}$ are both diagonal matrices with $A[k]$ and $B[k]$ being the k-th diagonal elements. $A[k]$ and $B[k]$ are derived from Eqs. (5.9), (5.10) and (5.12) as

$$\begin{aligned}A[k] = &\Big[U_f[k]U_f^*[k]U_{-f}[k]U_{-f}^*[k] + V_f[k]V_f^*[k]V_{-f}[k]V_{-f}^*[k] - U_f[k]U_{-f}^*[k]V_f^*[k]V_{-f}[k] \\ &- U_f^*[k]U_{-f}[k]V_f[k]V_{-f}^*[k] + \frac{1}{\gamma_{in}}(U_f[k]U_f^*[k] + V_{-f}[k]V_{-f}^*[k])\Big] \\ &\div \Big[(U_f[k]U_f^*[k] + V_f[k]V_f^*[k] + \frac{1}{\gamma_{in}})(U_{-f}[k]U_{-f}^*[k] + V_{-f}[k]V_{-f}^*[k] + \frac{1}{\gamma_{in}}) \\ &- (U_f[k]V_{-f}[k] + U_{-f}[k]V_f[k])(U_f^*[k]V_{-f}^*[k] + U_{-f}^*[k]V_f^*[k])\Big], \qquad (5.14) \\ B[k] = &\frac{1}{\gamma_{in}}(U_f^*[k]V_f[k] + U_{-f}^*[k]V_{-f}[k]) \div \Big[(U_f[k]U_f^*[k] + V_f[k]V_f^*[k] + \frac{1}{\gamma_{in}}) \\ &(U_{-f}[k]U_{-f}^*[k] + V_{-f}[k]V_{-f}^*[k] + \frac{1}{\gamma_{in}}) - (U_f[k]V_{-f}[k] + U_{-f}[k]V_f[k]) \\ &(U_f^*[k]V_{-f}^*[k] + U_{-f}^*[k]V_f^*[k])\Big].\end{aligned}$$

For simplicity, the definitions $\mathbf{P_A} = \mathbf{F^H A_f F}$, $\mathbf{P_B} = \mathbf{F^H B_f F}$, $\mathbf{P_{-A}} = \mathbf{F^H A_{-f} F}$, and $\mathbf{P_{-B}} = \mathbf{F^H B_{-f} F}$ are used, and $A_-[k]$ and $B_-[k]$ denote the k-th diagonal elements of diagonal matrices $\mathbf{A_{-f}}$, $\mathbf{B_{-f}}$, respectively. Note that $\mathbf{P_A}, \mathbf{P_B}, \mathbf{P_{-A}}, \mathbf{P_{-B}}$ are all Hermitian matrices, their diagonal elements can be directly used to calculate the trace of the respective matrices, which will be used in evaluating the BER performance.

5.2.3 Stage II: Decision-Directed Iterative Equalisation

The extended-dimension equalised signal in stage I can be decomposed as

$$\begin{aligned}\begin{bmatrix}\hat{\mathbf{z}} \\ \hat{\mathbf{z}}^*\end{bmatrix} &= \begin{bmatrix}\mathbf{P_A} & \mathbf{P_B} \\ \mathbf{P_{-B}^*} & \mathbf{P_{-A}^*}\end{bmatrix}\begin{bmatrix}\mathbf{s} \\ \mathbf{s}^*\end{bmatrix} + \begin{bmatrix}\mathbf{F^H} & O \\ O & \mathbf{F^H}\end{bmatrix}\mathbf{E}\begin{bmatrix}\mathbf{F} & O \\ O & \mathbf{F}\end{bmatrix}\begin{bmatrix}\mathbf{w} \\ \mathbf{w}^*\end{bmatrix} \\ &= \begin{bmatrix}\mathbf{P_A s} + \mathbf{P_B s}^* \\ \mathbf{P_{-B}^* s} + \mathbf{P_{-A}^* s}^*\end{bmatrix} + \begin{bmatrix}\mathbf{F^H} & O \\ O & \mathbf{F^H}\end{bmatrix}\mathbf{E}\begin{bmatrix}\mathbf{F} & O \\ O & \mathbf{F}\end{bmatrix}\begin{bmatrix}\mathbf{w} \\ \mathbf{w}^*\end{bmatrix} \\ &= a_0\begin{bmatrix}\mathbf{s} \\ \mathbf{s}^*\end{bmatrix} + \begin{bmatrix}(\mathbf{P_A} - a_0\mathbf{I}_N)\mathbf{s} + \mathbf{P_B s}^* \\ \mathbf{P_{-B}^* s} + (\mathbf{P_{-A}^*} - a_0\mathbf{I}_N)\mathbf{s}^*\end{bmatrix} \\ &\quad + \begin{bmatrix}\mathbf{F^H} & O \\ O & \mathbf{F^H}\end{bmatrix}\mathbf{E}\begin{bmatrix}\mathbf{F} & O \\ O & \mathbf{F}\end{bmatrix}\begin{bmatrix}\mathbf{w} \\ \mathbf{w}^*\end{bmatrix}, \qquad (5.15)\end{aligned}$$

where the three terms represent the desired signal, joint interference and noise respectively. a_0 is the scaling factor caused by the channel response expressed as

$$a_0 = \frac{1}{N}\mathrm{Tr}\left\{\mathbf{P_A}\right\} = \frac{1}{N}\sum_{k=0}^{N-1} A[k]. \qquad (5.16)$$

Note that, from Eq. (5.14), a_0 is real-valued.

In order to remove the remained ISI and IQI in the first stage, the equalised data symbols are reprocessed by passing through a noise-free extended-dimension channel to regenerate the MMSE equalised signal. The regeneration process can be formulated in a widely linear system expressed as

$$\begin{bmatrix} \hat{\mathbf{z}}^i \\ (\hat{\mathbf{z}}^i)^* \end{bmatrix} = \begin{bmatrix} \mathbf{P}_{\mathbf{A}} & \mathbf{P}_{\mathbf{B}} \\ \mathbf{P}^*_{-\mathbf{B}} & \mathbf{P}^*_{-\mathbf{A}} \end{bmatrix} \begin{bmatrix} \hat{\mathbf{s}}^i \\ (\hat{\mathbf{s}}^i)^* \end{bmatrix}, \tag{5.17}$$

where $(\cdot)^i$ denotes the symbol vector of the i-th iteration and $\begin{bmatrix} \hat{\mathbf{s}}^i \\ (\hat{\mathbf{s}}^i)^* \end{bmatrix}$ represents the hard-decided symbol vector. Note that the entire regeneration can be performed in FD through DFT/IDFT.

Assuming that the total interference has been sufficiently mitigated in the last iteration, i.e., $\begin{bmatrix} \mathbf{s} \\ \mathbf{s}^* \end{bmatrix} = \begin{bmatrix} \hat{\mathbf{s}}^i \\ (\hat{\mathbf{s}}^i)^* \end{bmatrix}$, the difference between the originally equalised signal (without interference cancellation) and the regenerated signal represents the joint interference and noise components from the previous iteration, which can be expressed as

$$\begin{bmatrix} \hat{\mathbf{z}} \\ \hat{\mathbf{z}}^* \end{bmatrix} - \begin{bmatrix} \hat{\mathbf{z}}^i \\ (\hat{\mathbf{z}}^i)^* \end{bmatrix} = \begin{bmatrix} \mathbf{F}^{\mathbf{H}} & O \\ O & \mathbf{F}^{\mathbf{H}} \end{bmatrix} \mathbf{E} \begin{bmatrix} \mathbf{F} & O \\ O & \mathbf{F} \end{bmatrix} \begin{bmatrix} \mathbf{w} \\ \mathbf{w}^* \end{bmatrix}. \tag{5.18}$$

By scaling the hard-decided data symbols to compensate for the equivalent channel response and adding them back to the difference signal, more accurate equalised signals with reduced interference are obtained. With further suppression of both ISI and IQI, the symbols, with less interference for decision in the next iteration can be expressed as

$$\begin{aligned} \begin{bmatrix} \hat{\mathbf{z}}^{(i+1)} \\ (\hat{\mathbf{z}}^{(i+1)})^* \end{bmatrix} &= a_0 \begin{bmatrix} \hat{\mathbf{s}}^i \\ (\hat{\mathbf{s}}^i)^* \end{bmatrix} + \begin{bmatrix} \hat{\mathbf{z}} \\ \hat{\mathbf{z}}^* \end{bmatrix} - \begin{bmatrix} \hat{\mathbf{z}}^i \\ (\hat{\mathbf{z}}^i)^* \end{bmatrix} \\ &= a_0 \begin{bmatrix} \hat{\mathbf{s}}^i \\ (\hat{\mathbf{s}}^i)^* \end{bmatrix} + \begin{bmatrix} \mathbf{P}_{\mathbf{A}} & \mathbf{P}_{\mathbf{B}} \\ \mathbf{P}^*_{-\mathbf{B}} & \mathbf{P}^*_{-\mathbf{A}} \end{bmatrix} \begin{bmatrix} \mathbf{s} - \hat{\mathbf{s}}^i \\ (\mathbf{s} - \hat{\mathbf{s}}^i)^* \end{bmatrix} \\ &\quad + \begin{bmatrix} \mathbf{F}^{\mathbf{H}} & O \\ O & \mathbf{F}^{\mathbf{H}} \end{bmatrix} \mathbf{E} \begin{bmatrix} \mathbf{F} & O \\ O & \mathbf{F} \end{bmatrix} \begin{bmatrix} \mathbf{w} \\ \mathbf{w}^* \end{bmatrix}. \end{aligned} \tag{5.19}$$

Table 5.1: Complexity Analysis for Various Methods

Methods	Proposed Algorithm (per iteration)	Truncated VA in [56]	M-BCJR algorithm in [67]
Addition/ subtraction	$4N^2 + 4N$	$N^2 m^L$	$2N^2 m^M$
Multiplication/ Division	$4N^2 + 2N$	$4N^2 m^L$	$8N^2 m^M$
Exponentiation/ Logarithm	0	NLm	$2NMm$
Recursion(s)	1	1	3
Required Filter(s)	1	1	3 or 4

This iterative approach ensures that the residual interference is progressively mitigated with each iteration. By repeating the DDSIC for several iterations, the estimated symbols can approach a joint-interference-free condition.

5.2.4 Complexity Analysis for Various Methods

This subsection assesses the computational complexity of the extended-dimension DDSIC algorithm while discussing its practicality and challenges concerning hardware implementation.

Table 5.1 provides a detailed comparison of computational complexity between the proposed DDSIC algorithm, the truncated VA from [56], and the M-BCJR algorithm described in [67]. In the table, a frame containing N symbols and a channel matrix of size $N \times N$ is considered. Here, m denotes the number of possible states per symbol, L represents the memory length in the truncated VA, and M refers to the number of survivors utilised in the M-BCJR algorithm.

While the new DDSIC algorithm involves operating in an extended-dimension form, it still maintains relatively low computational complexity. Specifically, the complexity is only doubled in terms of multiplications/divisions and additions/subtractions compared to the previously proposed algorithm in Section 3.5. The use of FD MMSE equalisation significantly simplifies the linear convolution operations, reducing them to matrix multiplications. For the extended-dimension DDSIC, this entails $4N^2 + 4N$ additions and $4N^2 + 2N$ multiplications, without requiring exponentiation or logarithm operations.

In contrast, the M-BCJR algorithm involves higher computational costs due to its reliance on multiple recursions and filter operations [68], whereas the proposed DDSIC algorithm requires only one recursion and a single MMSE equalisation operation. Furthermore, by processing the entire frame simultaneously, the DDSIC algorithm enhances efficiency compared to conventional symbol-by-symbol processing approaches.

5.3 Performance Analysis

With the aid of dimension extension, the theoretical BER expressions for each DDSIC iteration and a BER lower bound of the proposed IQI-aware FTN system are analysed.

5.3.1 Power Expression of Each Component

For the derivation of output SNR, the power of each component are first derived in Eq. (5.15). Denoting the TD equivalent transfer matrix from $\begin{bmatrix} \mathbf{s} \\ \mathbf{s}^* \end{bmatrix}$ to $\begin{bmatrix} \hat{\mathbf{z}} \\ \hat{\mathbf{z}}^* \end{bmatrix}$ as $\mathbf{P}$, which is given by

$$\mathbf{P} = \begin{bmatrix} \mathbf{P_A} & \mathbf{P_B} \\ \mathbf{P}^*_{-\mathbf{B}} & \mathbf{P}^*_{-\mathbf{A}} \end{bmatrix}, \tag{5.20}$$

the power of the received signal can be derived from the trace of its covariance matrix as

$$
\begin{aligned}
&\text{Power}\Big\{\text{received signal}\Big\}\\
&= \frac{1}{2N}\text{Tr}\Bigg\{\mathbb{E}\Bigg[\begin{bmatrix}\hat{\mathbf{z}}\\ \hat{\mathbf{z}}^*\end{bmatrix}\begin{bmatrix}\hat{\mathbf{z}}\\ \hat{\mathbf{z}}^*\end{bmatrix}^{\mathbf{H}}\Bigg]\Bigg\}\\
&= \frac{1}{2N}\text{Tr}\Bigg\{\mathbf{P}\mathbb{E}\Bigg[\begin{bmatrix}\mathbf{s}\\ \mathbf{s}^*\end{bmatrix}\begin{bmatrix}\mathbf{s}\\ \mathbf{s}^*\end{bmatrix}^{\mathbf{H}}\Bigg]\mathbf{P}^{\mathbf{H}} + \mathbf{E}\mathbb{E}\Bigg[\begin{bmatrix}\mathbf{w}\\ \mathbf{w}^*\end{bmatrix}\begin{bmatrix}\mathbf{w}\\ \mathbf{w}^*\end{bmatrix}^{\mathbf{H}}\Bigg]\mathbf{E}^{\mathbf{H}}\Bigg\}\\
&= \frac{1}{N}\text{Tr}\Big\{\sigma_s^2\mathbf{P}\mathbf{P}^{\mathbf{H}} + \sigma_w^2\mathbf{E}\mathbf{E}^{\mathbf{H}}\Big\}\\
&= \frac{1}{N}\text{Tr}\Big\{\mathbf{P}\mathbf{P}^{\mathbf{H}} + \frac{1}{\gamma_{in}}\mathbf{E}\mathbf{E}^{\mathbf{H}}\Big\}\sigma_s^2\\
&= \frac{1}{N}\text{Tr}\Big\{\mathbf{E}(\mathbf{G}\mathbf{G}^{\mathbf{H}} + \frac{1}{\gamma_{in}}\mathbf{I}_{2N})\mathbf{E}^{\mathbf{H}}\Big\}\sigma_s^2\\
&= \frac{1}{N}\text{Tr}\Big\{\mathbf{P}^{\mathbf{H}}\Big\}\sigma_s^2\\
&= 2a_0\sigma_s^2.
\end{aligned}
\tag{5.21}
$$

In each iteration, the desired signal component is always $a_0\begin{bmatrix}\mathbf{s}\\ \mathbf{s}^*\end{bmatrix}$, thus the power of the desired signal can be expressed as

$$
\begin{aligned}
&\text{Power}\Big\{\text{desired signal}\Big\}\\
&= \frac{1}{2N}\text{Tr}\Bigg\{\mathbb{E}\Bigg[\begin{bmatrix}a_0\mathbf{s}\\ a_0\mathbf{s}^*\end{bmatrix}\begin{bmatrix}a_0\mathbf{s}\\ a_0\mathbf{s}^*\end{bmatrix}^{\mathbf{H}}\Bigg]\Bigg\}\\
&= 2a_0^2\sigma_s^2.
\end{aligned}
\tag{5.22}
$$

To compute the noise power from Eq. (5.13), $\mathbf{P}\mathbf{P}^{\mathbf{H}}$ is expressed in a similar extended-dimension form as

$$
\mathbf{P}\mathbf{P}^{\mathbf{H}} = \begin{bmatrix}\mathbf{A_f}\mathbf{A_f^*} + \mathbf{B_f}\mathbf{B_f^*} & \mathbf{A_f}\mathbf{B_{-f}} + \mathbf{A_{-f}}\mathbf{B_f}\\ \mathbf{A_f^*}\mathbf{B_{-f}^*} + \mathbf{A_{-f}^*}\mathbf{B_f^*} & \mathbf{A_{-f}}\mathbf{A_{-f}^*} + \mathbf{B_{-f}}\mathbf{B_{-f}^*}\end{bmatrix}. \tag{5.23}
$$

Note that the diagonal elements $A_{-}[k]$ and $B_{-}[k]$ satisfy that $A_{-}[k]A_{-}^{*}[k] = |A[k]|^2$ and $B_{-}[k]B_{-}^{*}[k] = |B[k]^2|$. With all these above relationships, the noise power can be expressed as the total received power minus the power corresponding to the $\mathbf{P}\begin{bmatrix}\mathbf{s}\\ \mathbf{s}^*\end{bmatrix}$ component, i.e.,

$$\begin{aligned}
&\text{Power}\Big\{\text{noise}\Big\} \\
&= \frac{1}{2N}\text{Tr}\left\{\mathbb{E}\left[\begin{bmatrix}\hat{\mathbf{z}}\\ \hat{\mathbf{z}}^*\end{bmatrix}\begin{bmatrix}\hat{\mathbf{z}}\\ \hat{\mathbf{z}}^*\end{bmatrix}^{\mathbf{H}} - \mathbf{P}\begin{bmatrix}\mathbf{s}\\ \mathbf{s}^*\end{bmatrix}\left(\mathbf{P}\begin{bmatrix}\mathbf{s}\\ \mathbf{s}^*\end{bmatrix}\right)^{\mathbf{H}}\right]\right\} \\
&= 2a_0\sigma_s^2 - \frac{1}{N}\text{Tr}\Big\{\mathbf{P}\mathbf{P}^{\mathbf{H}}\Big\}\sigma_s^2 \\
&= 2a_0\sigma_s^2 - \frac{2}{N}(\sum_{k=0}^{N-1}|A[k]|^2 + |B[k]|^2)\sigma_s^2. \qquad (5.24)
\end{aligned}$$

5.3.2 Theoretical BER for Stage I of DDSIC

Similar to the analysis in Chapter 3, the output SNR after the initial MMSE equalisation is derived as

$$\begin{aligned}
\gamma_{out}^{(1)} &= \frac{\text{Power}\Big\{\text{desired signal}\Big\}}{\text{Power}\Big\{\text{received signal}\Big\} - \text{Power}\Big\{\text{desired signal}\Big\}} \\
&= \frac{2a_0^2}{2a_0 - 2a_0^2} = \frac{a_0}{1-a_0}. \qquad (5.25)
\end{aligned}$$

Denoting $P_s^{(1)}$ as the symbol error probability of the MMSE equalised signal. For an M-QAM system, it is given by

$$P_s^{(1)} \approx 1 - \left\{1 - 2(1-\frac{1}{\sqrt{M}})Q\left(\sqrt{\frac{3\gamma_{out}^{(1)}}{M-1}}\right)\right\}^2. \qquad (5.26)$$

Therefore, the BER of the first iteration, denoted as $P_b^{(1)}$, can be derived as

$$\begin{aligned} P_b^{(1)} &\approx \frac{1}{\log_2 M} P_s^{(1)} \\ &\approx \frac{1}{\log_2 M} \left\{ 1 - \left[1 - 2(1 - \frac{1}{\sqrt{M}}) Q \left(\sqrt{\frac{3\gamma_{out}^{(1)}}{M-1}} \right) \right]^2 \right\} \\ &= \frac{1}{\log_2 M} \left\{ 1 - \left[1 - 2(1 - \frac{1}{\sqrt{M}}) \right.\right. \\ &\qquad \left.\left. Q \left(\sqrt{\frac{3}{M-1} \cdot \frac{a_0}{1-a_0}} \right) \right]^2 \right\}. \end{aligned} \tag{5.27}$$

5.3.3 Theoretical BER after Each Iteration in Stage II of DDSIC

To derive the output SNR of each iteration in Stage II, the power of residual joint interference should be analysed first. In particular, let $d = \frac{1}{\sqrt{\frac{2}{3}(M-1)}}$ represent the scaling factor for constellation spacing in a normalised M-QAM system and assume that a mis-mapped symbol results in only a one-bit error, the distance between these two constellation points is $2d$. After the hard decision, a mis-mapped symbol introduces ISI equivalent to the distance between two adjacent symbols. Consequently, the residual ISI power is $(4d)^2$ times the original ISI power, weighted by the symbol error rate. On the other hand, the residual IQI power is $(2d)^2$ times the original IQI power, since only the image symbol corresponding to the mis-mapped symbol is incorrectly generated.

The residual ISI-plus-IQI power after the first iteration is derived as

$$\begin{aligned}
\text{ISI-IQI}_{re}^{(1)} =&\left(\frac{4}{\sqrt{\frac{2}{3}(M-1)}}\right)^2 \frac{1}{2N}\text{Tr}\left\{\mathbb{E}\left[\begin{bmatrix}(\mathbf{P_A}-a_0\mathbf{I}_N)\mathbf{s}\\(\mathbf{P}^*_{-\mathbf{A}}-a_0\mathbf{I}_N)\mathbf{s}^*\end{bmatrix}\begin{bmatrix}(\mathbf{P_A}-a_0\mathbf{I}_N)\mathbf{s}\\(\mathbf{P}^*_{-\mathbf{A}}-a_0\mathbf{I}_N)\mathbf{s}^*\end{bmatrix}^{\mathbf{H}}\right]\right\}\\
&+\left(\frac{2}{\sqrt{\frac{2}{3}(M-1)}}\right)^2 \frac{1}{2N}\text{Tr}\left\{\mathbb{E}\left[\begin{bmatrix}\mathbf{P_B}\mathbf{s}^*\\\mathbf{P}^*_{-\mathbf{B}}\mathbf{s}\end{bmatrix}\begin{bmatrix}\mathbf{P_B}\mathbf{s}^*\\\mathbf{P}^*_{-\mathbf{B}}\mathbf{s}\end{bmatrix}^{\mathbf{H}}\right]\right\}\\
=&\left(\frac{4}{\sqrt{\frac{2}{3}(M-1)}}\right)^2 \frac{1}{2N}\text{Tr}\left\{\mathbb{E}\left[\begin{bmatrix}\mathbf{P_A}-a_0\mathbf{I}_N & O\\ O & \mathbf{P}^*_{-\mathbf{A}}-a_0\mathbf{I}_N\end{bmatrix}\begin{bmatrix}\mathbf{s}\\\mathbf{s}^*\end{bmatrix}\right.\right.\\
&\left.\left.\begin{bmatrix}\mathbf{s}\\\mathbf{s}^*\end{bmatrix}^{\mathbf{H}}\begin{bmatrix}\mathbf{P_A}-a_0\mathbf{I}_N & O\\ O & \mathbf{P}^*_{-\mathbf{A}}-a_0\mathbf{I}_N\end{bmatrix}^{\mathbf{H}}\right]\right\}P_s^{(1)}\\
&+\left(\frac{2}{\sqrt{\frac{2}{3}(M-1)}}\right)^2 \frac{1}{2N}\text{Tr}\left\{\mathbb{E}\left[\begin{bmatrix}O & \mathbf{P_B}\\ \mathbf{P}^*_{-\mathbf{B}} & O\end{bmatrix}\begin{bmatrix}\mathbf{s}\\\mathbf{s}^*\end{bmatrix}\begin{bmatrix}\mathbf{s}\\\mathbf{s}^*\end{bmatrix}^{\mathbf{H}}\begin{bmatrix}O & \mathbf{P_B}\\ \mathbf{P}^*_{-\mathbf{B}} & O\end{bmatrix}^{\mathbf{H}}\right]\right\}P_s^{(1)}\\
=&\frac{24}{M-1}\Big[\big(\frac{2}{N}\sum_{k=0}^{N-1}|A[k]|^2+\frac{1}{4}|B[k]|^2\big)-2a_0^2\Big]P_s^{(1)}\sigma_s^2.
\end{aligned}\tag{5.28}$$

Therefore, the output SNR of the second iteration can be computed as

$$\begin{aligned}
\gamma_{out}^{(2)} =& \frac{\text{Power}\Big\{\text{desired signal}\Big\}}{\text{ISI-IQI}_{re}^{(1)}+\text{Power}\Big\{\text{noise}\Big\}}\\
=& \frac{2a_0^2\sigma_s^2}{\text{ISI-IQI}_{re}^{(1)}+2a_0\sigma_s^2-\frac{2\sigma_s^2}{N}(\sum\limits_{k=0}^{N-1}|A[k]|^2+|B[k]|^2)},
\end{aligned}\tag{5.29}$$

and the BER of the second iteration for the M-QAM system is

$$\begin{aligned}
P_b^{(2)} \approx& \frac{1}{\log_2 M}\left\{1-\left[1-2(1-\frac{1}{\sqrt{M}})Q\left(\sqrt{\frac{3}{M-1}}\right.\right.\right.\\
&\left.\left.\left.\sqrt{\frac{2a_0^2\sigma_s^2}{\text{ISI-IQI}_{re}^{(1)}+2a_0\sigma_s^2-\frac{2\sigma_s^2}{N}(\sum\limits_{k=0}^{N-1}|A[k]|^2+|B[k]|^2)}}\right)\right]^2\right\}.
\end{aligned}\tag{5.30}$$

In order not to lose generality, the results in Eq. (5.30) are extended to the i-th iteration via Eq. (5.28) and Eq. (5.29). The BER expressions after the i-th iteration ($i > 1$) can be represented as

$$P_b^{(i)} \approx \frac{1}{\log_2 M}\left\{1-\left[1-2(1-\frac{1}{\sqrt{M}})Q\left(\sqrt{\frac{3\gamma_{out}^{(i)}}{M-1}}\right)\right]^2\right\}, \tag{5.31}$$

where

$$\gamma_{out}^{(i)} = \frac{2a_0^2\sigma_s^2}{\text{ISI-IQI}_{re}^{(i-1)} + 2a_0\sigma_s^2 - \frac{2\sigma_s^2}{N}(\sum\limits_{k=0}^{N-1}|A[k]|^2 + |B[k]|^2)} \tag{5.32}$$

and

$$\text{ISI-IQI}_{re}^{(i-1)} = \frac{24}{M-1}\Big[\big(\frac{2}{N}\sum_{k=0}^{N-1}|A[k]|^2 + \frac{1}{4}|B[k]|^2\big) - 2a_0^2\Big] \cdot \log_2 M P_b^{(i-1)}\sigma_s^2. \tag{5.33}$$

5.3.4 BER Lower Bound

When the joint interference is totally removed, the BER will reach a lower bound, which represents the limit of system performance. In this ideal condition, the output SNR can be derived from Eqs. (5.22) and (5.24) as

$$\begin{aligned}\gamma_0 &= \frac{\text{Power}\Big\{\text{desired signal}\Big\}}{\text{Power}\Big\{\text{noise}\Big\}} \\ &= \frac{a_0^2}{a_0 - \frac{1}{N}(\sum\limits_{k=0}^{N-1}|A[k]|^2 + |B[k]|^2)}.\end{aligned} \tag{5.34}$$

Then the BER lower bound for the M-QAM system is expressed as

$$\begin{aligned}P_{bLB} &\approx \frac{1}{\log_2 M}\Bigg\{1 - \Bigg[1 - 2(1-\frac{1}{\sqrt{M}})Q\left(\sqrt{\frac{3\gamma_0}{M-1}}\right)\Bigg]^2\Bigg\} \\ &= \frac{1}{\log_2 M}\Bigg\{1 - \Bigg[1 - 2(1-\frac{1}{\sqrt{M}})Q\Bigg(\sqrt{\frac{3}{M-1}} \\ &\quad \cdot \sqrt{\frac{a_0^2}{a_0 - \frac{1}{N}(\sum\limits_{k=0}^{N-1}|A[k]|^2 + |B[k]|^2)}}\Bigg)\Bigg]^2\Bigg\}.\end{aligned} \tag{5.35}$$

In slow-fading channels, the derived expressions are still applicable as the channel parameters can be assumed constant. Moreover, the ergodic BER can be obtained numerically by performing realisations as many as possible and calculating the average results.

5.4 Simulation Results

In this section, the robustness of the proposed scheme under various ISI and IQI conditions is assessed. Additionally, the BER performance of the scheme is evaluated and the derived

Table 5.2: Simulation Parameters

Carrier Frequency (f_c)	6 GHz		No. of Symbols per Frame (N)	256
No. of Frames	1500		3 dB Cut-off Frequency of the RRC Filter ($1/T$)	6.144 MHz
Time Acceleration Factor (α)	0.8		Roll-off Factor of the RRC Filter (β)	0.25
Frequency Resolution ($\Delta f = 1/(N\alpha T)$)	30 kHz		Sampling Rate ($F_s = N \cdot \Delta f$)	7.68 MHz

theoretical results under a variety of system parameters and transmission conditions is verified. Unless otherwise specified, 4-QAM modulation is employed, and the system parameters are presented in Table. 5.2. As described in Chapter 3, the relationship of α and β is set as $\beta = 1/\alpha - 1$ to ensure that the FTN bandwidth is fully utilised, which guarantees optimal transmission without being affected by the interference caused by zero-valued frequency bins at the edge of the signal bandwidth. For the IQI parameters of the transmitter, $H_{I,t}$ and $H_{Q,t}$ are implemented as a 4th-order Butterworth LPF with a 3 dB cut-off frequency of 3.805 MHz and a 4th-order Butterworth LPF with a 3 dB cut-off frequency of 3.777 MHz respectively. For the receiver, $H_{I,r}$ and $H_{Q,r}$ are implemented as a 4th-order Butterworth LPF with a 3 dB cut-off frequency of 3.827 MHz and a 4th-order Butterworth LPF with a 3 dB cut-off frequency of 3.782 MHz respectively. The simulations on TDL-A and TDL-D models are carried out based on the recommendations of the ETSI, which are detailed in Appendix 2-A. The simulation results are averaged over thousands of channel realisations with randomly generated CSIs. Both uncoded and coded systems with LDPC coding are simulated. Unless otherwise mentioned, the results presented in this section are for uncoded systems, the FTN coefficients are set as $[\alpha, \beta] = [0.8, 0.25]$ and the IQI coefficients are set as $g_t = 1.12$, $g_r = 0.89$, $\theta_t = 5°$ and $\theta_r = 5°$.

Table 5.3: IQI Coefficients of Different Cases

	Case 1 (Mild)	Case 2 (Medium)	Case 3 (Severe)
g_t	1.01	1.12	1.26
g_r	0.98	0.89	0.79
θ_t	1°	5°	10°
θ_r	1°	5°	10°

5.4.1 BER Performance under Different IQI Cases

First, the robustness of the proposed scheme against various IQI conditions is evaluated by comparing the BER performance in an IQI-free scenario with three IQI-affected cases in AWGN channels. In practical RF circuit implementations, the parameters g_t and g_r generally range from 1.01 to 1.05, while θ_t and θ_r typically lie within 1° to 5° [125]. As presented in Table 5.3, three different IQI environments are employed, where the "mild" and "medium" cases represent typical and extreme transmission conditions, respectively. Considering an exaggerated transmission condition as the "severe" case, the IQI mitigation capability of the scheme is demonstrated and a benchmark against two realistic scenarios is provided.

Figure 5.3 shows that in Case 1 and Case 2, the BER performance is nearly identical to the IQI-free scenario, confirming that DDSIC effectively mitigates IQI in these conditions. Even under the beyond-realistic IQI conditions in Case 3, the SNR degradation at the target BER of 10^{-5} is only about 0.5 dB. This demonstrates the robustness of the proposed scheme in mitigating IQI in practical implementations.

5.4.2 BER Performance Comparison

In this subsection, the BER performance of the proposed DDSIC algorithm is compared with those of the truncated VA in [56], the M-BCJR algorithm in [67], the symbol-based SSSSE and SSSgbKSE in [54] and the EVD-based precoding scheme in [44]. The memory length of the truncated VA algorithm is set to 3, and the survivor number of the M-BCJR algorithm is set to 4. 6 ISI symbols are considered and the go-back length K is set as 3 for SSSSE and SSSgbKSE.

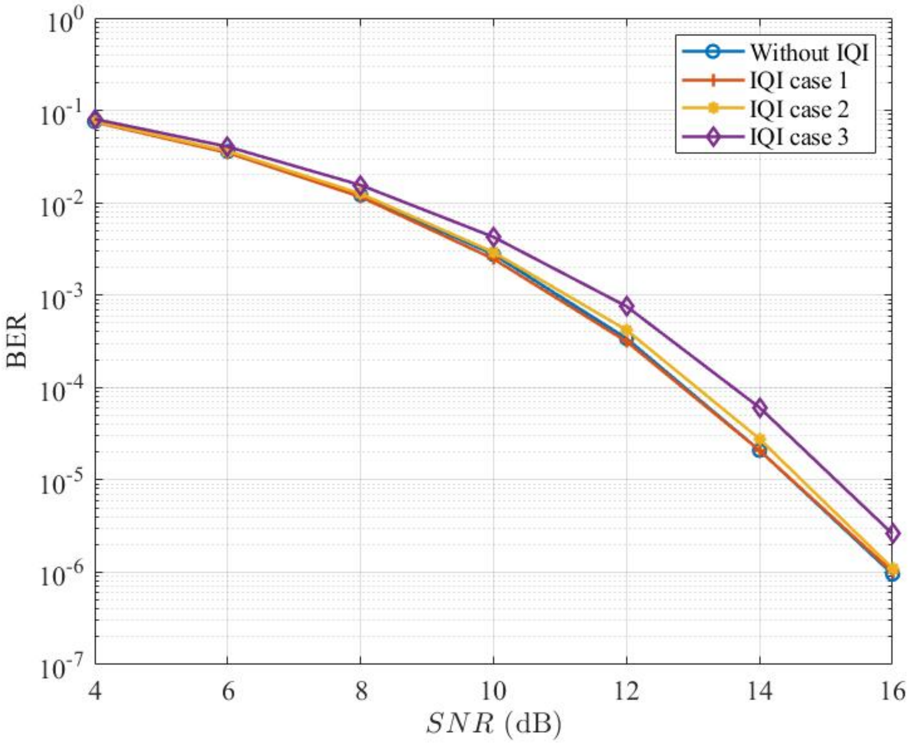

Figure 5.3: BER performance of the fifth iteration for DDSIC under various IQI cases in AWGN channel.

Figure 5.4 presents the BER performances of various algorithms and the theoretical BER curves under the AWGN channel. Observe that the theoretical BER curves align closely with the simulated ones. As there is no channel fading, when SNR>12 dB, the BER performances of DDSIC after the second iteration converge to the derived lower bound. With increasing SNR, the EVD-based method shows the worst performance due to zero distortion [44]. In the first iteration, without interference cancellation being applied, the proposed scheme shows a poorer BER performance compared to the truncated VA and the M-BCJR algorithms. Nevertheless, after the second iteration, a remarkable performance enhancement is observed, enabling it to outperform both algorithms. For the target BER of 10^{-4}, the required SNR for the fifth iteration of the DDSIC algorithm is approximately 1.5 dB lower than that of the truncated VA, approximately 2.8 dB lower than that of the SSSgbKSE, and far lower than those of the SSSSE and EVD-based method. The BER performance of DDSIC and M-BCJR is nearly identical. However, the DDSIC algorithm operates with much lower computational complexity compared to the M-BCJR algorithm, as it avoids the need to traverse the state map for every frame. Compared with the perfect ISI-free and IQI-free case, the required SNR for the fifth iteration of the DDSIC algorithm is approximately 2.2 dB higher to achieve a target BER of 10^{-5}.

Figures 5.5 and 5.6 illustrate the BER performance of the proposed DDSIC scheme under TDL-A (NLOS) and TDL-D (LOS) channels, respectively. The results indicate that DDSIC remains effective in both LOS and NLOS scenarios and outperforms the truncated VA algorithm. Due to the limited adjacent symbols, SSSSE and SSSgbKSE both lose effectiveness in this context, whereas EVD-based method demonstrates robustness under both LOS and NLOS channels. However, in the absence of channel coding, its performance in mitigating ISI and IQI remains inferior to that of DDSIC. Specifically, for a target BER of 10^{-4}, the SNR difference between the fifth iteration of DDSIC and the truncated VA is approximately 3.8 dB in the TDL-A NLOS channel and 0.7 dB in the TDL-D LOS channel, and the SNR gap between the fifth-iter-DDSIC and the EVD-precoding is approximately 2.7 dB for the TDL-A NLOS channel and 5.5 dB for the TDL-D LOS channel. Notably, DDSIC achieves convergence after the fourth iteration, by which point the majority of IQI and ISI have been mitigated. Additionally, the theoretical BER results align well with the simulation outcomes in both channels, validating the accuracy

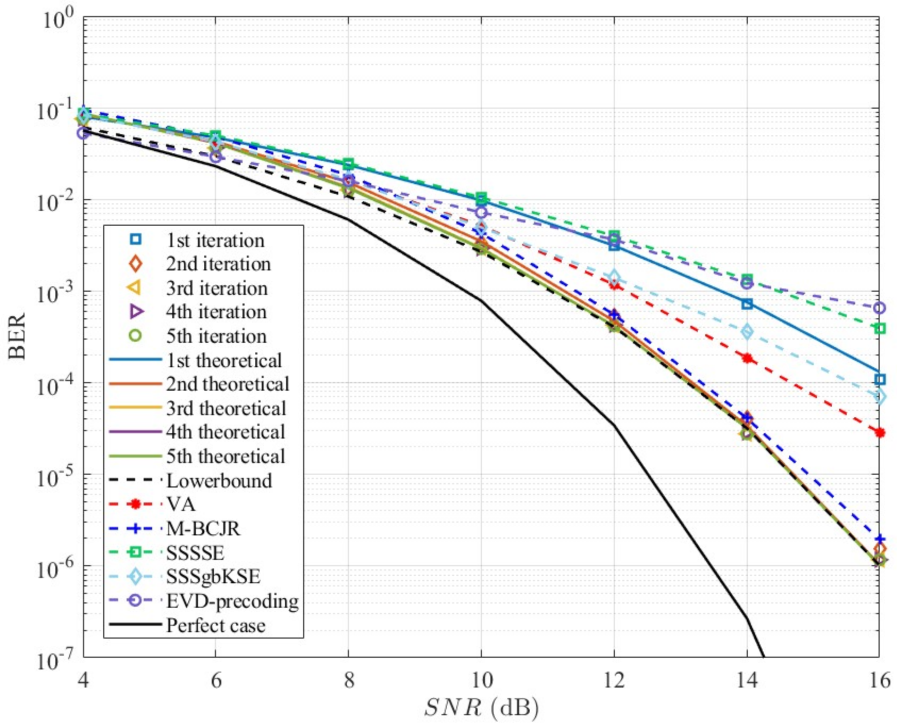

Figure 5.4: BER performance of various algorithms (solid) and theoretical results (dashed) in AWGN channel.

of the derived theoretical expressions.

5.4.3 BER Performance with Higher-Order Modulation

The BER performance of DDSIC with 16-QAM mapping is evaluated is this subsection. In this case, the computational complexity of the M-BCJR algorithm is almost 3×2^{15} times greater than that of the DDSIC scheme, making it impractical for implementation. Similarly, uncoded EVD-based method is unsuitable with 16-QAM modulation under multipath fading channels due to the impact of zero distortion. Therefore, DDSIC is only compared with the truncated VA. As depicted in Figures 5.7 and 5.8, the proposed DDSIC scheme demonstrates strong performance with 16-QAM modulation across both LOS and NLOS channels. In the first iteration, without interference cancellation, the BER performance in both channels closely matches that of the truncated VA algorithm. Consistent with the results shown in Figures 5.5 and 5.6, the majority of ISI and IQI are effectively mitigated by the fourth iteration. Specifically, in the NLOS channel, the proposed scheme reaches a BER of 10^{-4} at an SNR of approximately

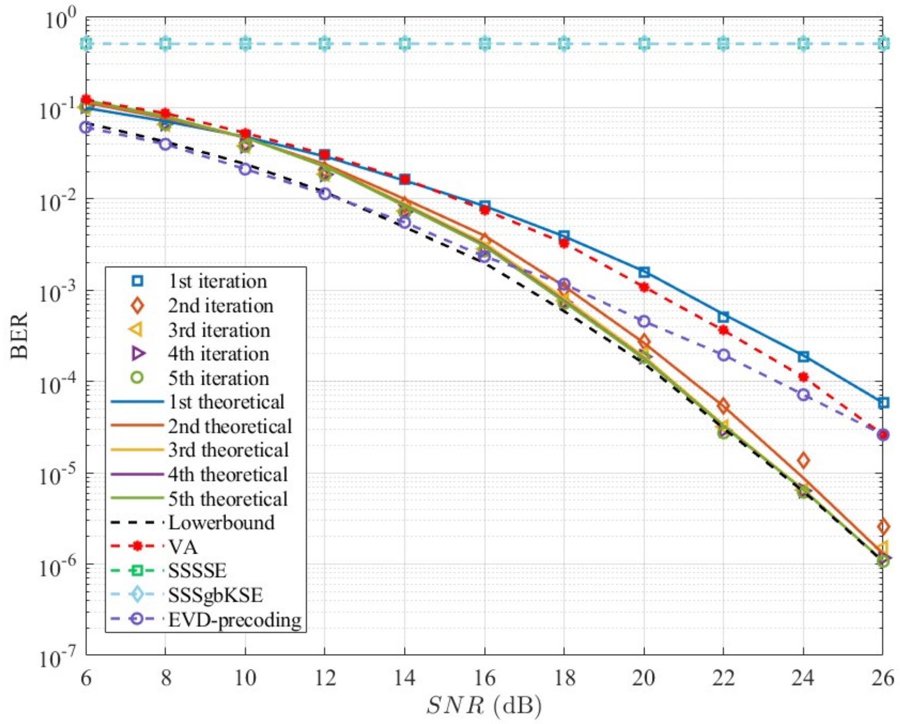

Figure 5.5: BER performance of various algorithms (solid) and theoretical results (dashed) in TDL-A channel.

35 dB, whereas in the LOS channel, the same BER is attained at an SNR of approximately 27.5 dB.

5.4.4 Combination with Channel Coding

To explore the potential of combination with channel coding, the BER performance of the proposed system when integrated with channel coding is assessed. Specifically, QC-LDPC coding is applied using soft outputs from each DDSIC iteration. The code rate is set at 0.75, with a block length of 648 bits, including 486 information bits and 162 parity check bits. As shown in Figure 5.9, the proposed scheme demonstrates effective performance under all three channel conditions when using LDPC coding. In the AWGN channel, the LDPC-coded scheme achieves a performance gain of approximately 6.7 dB compared to the uncoded scheme at a target BER of 10^{-4}. Furthermore, the SNR enhancement is around 5 dB for the TDL-A channel and approximately 3.7 dB for the TDL-D channel. Overall, integrating LDPC coding enhances the performance of the proposed scheme in both ideal and practical scenarios, further validating

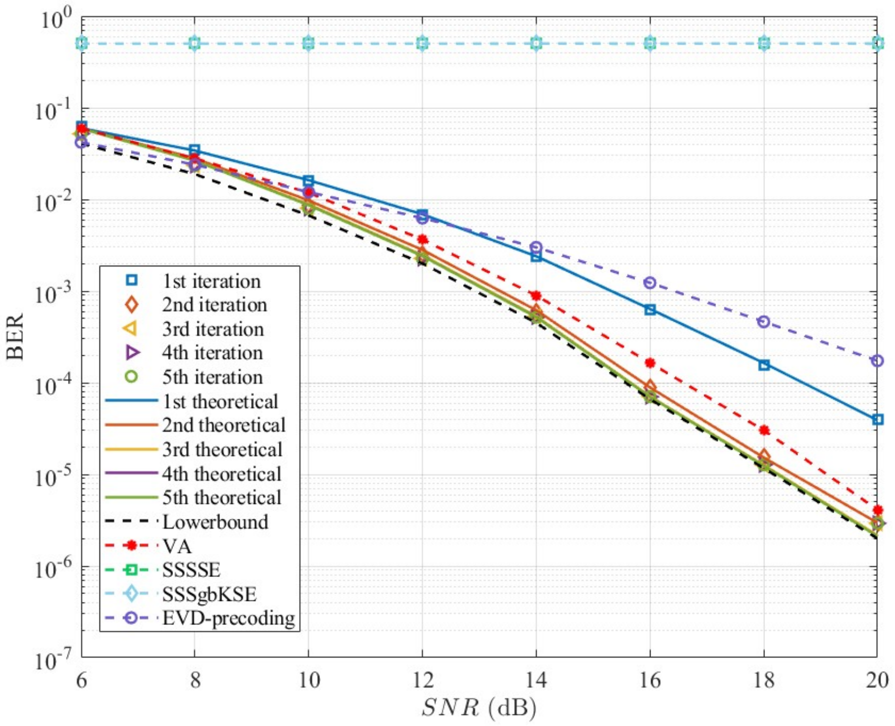

Figure 5.6: BER performance of various algorithms (solid) and theoretical results (dashed) in TDL-D channel.

its feasibility for real-world implementation.

5.5 Conclusions

In this chapter, a more realistic FTN system is proposed that considers both ISI and frequency-dependent IQI problems. FTN signal model is improved from one dimension to an extended dimension, which ensures the feasibility of the conventional DDSIC to mitigate ISI and IQI jointly. To mathematically express the performance, the theoretical BERs for each iteration of DDSIC and a BER lower bound of the proposed system are derived. The simulation results demonstrate that the proposed scheme remains robust under diverse IQI conditions. In mild and moderate IQI cases, the system performance closely approximates the ideal IQI-free scenario, with negligible BER degradation. Even under severe IQI conditions, the observed degradation of BER remains within acceptable limits. Additionally, further simulations validate the superiority of the DDSIC algorithm over existing methods, while also confirming the

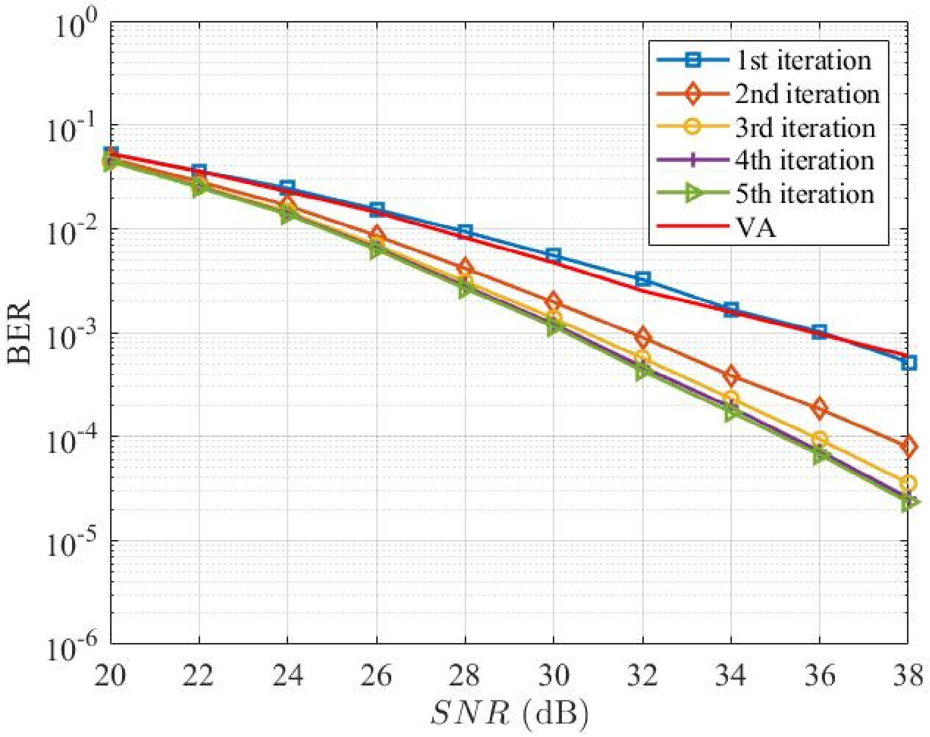

Figure 5.7: BER performance of various algorithms with 16-QAM modulation in TDL-A channel.

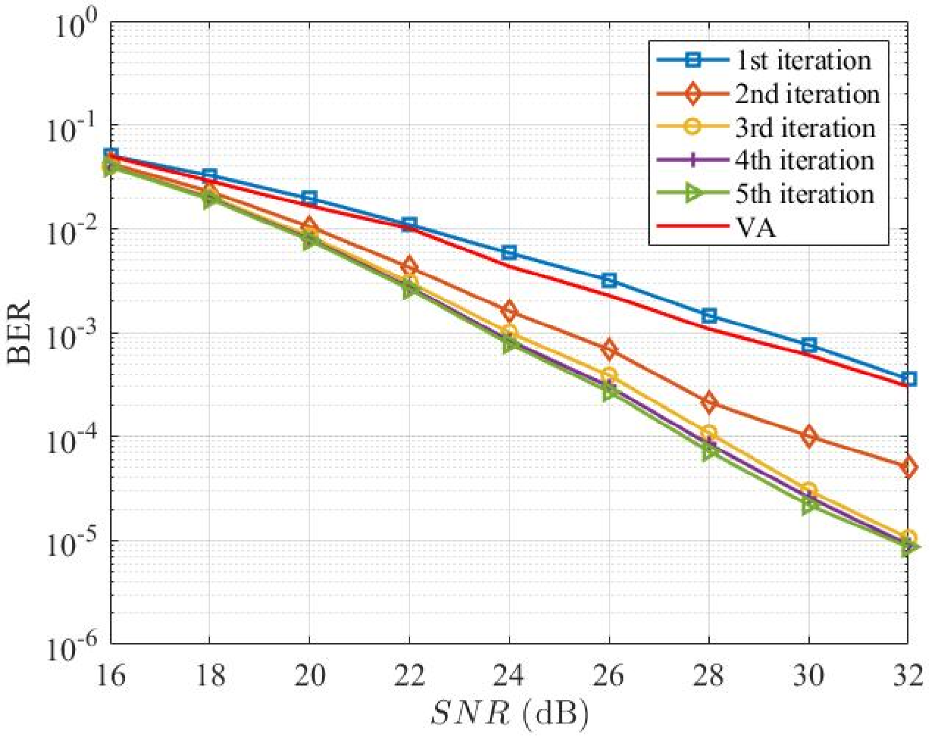

Figure 5.8: BER performance of various algorithms with 16-QAM modulation in TDL-D channel.

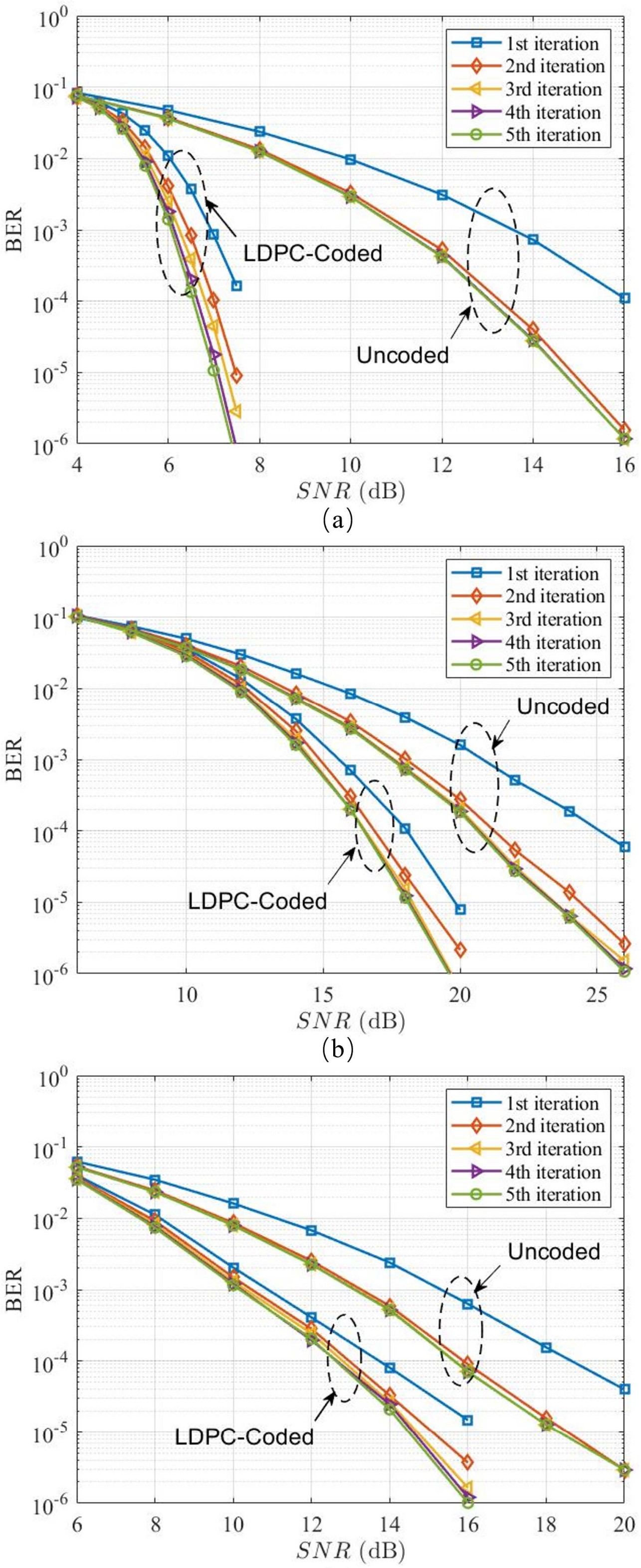

Figure 5.9: BER performance comparison of the proposed scheme with and without LDPC coding in: (a) AWGN channel, (b) TDL-A channel, and (c) TDL-D channel.

correctness of the derived BER metrics.

Chapter 6

Conclusions and Future Work

This chapter revisits the primary research objectives outlined in Chapter 1, summarises how these objectives have been addressed throughout the thesis, and outlines potential avenues for future work.

6.1 Conclusions

The overarching aim of this thesis is to develop an implementable FTN communication framework that addresses key challenges including ISI, fast-fading multipath effects, and IQI. The motivation stems from the need for spectrally efficient and robust wireless communication systems that are practical under non-ideal conditions. To address the above aim, this thesis presents a series of advancements in FTN system design, focusing on low-complexity ISI cancellation, adaptive precoding, and compensation for practical impairments. The proposed DDSIC algorithm, which integrates FD-MMSE equalisation with successive interference cancellation, significantly reduces computational complexity while maintaining robust BER performance across various channel conditions. Theoretical BER expressions and lower bounds provide valuable benchmarks for practical implementation.

To further enhance FTN system reliability in dynamic environments, an ATPC-based FTN signalling scheme is introduced, effectively transforming fast-fading channels into slow-fading equivalents. Theoretical and simulation analyses confirm its feasibility, demonstrating the priority over state-of-the-art methods.

Finally, the thesis extends the FTN model to address both ISI and frequency-dependent IQI, demonstrating that the improved DDSIC algorithm effectively mitigates these impairments. Theoretical and simulation results confirm that system performance remains robust even under severe IQI conditions. Collectively, these contributions lay the foundation for practical, cost-effective FTN signalling in future wireless communication systems.

6.2 Future Research Directions

The proposed FTN system and the DDSIC algorithm can be improved and integrated with emerging 5G technologies. The potential research directions in my future work are provided as follows.

6.2.1 Optimisation of DDSIC Algorithm

The optimization of the current DDSIC algorithm can be approached from two perspectives.

First, the existing scheme employs hard-decision demodulation, where symbols are converted into data bits through a threshold-based comparison. This approach results in a quantized, one-bit decision regarding the transmitted symbol's state. In contrast, soft-decision demodulation retains more granular information about the received signal, such as amplitude or likelihood metrics for each bit, rather than making a binary decision. By preserving the probability of each bit being a 0 or 1, soft-decision provides a measure of reliability, making SISO processing potentially more accurate than hard-decision in our system.

Second, the normalization process, which aims to compensate for channel response effects, can be optimized by either multiplying the directly decided signal or dividing the difference signal by a scaling factor. This factor is derived from the input SNR of the MMSE equaliser. Such optimization is expected to enhance data recovery performance, particularly in low-SNR regimes.

6.2.2 More General Channel Model and Channel Estimation

In Chapter 4, Doppler shift with integer value is identified as the primary source of interference in fast-fading channels. The developed channel model is designed to be general, accommodating both integer and fractional time delays as well as Doppler shifts. This flexibility ensures its applicability to a wide range of practical scenarios. However, in reality, perfect CSI is unattainable, necessitating a robust channel estimation method. Such a method must perform effectively under fast-fading conditions and handle both integer and fractional time delays and Doppler shifts. Additionally, the DDSIC algorithm can be enhanced to mitigate the impact of channel estimation errors. Replacing the direct feedback of the $\mathbf{Q}$ matrix with a codebook-based feedback mechanism is another promising approach, as it would significantly reduce feedback overhead, improving the system's efficiency and scalability.

6.2.3 Consideration of More Realistic Impairments

Beyond IQI problem, the proposed scheme can be extended to address other practical hardware impairments. One critical impairment is carrier frequency offset (CFO), which results from mismatches between the local oscillators at the transmitter and receiver, as well as Doppler shifts caused by the motion of the transmitter, receiver, or propagation medium. CFO introduces a time-varying phase rotation, leading to frequency shifts in the received signal. These shifts exacerbate ISI and frequency errors in FTN systems. To counteract this, the scheme can incorporate time-varying phase rotation compensation mechanisms.

Another significant source of performance degradation is system nonlinearity, which arises in components such as power amplifiers, mixers, digital-to-analog converters (DACs), and analog-to-digital converters (ADCs) [126]. Digital compensation techniques, such as those proposed in [126]–[128], can be integrated into the system to mitigate these nonlinear effects, further enhancing its robustness and reliability.

Bibliography

[1] 3GPP, "Release 15 - 3GPP," *3GPP Specifications*, 2018, Available: `https://www.3gpp.org/release-15`.

[2] 3GPP, "Release 16 - 3GPP," *3GPP Specifications*, 2020, Available: `https://www.3gpp.org/release-16`.

[3] M. Shafi, A. F. Molisch, P. J. Smith, *et al.*, "5G: A tutorial overview of standards, trials, challenges, deployment, and practice," *IEEE journal on selected areas in communications*, vol. 35, no. 6, pp. 1201–1221, 2017.

[4] J. G. Andrews, S. Buzzi, W. Choi, *et al.*, "What will 5G be?" *IEEE Journal on Selected Areas in Communications*, vol. 32, no. 6, pp. 1065–1082, 2014.

[5] T. S. Rappaport, S. Sun, R. Mayzus, *et al.*, "Millimeter wave mobile communications for 5G cellular: It will work!" *IEEE Access*, vol. 1, pp. 335–349, 2013.

[6] C.-X. Wang, F. Haider, X. Gao, *et al.*, "Cellular architecture and key technologies for 5G wireless communication networks," *IEEE Communications Magazine*, vol. 52, no. 2, pp. 122–130, 2014.

[7] E. Björnson, J. Hoydis, L. Sanguinetti, *et al.*, "Massive MIMO networks: Spectral, energy, and hardware efficiency," *Foundations and Trends® in Signal Processing*, vol. 11, no. 3-4, pp. 154–655, 2017.

[8] R. W. Heath, N. Gonzalez-Prelcic, S. Rangan, W. Roh, and A. M. Sayeed, "An overview of signal processing techniques for millimeter wave MIMO systems," *IEEE Journal of Selected Topics in Signal Processing*, vol. 10, no. 3, pp. 436–453, 2016.

[9] T. S. Rappaport, Y. Xing, G. R. MacCartney, A. F. Molisch, E. Mellios, and J. Zhang, "Overview of millimeter wave communications for fifth-generation (5G) wireless networks—With a focus on propagation models," *IEEE Transactions on Antennas and Propagation*, vol. 65, no. 12, pp. 6213–6230, 2017.

[10] C. Jiang, H. Zhang, Y. Ren, Z. Han, K.-C. Chen, and L. Hanzo, “Machine learning paradigms for next-generation wireless networks,” *IEEE Wireless Communications*, vol. 24, no. 2, pp. 98–105, 2016.

[11] H. Sun, X. Chen, Q. Shi, M. Hong, X. Fu, and N. D. Sidiropoulos, “Learning to optimize: Training deep neural networks for wireless resource management,” in *2017 IEEE 18th International Workshop on Signal Processing Advances in Wireless Communications (SPAWC)*, IEEE, 2017, pp. 1–6.

[12] A. Mihovska, R. Prasad, *et al.*, “Spectrum sharing and dynamic spectrum management techniques in 5G and beyond networks: A survey,” *Journal of Mobile Multimedia*, pp. 65–78, 2021.

[13] R. Irmer, H. Droste, P. Marsch, *et al.*, “Coordinated multipoint: Concepts, performance, and field trial results,” *IEEE Communications Magazine*, vol. 49, no. 2, pp. 102–111, 2011.

[14] Y. Mao, C. You, J. Zhang, K. Huang, and K. B. Letaief, “A survey on mobile edge computing: The communication perspective,” *IEEE Communications Surveys & Tutorials*, vol. 19, no. 4, pp. 2322–2358, 2017.

[15] X. Foukas, G. Patounas, A. Elmokashfi, and M. K. Marina, “Network slicing in 5G: Survey and challenges,” *IEEE Communications Magazine*, vol. 55, no. 5, pp. 94–100, 2017.

[16] T. Taleb, S. Dutta, A. Ksentini, M. Iqbal, and H. Flinck, “Mobile edge computing potential in making cities smarter,” *IEEE Communications Magazine*, vol. 55, no. 3, pp. 38–43, 2017.

[17] M. Torres Vega, C. Liaskos, S. Abadal, *et al.*, “Immersive interconnected virtual and augmented reality: A 5G and IoT perspective,” *Journal of Network and Systems Management*, vol. 28, pp. 796–826, 2020.

[18] I. Rahman, S. M. Razavi, O. Liberg, *et al.*, “5G evolution toward 5G advanced: An overview of 3GPP releases 17 and 18,” *Ericsson Technology Review*, vol. 2021, no. 14, pp. 2–12, 2021.

[19] P. Popovski, J. J. Nielsen, C. Stefanovic, *et al.*, “Wireless access for ultra-reliable low-latency communication: Principles and building blocks,” *IEEE Network*, vol. 32, no. 2, pp. 16–23, 2018.

[20] Q. C. Li, H. Niu, A. T. Papathanassiou, and G. Wu, “5G network capacity: Key elements and technologies,” *IEEE Vehicular Technology Magazine*, vol. 9, no. 1, pp. 71–78, 2014.

[21] P. P. Sriram, H.-C. Wang, H. G. Jami, and K. Srinivasan, “5G security: Concepts and challenges,” *5G Enabled Secure Wireless Networks*, pp. 1–43, 2019.

[22] I. F. Akyildiz, A. Kak, and S. Nie, “6G and beyond: The future of wireless communications systems,” *IEEE Access*, vol. 8, pp. 133 995–134 030, 2020.

[23] M. Giordani, M. Polese, M. Mezzavilla, S. Rangan, and M. Zorzi, “Toward 6G networks: Use cases and technologies,” *IEEE Communications Magazine*, vol. 58, no. 3, pp. 55–61, 2020.

[24] L. Gyongyosi and S. Imre, “A survey on quantum computing technology,” *Computer Science Review*, vol. 31, pp. 51–71, 2019.

[25] H. Tataria, M. Shafi, A. F. Molisch, M. Dohler, H. Sjöland, and F. Tufvesson, “6G wireless systems: Vision, requirements, challenges, insights, and opportunities,” *Proceedings of the IEEE*, vol. 109, no. 7, pp. 1166–1199, 2021.

[26] S. Dang, O. Amin, B. Shihada, and M.-S. Alouini, “What should 6G be?” *Nature Electronics*, vol. 3, no. 1, pp. 20–29, 2020.

[27] M. Z. Chowdhury, M. Shahjalal, S. Ahmed, and Y. M. Jang, “6G wireless communication systems: Applications, requirements, technologies, challenges, and research directions,” *IEEE Open Journal of the Communications Society*, vol. 1, pp. 957–975, 2020.

[28] H. Nyquist, “Certain factors affecting telegraph speed,” *Transactions of the American Institute of Electrical Engineers*, vol. 43, pp. 412–422, 1924.

[29] J. E. Mazo, “Faster-than-Nyquist signaling,” *The Bell System Technical Journal*, vol. 54, no. 8, pp. 1451–1462, 1975.

[30] J. B. Anderson, F. Rusek, and V. Öwall, “Faster-than-Nyquist signaling,” *Proceedings of the IEEE*, vol. 101, no. 8, pp. 1817–1830, 2013.

[31] A. D. Liveris and C. N. Georghiades, “Exploiting faster-than-Nyquist signaling,” *IEEE Transactions on Communications*, vol. 51, no. 9, pp. 1502–1511, 2003.

[32] J. Erfanian, S. Pasupathy, and G. Gulak, “Reduced complexity symbol detectors with parallel structure for ISI channels,” *IEEE Transactions on Communications*, vol. 42, no. 234, pp. 1661–1671, 1994.

[33] J. Salz, “Optimum mean-square decision feedback equalization,” *Bell System Technical Journal*, vol. 52, no. 8, pp. 1341–1373, 1973.

[34] S. Sugiura, "Frequency-domain equalization of faster-than-Nyquist signaling," *IEEE Wireless Communications Letters*, vol. 2, no. 5, pp. 555–558, 2013.

[35] G. D. Forney, "The viterbi algorithm," *Proceedings of the IEEE*, vol. 61, no. 3, pp. 268–278, 2005.

[36] L. Bahl, J. Cocke, F. Jelinek, and J. Raviv, "Optimal decoding of linear codes for minimizing symbol error rate (corresp.)," *IEEE Transactions on information theory*, vol. 20, no. 2, pp. 284–287, 2003.

[37] G. Colavolpe, D. Fertonani, and A. Piemontese, "SISO detection over linear channels with linear complexity in the number of interferers," *IEEE Journal of Selected Topics in Signal Processing*, vol. 5, no. 8, pp. 1475–1485, 2011.

[38] G. Forney, "Maximum-likelihood sequence estimation of digital sequences in the presence of intersymbol interference," *IEEE Transactions on Information theory*, vol. 18, no. 3, pp. 363–378, 1972.

[39] V. Franz and J. B. Anderson, "Concatenated decoding with a reduced-search BCJR algorithm," *IEEE Journal on selected Areas in Communications*, vol. 16, no. 2, pp. 186–195, 1998.

[40] F. Rusek and A. Prlja, "Optimal channel shortening for MIMO and ISI channels," *IEEE transactions on wireless communications*, vol. 11, no. 2, pp. 810–818, 2011.

[41] A. Modenini, F. Rusek, and G. Colavolpe, "Optimal transmit filters for ISI channels under channel shortening detection," *IEEE Transactions on Communications*, vol. 61, no. 12, pp. 4997–5005, 2013.

[42] S. Wen, G. Liu, C. Liu, H. Qu, L. Zhang, and M. A. Imran, "Joint precoding and pre-equalization for faster-than-Nyquist transmission over multipath fading channels," *IEEE Transactions on Vehicular Technology*, vol. 71, no. 4, pp. 3948–3963, 2022.

[43] T. Ishihara and S. Sugiura, "Reduced-complexity FFT-spread multicarrier faster-than-Nyquist signaling in frequency-selective fading channel," *IEEE Open Journal of the Communications Society*, vol. 3, pp. 530–542, 2022.

[44] T. Ishihara and S. Sugiura, "Eigendecomposition-precoded faster-than-Nyquist signaling with optimal power allocation in frequency-selective fading channels," *IEEE Transactions on Wireless Communications*, vol. 21, no. 3, pp. 1681–1693, 2021.

[45] T. Ishihara and S. Sugiura, "FFT-spread faster-than-Nyquist signaling in frequency-selective fading channel," in *ICC 2022-IEEE International Conference on Communications*, IEEE, 2022, pp. 2399–2404.

[46] Q. Li, F.-K. Gong, P.-Y. Song, G. Li, and S.-H. Zhai, "Joint channel estimation and precoding for faster-than-Nyquist signaling," *IEEE Transactions on Vehicular Technology*, vol. 69, no. 11, pp. 13 139–13 147, 2020.

[47] K. Wang, A. Liu, X. Liang, and S. Pen, "Unique faster-than-Nyquist transceiver of the ACM system," *IET Communications*, vol. 12, no. 4, pp. 432–440, 2018.

[48] F. Mazzenga and G. E. Corazza, "Blind least-squares estimation of carrier phase, Doppler shift, and Doppler rate for m-PSK burst transmission," *IEEE Communications Letters*, vol. 2, no. 3, pp. 73–75, 1998.

[49] A. Tajer and A. Nosratinia, "Diversity order in ISI channels with single-carrier frequency-domain equalizers," *IEEE Transactions on Wireless Communications*, vol. 9, no. 3, pp. 1022–1032, 2010.

[50] D. Dasalukunte, F. Rusek, and V. Owall, "Multicarrier faster-than-Nyquist transceivers: Hardware architecture and performance analysis," *IEEE Transactions on Circuits and Systems I: Regular Papers*, vol. 58, no. 4, pp. 827–838, 2010.

[51] D. Dasalukunte, F. Rusek, and V. Öwall, "An 0.8-mm^2 9.6-mW iterative decoder for faster-than-Nyquist and orthogonal signaling multicarrier systems in 65-nm CMOS," *IEEE journal of solid-state circuits*, vol. 48, no. 7, pp. 1680–1688, 2013.

[52] M. Jana, L. Lampe, and J. Mitra, "Dual-polarized faster-than-Nyquist transmission using higher order modulation schemes," *IEEE Transactions on Communications*, vol. 66, no. 11, pp. 5332–5345, 2018.

[53] X. Huang, H. Zhang, A. T. Le, J. Andrew Zhang, and Y. Jay Guo, "Digital post-cancellation of nonlinear interference for millimeter wave and terahertz systems," *IEEE Transactions on Wireless Communications*, vol. 23, no. 11, pp. 16 033–16 047, 2024.

[54] E. Bedeer, M. H. Ahmed, and H. Yanikomeroglu, "A very low complexity successive symbol-by-symbol sequence estimator for faster-than-Nyquist signaling," *IEEE Access*, vol. 5, pp. 7414–7422, 2017.

[55] P. Raviteja, K. T. Phan, Y. Hong, and E. Viterbo, "Interference cancellation and iterative detection for orthogonal time frequency space modulation," *IEEE transactions on wireless communications*, vol. 17, no. 10, pp. 6501–6515, 2018.

[56] A. Prlja, J. B. Anderson, and F. Rusek, “Receivers for faster-than-Nyquist signaling with and without turbo equalization,” in *2008 IEEE International Symposium on Information Theory*, IEEE, 2008, pp. 464–468.

[57] H. Che and Y. Bai, “M-BCJR algorithm with channel shortening based on ungerboeck observation model for faster-than-Nyquist signaling,” *China Communications*, vol. 18, no. 4, pp. 88–98, 2021.

[58] G. J. Foschini, “Contrasting performance of faster binary signaling with QAM,” *AT&T Bell Laboratories technical journal*, vol. 63, no. 8, pp. 1419–1445, 1984.

[59] D. Hajela, “On computing the minimum distance for faster than Nyquist signaling,” *IEEE transactions on information theory*, vol. 36, no. 2, pp. 289–295, 1990.

[60] J. E. Mazo and H. J. Landau, “On the minimum distance problem for faster-than-Nyquist signaling,” *IEEE Transactions on Information Theory*, vol. 34, no. 6, pp. 1420–1427, 1988.

[61] J.-H. Lee and Y.-H. Lee, “Design of multiple MMSE subequalizers for faster-than-Nyquist-rate transmission,” *IEEE transactions on communications*, vol. 52, no. 8, pp. 1257–1264, 2004.

[62] F. Rusek and J. B. Anderson, “The two dimensional Mazo limit,” in *Proceedings. International Symposium on Information Theory, 2005. ISIT 2005.*, IEEE, 2005, pp. 970–974.

[63] J. B. Anderson and F. Rusek, “Improving OFDM: Multistream faster-than-Nyquist signaling,” in *4th International Symposium on Turbo Codes & Related Topics; 6th International ITG-Conference on Source and Channel Coding*, VDE, 2006, pp. 1–5.

[64] D. Dasalukunte, F. Rusek, and V. Öwall, “An iterative decoder for multicarrier faster-than-Nyquist signaling systems,” in *2010 IEEE International Conference on Communications*, IEEE, 2010, pp. 1–5.

[65] J. Hagenauer and P. Hoeher, “A Viterbi algorithm with soft-decision outputs and its applications,” in *1989 IEEE Global Telecommunications Conference and Exhibition “Communications Technology for the 1990s and Beyond”*, IEEE, 1989, pp. 1680–1686.

[66] R. J. McEliece, “On the BCJR trellis for linear block codes,” *IEEE Transactions on Information Theory*, vol. 42, no. 4, pp. 1072–1092, 2002.

[67] A. Prlja and J. B. Anderson, “Reduced-complexity receivers for strongly narrowband intersymbol interference introduced by faster-than-Nyquist signaling,” *IEEE Transactions on Communications*, vol. 60, no. 9, pp. 2591–2601, 2012.

[68] S. Li, B. Bai, J. Zhou, P. Chen, and Z. Yu, “Reduced-complexity equalization for faster-than-Nyquist signaling: New methods based on Ungerboeck observation model,” *IEEE Transactions on Communications*, vol. 66, no. 3, pp. 1190–1204, 2017.

[69] M.-S. Baek, N.-H. Hur, and H. Lim, “Novel interference cancellation technique based on matrix computation for FTN communication system,” in *2014 IEEE Military Communications Conference*, IEEE, 2014, pp. 830–834.

[70] M.-S. Baek, J. Yun, N. Hur, and H. Lim, “Interference cancellation and signal detection technique based on QRD-M algorithm for FTN signalling,” *Electronics letters*, vol. 53, no. 6, pp. 409–411, 2017.

[71] T. Ishihara and S. Sugiura, “SVD-precoded faster-than-Nyquist signaling with optimal and truncated power allocation,” *IEEE Transactions on Wireless Communications*, vol. 18, no. 12, pp. 5909–5923, 2019.

[72] Y. Li, S. Xiao, J. Wang, and W. Tang, “Cholesky-decomposition aided linear precoding and decoding for FTN signaling,” *IEEE Wireless Communications Letters*, vol. 10, no. 6, pp. 1163–1167, 2021.

[73] Q. Li, L. Li, Y. Li, W. Han, X. Li, and D. B. da Costa, “Low-complexity SVD precoding for faster-than-Nyquist signaling using high-order modulations,” *IEEE Transactions on Aerospace and Electronic Systems*, vol. 60, no. 1, pp. 591–603, 2023.

[74] Z. Zhang, M. Yuksel, and H. Yanikomeroglu, “Faster-than-Nyquist signaling for MIMO communications,” *IEEE Transactions on Wireless Communications*, vol. 22, no. 4, pp. 2379–2392, 2022.

[75] P. Chaki, T. Ishihara, and S. Sugiura, “Eigendecomposition-precoded faster-than-Nyquist signaling with index modulation,” *IEEE Transactions on Communications*, vol. 70, no. 7, pp. 4822–4836, 2022.

[76] G.-W. Park and J.-W. Jung, “A study on MIMO-FTN scheme based on layered space time code using turbo codes,” in *2016 Eighth International Conference on Ubiquitous and Future Networks (ICUFN)*, IEEE, 2016, pp. 505–507.

[77] W. Yuan, N. Wu, A. Zhang, X. Huang, Y. Li, and L. Hanzo, “Iterative receiver design for FTN signaling aided sparse code multiple access,” *IEEE Transactions on Wireless Communications*, vol. 19, no. 2, pp. 915–928, 2019.

[78] W. Yuan, N. Wu, Q. Guo, D. W. K. Ng, J. Yuan, and L. Hanzo, “Iterative joint channel estimation, user activity tracking, and data detection for FTN-NOMA systems supporting random access,” *IEEE Transactions on Communications*, vol. 68, no. 5, pp. 2963–2977, 2020.

[79] M. Ganji, X. Zou, and H. Jafarkhani, “On the capacity of faster than Nyquist signaling,” *IEEE Communications Letters*, vol. 24, no. 6, pp. 1197–1201, 2020.

[80] F. Rusek and J. B. Anderson, “Constrained capacities for faster-than-Nyquist signaling,” *IEEE Transactions on Information Theory*, vol. 55, no. 2, pp. 764–775, 2009.

[81] C. Si, S. Li, M. Liu, B. Bai, and J. Wang, “An iterative receiver for coded faster-than-Nyquist signaling over Rayleigh fading channels,” in *2022 IEEE/CIC International Conference on Communications in China (ICCC Workshops)*, IEEE, 2022, pp. 472–477.

[82] Q. Shi, N. Wu, X. Ma, and H. Wang, “Frequency-domain joint channel estimation and decoding for faster-than-Nyquist signaling,” *IEEE Transactions on Communications*, vol. 66, no. 2, pp. 781–795, 2017.

[83] H.-T. Chiu, S. Saito, H. Suganuma, *et al.*, “Performance evaluation of MIMO-FTN signaling under multipath fading channels,” *IEEE Access*, 2023.

[84] T. Yu, M. Zhao, J. Zhong, J. Zhang, and P. Xiao, “Low-complexity graph-based turbo equalisation for single-carrier and multi-carrier FTN signalling,” *IET Signal Processing*, vol. 11, no. 7, pp. 838–845, 2017.

[85] T. Xu and I. Darwazeh, “A soft detector for spectrally efficient systems with non-orthogonal overlapped sub-carriers,” *IEEE Communications Letters*, vol. 18, no. 10, pp. 1847–1850, 2014.

[86] Y. Yamada, M. Sawahashi, and K. Saito, “Performance of time and frequency compression of faster-than-Nyquist signaling in frequency-selective fading channels,” in *2015 21st Asia-Pacific Conference on Communications (APCC)*, IEEE, 2015, pp. 550–554.

[87] N. Wu, W. Yuan, Q. Guo, and J. Kuang, “A hybrid BP-EP-VMP approach to joint channel estimation and decoding for FTN signaling over frequency selective fading channels,” *IEEE Access*, vol. 5, pp. 6849–6858, 2017.

[88] Y. Ma, N. Wu, J. A. Zhang, B. Li, and L. Hanzo, "Parametric bilinear iterative generalized approximate message passing reception of FTN multi-carrier signaling," *IEEE Transactions on Communications*, vol. 69, no. 12, pp. 8443–8458, 2021.

[89] T. Ishihara and S. Sugiura, "Differential multi-carrier faster-than-Nyquist signaling in doubly selective fading channel," *IEEE Transactions on Vehicular Technology*, vol. 73, no. 1, pp. 1424–1429, 2023.

[90] W. Yuan, N. Wu, H. Wang, and J. Kuang, "Variational inference-based frequency-domain equalization for faster-than-nyquist signaling in doubly selective channels," *IEEE Signal Processing Letters*, vol. 23, no. 9, pp. 1270–1274, 2016.

[91] H. Harashima and H. Miyakawa, "Matched-transmission technique for channels with intersymbol interference," *IEEE Transactions on Communications*, vol. 20, no. 4, pp. 774–780, 1972.

[92] M. Jana, A. Medra, L. Lampe, and J. Mitra, "Pre-equalized faster-than-Nyquist transmission," *IEEE Transactions on Communications*, vol. 65, no. 10, pp. 4406–4418, 2017.

[93] T. Ishihara, S. Sugiura, and L. Hanzo, "The evolution of faster-than-Nyquist signaling," *IEEE Access*, vol. 9, pp. 86 535–86 564, 2021.

[94] M. Morelli, C.-C. J. Kuo, and M.-O. Pun, "Synchronization techniques for orthogonal frequency division multiple access (OFDMA): A tutorial review," *Proceedings of the IEEE*, vol. 95, no. 7, pp. 1394–1427, 2007.

[95] T. S. Rappaport, *Wireless communications: principles and practice*. Cambridge University Press, 2024.

[96] H. Ye, G. Y. Li, and B.-H. Juang, "Power of deep learning for channel estimation and signal detection in OFDM systems," *IEEE Wireless Communications Letters*, vol. 7, no. 1, pp. 114–117, 2017.

[97] H. He, C.-K. Wen, S. Jin, and G. Y. Li, "Deep learning-based channel estimation for beamspace mmWave massive MIMO systems," *IEEE Wireless Communications Letters*, vol. 7, no. 5, pp. 852–855, 2018.

[98] M. Valkama, M. Renfors, and V. Koivunen, "Advanced methods for I/Q imbalance compensation in communication receivers," *IEEE Transactions on Signal Processing*, vol. 49, no. 10, pp. 2335–2344, 2001.

[99] J. P. Glas, "Digital I/Q imbalance compensation in a low-IF receiver," in *IEEE GLOBECOM 1998 (Cat. NO. 98CH36250)*, IEEE, vol. 3, 1998, pp. 1461–1466.

[100] M. Valkama, J. Pirskanen, and M. Renfors, “Signal processing challenges for applying software radio principles in future wireless terminals: an overview,” *International journal of communication systems*, vol. 15, no. 8, pp. 741–769, 2002.

[101] D. Mattera, L. Paura, and F. Sterle, “MMSE WL equalizer in presence of receiver IQ imbalance,” *IEEE Transactions on Signal Processing*, vol. 56, no. 4, pp. 1735–1740, 2008.

[102] L. Tang, J. He, K. Wang, B. Wei, and X. Tang, “DFT-based method for accurate I/Q imbalance estimation,” *IEEE Transactions on Circuits and Systems II: Express Briefs*, vol. 71, no. 4, pp. 2474–2478, 2024.

[103] J. Tubbax, B. Come, L. Van der Perre, *et al.*, “Compensation of IQ imbalance and phase noise in OFDM systems,” *IEEE Transactions on Wireless Communications*, vol. 4, no. 3, pp. 872–877, 2005.

[104] A.-A. A. Boulogeorgos, V. M. Kapinas, R. Schober, and G. K. Karagiannidis, “I/Q-imbalance self-interference coordination,” *IEEE Transactions on Wireless Communications*, vol. 15, no. 6, pp. 4157–4170, 2016.

[105] X. Zhang, H. Li, W. Liu, and J. Qiao, “Iterative IQ imbalance compensation receiver for single carrier transmission,” *IEEE Transactions on Vehicular Technology*, vol. 66, no. 9, pp. 8238–8248, 2017.

[106] E. Nayebi, P. Dayal, and K.-B. Song, “Adaptive IQ mismatch compensation in time-domain using frequency-domain observations,” *IEEE Transactions on Signal Processing*, vol. 69, pp. 655–668, 2021.

[107] X. Peng, F. Yu, Z. Wang, J. Liu, C. Wang, and J. Wang, “A frequency-domain I/Q imbalance calibration algorithm for wideband direct conversion receivers using low-cost compensator,” *IEEE Access*, vol. 11, pp. 48 739–48 748, 2023.

[108] X. Huang, A. T. Le, and Y. J. Guo, “Joint analog and digital self-interference cancellation for full duplex transceiver with frequency-dependent I/Q imbalance,” *IEEE Transactions on Wireless Communications*, vol. 22, no. 4, pp. 2364–2378, 2022.

[109] S. Wen, G. Liu, C. Liu, H. Qu, M. Tian, and Y. Chen, “Waveform design for high-order QAM faster-than-Nyquist transmission in the presence of phase noise,” *IEEE Transactions on Wireless Communications*, vol. 21, no. 1, pp. 2–17, 2021.

[110] F. Ismael and E. Bedeer, “Widely-linear processing of faster-than-Nyquist signaling in the presence of IQ imbalance,” in *2024 IEEE 99th Vehicular Technology Conference (VTC2024-Spring)*, IEEE, 2024, pp. 1–6.

[111] J. G. Proakis and M. Salehi, *Digital communications*. McGraw-Hill, 2008.

[112] S. Li, W. Yuan, J. Yuan, B. Bai, D. W. K. Ng, and L. Hanzo, "Time-domain vs. frequency-domain equalization for FTN signaling," *IEEE transactions on vehicular technology*, vol. 69, no. 8, pp. 9174–9179, 2020.

[113] A. Gusmao, R. Dinis, and N. Esteves, "On frequency-domain equalization and diversity combining for broadband wireless communications," *IEEE Transactions on Communications*, vol. 51, no. 7, pp. 1029–1033, 2003.

[114] N. Docomo *et al.*, "5G channel model for bands up to 100 GHz," Technical report, Tech. Rep., 2016.

[115] T. J. Richardson and R. L. Urbanke, "The capacity of low-density parity-check codes under message-passing decoding," *IEEE Transactions on information theory*, vol. 47, no. 2, pp. 599–618, 2002.

[116] R. W. Chang, "Synthesis of band-limited orthogonal signals for multichannel data transmission," *Bell system technical journal*, vol. 45, no. 10, pp. 1775–1796, 1966.

[117] D. Falconer, S. L. Ariyavisitakul, A. Benyamin-Seeyar, and B. Eidson, "Frequency domain equalization for single-carrier broadband wireless systems," *IEEE Communications Magazine*, vol. 40, no. 4, pp. 58–66, 2002.

[118] R. Hadani, S. Rakib, M. Tsatsanis, *et al.*, "Orthogonal time frequency space modulation," in *2017 IEEE wireless communications and networking conference (WCNC)*, IEEE, 2017, pp. 1–6.

[119] F. M. Dekking, *A modern introduction to probability and statistics: Understanding why and how*. Springer Science & Business Media, 2005.

[120] X. Jiang and F. Kaltenberger, "Channel reciprocity calibration in TDD hybrid beamforming massive MIMO systems," *IEEE Journal of Selected Topics in Signal Processing*, vol. 12, no. 3, pp. 422–431, 2018.

[121] J. M. Nieminen and L. Muche, "A random matrix model whose eigenvalue spacings are closely described by the brody distribution," *Acta Physica Polonica B*, vol. 48, no. 4, 2017.

[122] A. Edelman, "Eigenvalues and condition numbers of random matrices," *SIAM Journal on Matrix Analysis and Applications*, vol. 9, no. 4, pp. 543–560, 1988.

[123] X. Huang, Y. J. Guo, and J. A. Zhang, “Transceiver I/Q imbalance self-calibration with phase-shifted local loopback for multichannel microwave backhaul,” *IEEE Transactions on Wireless Communications*, vol. 15, no. 11, pp. 7657–7669, 2016.

[124] X. Cheng, Z. Luo, and S. Li, “Joint estimation for I/Q imbalance and multipath channel in millimeter-wave SC-FDE systems,” *IEEE Transactions on Vehicular Technology*, vol. 65, no. 9, pp. 6901–6912, 2015.

[125] B. Razavi, “Cognitive radio design challenges and techniques,” *IEEE Journal of Solid-State Circuits*, vol. 45, no. 8, pp. 1542–1553, 2010.

[126] Y. Yao, Y. Jin, M. Li, Z. Dai, and S. He, “An accurate three-input nonlinear model for joint compensation of frequency-dependent I/Q imbalance and power amplifier distortion,” *IEEE Access*, vol. 7, pp. 140 651–140 664, 2019.

[127] J. Ren, “Digital predistortion architecture with feedback channel nonlinear blind identification and compensation,” *IEEE Microwave and Wireless Components Letters*, vol. 30, no. 11, pp. 1112–1115, 2020.

[128] Y.-D. Kim, E.-R. Jeong, and Y. H. Lee, “Adaptive compensation for power amplifier nonlinearity in the presence of quadrature modulation/demodulation errors,” *IEEE Transactions on Signal Processing*, vol. 55, no. 9, pp. 4717–4721, 2007.